1 2 9 0

UNIVERSIDADE Đ
COIMBRA

Felipe Ferreira Salles

PREDICTION OF STRAIN LOCALIZATION IN NONLINEAR STRAIN PATHS

Dissertação no âmbito do Mestrado em Engenharia de Materiais orientada pela Professora Doutora Marta Cristina Cardoso de Oliveira e pelo Professor Doutor Diogo Mariano Simões Neto e apresentada ao Departamento de Engenharia Mecânica

October 2021

FACULDADE DE
CIÊNCIAS E TECNOLOGIA
UNIVERSIDADE DE
COIMBRA

PREDICTION OF STRAIN LOCALIZATION IN NONLINEAR STRAIN PATHS

Submitted in Partial Fulfilment of the Requirements for the Degree of Master in Materials Engineering.

Previsão da localização da deformação em trajectórias de deformação não lineares

Author
Felipe Ferreira Salles

Advisors
Marta Cristina Cardoso de Oliveira
Diogo Mariano Simões Neto

Jury

President	**Professora Doutora Ana Paula da Fonseca Piedade** **Assistant professor of the Coimbra University**
Vowel	**Professor Doutor André Filipe Gomes Pereira** **Assistant Researcher of the Coimbra University**
Advisor	**Professora Doutora Marta Cristina Cardoso de Oliveira** **Associate professor of the Coimbra University**

Coimbra, October, 2021

“Knowing how to think empowers you far beyond those who know only what to think.”

— Neil deGrasse Tyson (1958- present)

ACKNOWLEDGEMENTS

The present work was carried out for the conclusion of the Masters in Materials Engineering. It is worth mentioning that deserves the recognition of those that contributed directly and indirectly to its development and improvement.

To Professor Marta Cristina Cardoso de Oliveira, for all the encouragement given to a highly complex work, for all the extremely valuable lessons provided throughout the work, for all the valuable support and for the demonstrated availability.

To Professor Diogo Mariano Simões Neto, for the availability and assistance provided throughout the work, as well as the constructive suggestions that were valuable for its improvement.

To the Coimbra University for the opportunity to undertake a master's course where I had great academic, professional and personal learning.

To my family, especially my parents for believing and investing in my academic and professional development.

To Mirela Barros Serafim for all the affection, companionship and all the emotional support, that significantly minimized the suffering during the difficult days of the pandemic that occurred during the period of this work.

To my friends Munique Sousa, Ricardo Campos, Maria Olivia Campos, as well as my cousins Claudia Lourenço, André Mendes, Camila Zambelli and Caio Reis also for their support during the difficult period of the pandemic, thus contributing to the evolution and non-interruption of this work.

Esta dissertação foi realizada no âmbito do projeto “If Damag Else: Modelling and numerical simulation of damage in metallic sheets: anisotropic behaviour and tension-compression asymmetry coupled approach for formability prediction” (PTDC/EME-EME/30592/2017), cofinanciados pela Fundação Portuguesa para a Ciência e Tecnologia (FCT) e pelo Fundo Europeu de Desenvolvimento Regional (FEDER), através do Programa Operacional Competitividade e Internacionalização (POCI-01-0145-FEDER-030592 e UIDB/00285/2020).

ABSTRACT

The simulation of nonlinear strain paths is important both for the design and development of tools for sheet metal forming processes, which can present very complex geometries, as well as for the prediction of failures during the process. Despite the evolution of computational methods, the prediction of ductile failure continues to be a challenge, especially in complex geometries. In this context, a benchmark was proposed within Numisheet 2020 conference, with the objective to evaluate the state of the art in the prediction of ductile fracture under nonlinear strain paths, for an advanced high strength steel (DP1180).

Numerical models were built for the Marciniak and the Nakazima test, enabling the analysis of both linear and non-linear strain paths, as well as the strain localization in the specimens. Regarding the constitutive model, the Hill48 and the Barlat91 anisotropic yield criterion were adopted. The Swift hardening law parameters were calibrated as well as a combination with the Voce law, including the weighting parameter. The tests were performed for conditions close to uniaxial tension, plane strain and different biaxial stress ratios.

In all tests performed, it was possible to predict the strain localization and the consequent drop in the forming force. The results from the monotonic strain paths tests highlight the importance of the yield criterion, which has a greater influence on the strain path predicted than the hardening law. This is more evident under conditions close to plane strain, which is the region were the yield criteria present higher differences in terms of the normal to the yield *loci*. Besides, the Barlat91 leads to strain paths closer to the experimental ones, when compared with the ones predicted by Hill48. Regarding the hardening law, the combined Swift and Voce always leads to a lower maximum punch force, which is attained also for a lower displacement. The same effects are valid for the bilinear strain paths. Finally, the information extracted on this work regarding the evolution of the stress triaxiality and the Lode parameter can be used in future works to calibrate uncoupled fracture models.

Keywords Finite Element Method, Sheet Metal Forming, Plastic Anisotropy, Nonlinear strain paths, Material flow, DD3IMP.

RESUMO

A simulação de trajectórias de deformação não linear é importante tanto para o projeto e desenvolvimento de ferramentas para processos de conformação de chapas metálicas, que podem apresentar uma geometria muito complexa, quanto para a previsão de fractura durante o processo. Apesar da evolução dos métodos computacionais, a previsão da fractura dúctil continua a ser um desafio, principalmente em geometrias complexas. Neste contexto, foi proposto um *benchmark* na conferência Numisheet 2020, com o objetivo de avaliar o estado da arte na previsão de fratura dúctil em trajectórias de deformação não linear, para um aço avançado de alta resistência (DP1180).

Foram construídos modelos numéricos para os testes de Marciniak e Nakazima, de modo a permitir a análise de trajectórias de deformações lineares e não lineares, bem como da localização da deformação nos provetes. Em relação ao modelo constitutivo, foram adotados os critérios anisotrópicos de plasticidade de Hill48 e Barlat91. Foram calibrados os parâmetros da lei de encruamento de Swift, bem como de uma combinação com a lei de Voce, incluindo o parâmetro de ponderação. Os testes foram realizados para condições próxima de tensão uniaxial, deformação plana e diferentes razões de tensão biaxial.

Em todos os ensaios realizados, foi possível prever a localização da deformação e a consequente queda da força de conformação. Os resultados dos testes para trajectórias de deformação monótonas destacam a importância do critério de plasticidade, que tem maior influência na trajectória de deformação prevista do que a lei de encruamento. Isso é mais evidente em condições próximas da deformação plana, que é a região onde os critérios de plasticidade apresentam maiores diferenças em termos da normal à superfície de plasticidade. Além disso, o critério de Barlat91 conduz a trajectórias de deformações mais próximas das experimentais, quando comparadas com as previstas por Hill48. Em relação à lei de encruamento, a combinação de Swift e Voce apresenta sempre uma força de punção máxima inferior, que é atingida também para um deslocamento menor. Os mesmos efeitos são válidos para trajectórias de deformação bilinear. Por fim, as informações extraídas neste trabalho a respeito da evolução da triaxialidade de tensões e do parâmetro de Lode podem ser utilizadas em trabalhos futuros para calibrar modelos não-acoplados de previsão de fratura dúctil.

Palavras-chave: Método dos elementos finitos, Conformação de Chapas de Metálicas, Plasticidade anisotrópica, Trajetórias de deformação não lineares, Escoamento plástico, DD3IMP.

CONTENTS

ACKNOWLEDGEMENTS i

ABSTRACT iii

RESUMO v

CONTENTS vii

LIST OF FIGURES ix

LIST OF TABLES xv

LIST OF SIMBOLS AND ACRONYMS/ ABBREVIATIONS xvii
  List of Symbols xvii
  Acronyms/Abbreviations xix

1. INTRODUCTION 1
  1.1. Motivation 1
  1.2. Objective 2
  1.3. Dissertation outline 3

2. ANALYSIS OF THE EXPERIMENTAL DATA 5
  2.1. Tests for characterizing the elastoplastic behavior 5
    2.1.1. Uniaxial Tensile/Compression Test 5
    2.1.2. Hydraulic Bulge Test 8
  2.2. Tests for characterizing the fracture behavior 9
    2.2.1. Fracture Characterization in Uniaxial Tension 10
    2.2.2. JIS Uniaxial Tension Test 11
    2.2.3. Hole Tension Test 12
    2.2.4. Conical Hole Expansion Test 13
    2.2.5. Fracture Characterization in Biaxial Tension 15
    2.2.6. Fracture Characterization in nonlinear strain paths 17

3. CONSTITUTIVE MODELS 19
  3.1. Hardening laws 19
    3.1.1. Identification of the Swift law parameters 21
    3.1.2. Identification of the Voce parameters 22
    3.1.3. Improvement of hardening law parameters 23
  3.2. Yield criteria 25

4. NUMERICAL MODEL 31
  4.1. Monotonic strain paths 32
  4.2. Nonlinear strain paths 35
    4.2.1. Pre-strain in uniaxial tension 35
    4.2.2. Pre-strain using Marciniak test conditions 36

5. RESULTS AND DISCUSSIONS 39
  5.1. Monotonic strain paths simulations 39
    5.1.1. Marciniak tests 39
    5.1.2. Nakazima tests 56

    5.1.3. Comparisons of monotonic strain path results and discussion 61
  5.2. Nonlinear strain paths 63
    5.2.1. Uniaxial followed by Mini-Nakazima (equibiaxial) 63
    5.2.2. Marciniak followed by Mini-Nakazima (equibiaxial) 66
    5.2.3. Comparisons of bilinear strain path results and discussion........................... 70
6. CONCLUSION 73
  6.1. Remarks for future work.. 74
BIBLIOGRAPHY 75
APPENDIX A: Triaxiality and Lode parameter 79

LIST OF FIGURES

Figure 1.1. (a) Deformation of a stent due to the blood flow as predicted by multiphysics. (b) Fluid–structure interaction tracks displacement of the heart valve [1]............. 1

Figure 1.2. Thinning distribution on an automotive inner hood [2]. 2

Figure 2.1. Schematic representation of the stress-strain curve obtained from the tensile test: (a) engineering stress-strain curve ; (b) beginning of the stress-strain diagram, comparing the real and the engineering stress-strain curves [5]. 6

Figure 2.2. Tensile specimen with:(a)(left) the indication of the lateral strains, εw/εt, during the extension; (right) the indication of the cut direction from a sheet, according to the RD [6]; (b) Anti-buckling fixture used in the uniaxial tension-compression-tension. 7

Figure 2.3. Specimen used for the tension-compression and uniaxial tensile tests [7]. 7

Figure 2.4. (a) Isotropic hardening – homothetic dilatation of the yield surface and kinematic hardening—translation of the yield surface with the same shape and size [2]. (b) Engineering stress-strain diagram for DP1180 in the low-strain region [10]. 8

Figure 2.5. Schematic representation of the bulge test, with the identification of the tools (adapted from [12]). 8

Figure 2.6. Diagrams for predict the occurrence of necking and/or fracture: (a) FLD concept as defined by Keeler and Goodwin; (b) FLD for necking and for fracture [5]. 10

Figure 2.7. Uniaxial tension specimen geometry. All dimensions are in millimeters [9]... 11

Figure 2.8. JIS uniaxial tension test: (a) major strain distribution obtained by DIC and the box inspector tool at the Ultimate Tensile Strength; (b) Strain distribution one image prior to fracture; (c) Thickness at the minimum cross-section in the specimen [9]. 12

Figure 2.9. Example of a re-construction of the strain path to failure based upon the post-mortem thickness strain and the DIC measured strain path in a JIS tensile test [9]. 12

Figure 2.10. Hole tension test: (a) specimen geometry; (b) Zoomed-in view of the major strain distribution [9]. 13

Figure 2.11. Cross-section of a DP1180 hole tension specimen showing the thickness: (a) at the hole edge; (b) maximum thinning location behind the edge [9]................. 13

Figure 2.12. Conical hole expansion test: (a) geometry of the specimen; (b) Schematic of the toolset. All dimensions are in millimeters. The conical punch head has an angle of 60 degrees with a truncated tip with a diameter of 3 mm and a base diameter of 20 mm [9]. 14

Figure 2.13. Fracture location in the hole expansion test and thickness measurement [8]. 15

Figure 2.14. Nakazima test: (a) Schematic of the tool set (Adapted from [21]); (b) Shape of the specimens [2]. 16

Figure 2.15. Set of specimens used in the Nakazima test for a complete FLD [2]. 16

Figure 2.16. Schematic layout of the device used in the Marciniak test [20]. 17

Figure 3.1. Comparison between experimental and numerical stress-strain: (a) Experimental data obtained from the uniaxial tensile test at RD and the numerical results obtained using the Benchmark parameters of Swift, Hockett-Sherby and the combined Swift with Hockett-Sherby law; (b) Experimental data from uniaxial test, bulge test and the combined curve using the uniaxial test results for the first part until 0.063 of equivalent plastic strain and the bulge test for the rest of the curve. 20

Figure 3.2. Linear regression of the set of points ln(σ) x ln(ε_p) obtained from the uniaxial test 1. 22

Figure 3.3. Comparison between experimental and numerical stress-strain curves: (a) experimental stress-strain curve of the uniaxial test with the hardening laws determined using either the uniaxial test or the bulge test results; (b) experimental stress-strain curve of the bulge test with the hardening laws determined using either the uniaxial test or the bulge test results. 24

Figure 3.4. Comparison between experimental and numerical stress-strain curves: (a) experimental data from the uniaxial test with the hardening laws determined using the combined experimental data; (b) experimental data from the bulge test with the hardening laws determined using the combined experimental data. 24

Figure 3.5. In-plane variation of the: (a) Normalized yield stress – θ (angle from the RD). (b) *r*-value – θ. (c) Yield surface assuming plane stress conditions with the $\boldsymbol{\sigma 3} = \mathbf{0}$. 27

Figure 3.6. Comparison between experimental and numerical in-plane variation of the yield stress, comparing different combinations of yield criteria and hardening laws. Continuous line: Swift+Voce 0.2%; circle marker: Swift 0.2%; square marker: Swift+Voce; triangular marker: Swift. 28

Figure 3.7. Strain ratio evolution as a function of the loading direction obtained analytically with the Hill48 and the Barlat91 yield criterion: (a) ratio between the minor and the through-thickness strain; and (b) ratio between the strain in the transverse and the rolling directions. 28

Figure 4.1: Meshes adopted for the tools of the Marciniak test: (a) Blank-holder (with draw bead); (b) Die (with draw bead); (c) Blank-holder (without draw bead); (d) Die (without draw bead); and (e) Punch. 32

Figure 4.2: Meshes adopted for the blank of the Marciniak test: (a) 1 inch width (with draw bead); (b) 1 inch width (without draw bead); (c) 5.5 inches width; (d) 6.5 inches width; and (e) 8 inches width. 33

Figure 4.3: Meshes adopted for the tools of the (a): Nakazima test: (i) Punch (101.6 mm); (ii) Blank-holder; and (iii) Die; (b) Mini-Nakazima test: (i) Punch (5 mm); (ii) Blank-holder; and (iii) Die. 34

Figure 4.4: Mesh adopted for the blank: (a) Nakazima test (8 inches width); (b) Mini-Nakazima test with 8 inches width; (c) Specimen used for uniaxial pre-strain followed by equibiaxial trajectory. 35

Figure 4.5: Assembly used for the model with the specimen with 5.5 inches, using the Marciniak tool (dark-blue: Blank-holder; grey: Die and pink: Punch) followed by Mini-Nakazima tool (light-blue: Blank-holder; brown: Die and green: Punch). The mesh shown in this figure is constructed in GID only for visualization purposes. 37

Figure 5.1. Evolution of the major strain-minor strain in the Marciniak test using the specimen with 1 inch width, comparing numerical predictions with experimental results. Simulations with drawbead (w.d.) and without drawbead (n.d.), both using a friction coefficient of 0.15. 40

Figure 5.2. Evolution of the predicted punch force in the Marciniak test specimen with 1 inch width, comparing the situations with drawbead (w.d.) and without drawbead (n.d.) (friction coefficient of 0.15). 41

Figure 5.3. Evolution of triaxiality (a, c and e) and Lode parameter (b, d and f) with the punch displacement in the Marciniak test specimen with 1 inch width from simulations with drawbead (w.d.) and without drawbead (n.d.) (all with friction coefficient of 0.15). 43

Figure 5.4. Equivalent plastic strain distribution in the Marciniak test specimen with 1 inch width: With drawbead (a) Swift/Hill48, (b) Swift/Yld91, (c) S_V/Yld91; without drawbead (d) Swift/Hill48, (e) Swift/Yld91, (f) S_V/Yld91. 44

Figure 5.5. Evolution of the major strain-minor strain in the Marciniak test using the specimen with 1 inch width and the friction coefficient of 0.15 (fr=0.15) or null friction coefficient (fr=0) in the numerical predictions. 45

Figure 5.6. Evolution of the predicted punch force in the Marciniak test specimen with 1 inch width, for friction coefficient of 0.15 (fr=0.15) and null friction coefficient (fr=0), using the model without drawbeads. 46

Figure 5.7. Evolution of triaxiality (a, c and e) and Lode parameter (b, d and f) with the punch displacement in the Marciniak test specimen with 1 inch width from simulations (without drawbeads) with friction coefficient of 0.15 (fr=0.15) and with null friction coefficient (fr=0). 47

Figure 5.8. Equivalent plastic strain distribution in the Marciniak test specimen with 1 inch width: with friction coefficient of 0.15 (a) Swift/Hill48, (b) Swift/Yld91, (c) S_V/Yld91; with null friction coefficient (d) Swift/Hill48, (e) Swift/Yld91, (f) S_V/Yld91. 48

Figure 5.9. Evolution in the Marciniak test specimen with 5.5 inch width of the predicted: (a) punch force and (b) major versus minor strain, including the experimental results. 50

Figure 5.10. Equivalent plastic strain on the specimen with 5.5 inch width predicted by the models: (a) Swift/Hill48, (b) Swift/Yld91, (c) S_V/ Yld91; (d) Strain localization in the location corresponding to the outer edge of the punch shoulder radius. 51

Figure 5.11. Evolution of triaxiality (a) and Lode parameter (b) with the punch displacement in the Marciniak test specimen with 5.5 inch width comparing different constitutive models. 52

Figure 5.12. Evolution in the Marciniak test specimen with 6.5 inch width of the predicted: (a) major versus minor strain, including the experimental results and (b) punch force. 53

Figure 5.13. Equivalent plastic strain on the specimen with 6.5-inch width predicted by the models: (a) Swift/Hill48, (b) Swift/Yld91, (c) S_V/Yld91; (d) Strain localization in the location corresponding to the outer edge of the punch shoulder radius. 53

Figure 5.14. Evolution in the Marciniak test specimen with 8 inch width of the predicted: (a) major versus minor strain, including the experimental results and (b) punch force. 55

Figure 5.15. Equivalent plastic strain on the specimen with 8-inch width predicted by the models: (a) Swift/Hill48, (b) Swift/Barlat91, (c) Swift+Voce/Barlat91; (d) Necking effect in the location corresponding to the outer edge of the punch. 56

Figure 5.16. Evolution of triaxiality (a) and Lode parameter (b) with the punch displacement in the Marciniak test specimen with 8 inch width comparing different constitutive models. 56

Figure 5.17. Evolution in the Nakazima test specimen (with 50.8 mm punch) of the predicted: (a) major versus minor strain, including the experimental results and (b) punch force. 57

Figure 5.18. Equivalent plastic strain in the Nakazima test specimen using 50.8 mm punch predicted by the models: (a) Swift/Hill48, (b) Swift/Yld91, (c) S_V/Yld91; (d) Strain distribution in the center of the specimen, as predicted with the S_V/Yld91 model. 58

Figure 5.19. Evolution of triaxiality (a) and Lode parameter (b) with the punch displacement in the Nakazima test specimen with 50.8 mm punch. 59

Figure 5.20. Evolution in the Nakazima test specimen (with 5 mm punch) of the predicted: (a) major versus minor strain, including the experimental results and (b) punch force. 60

Figure 5.21. Equivalent plastic strain in the Nakazima test specimen using 5 mm punch predicted by the models: (a) Swift/Hill48, (b) Swift/Yld91, (c) S_V/ Yld91; (d) Strain distribution in the center of the specimen, as predicted with the S_V/Yld91 model. 60

Figure 5.22. Evolution of triaxiality (a) and Lode parameter (b) with the punch displacement in the Nakazima test specimen with 5 mm punch. 61

Figure 5.23. Normalized stresses in the transverse and rolling directions from analytical predictions and numerical solutions from Marciniak tests. Diamond marker: Uniaxial stress; Triangle marker: Plane strain (5.5 inch specimen); Square marker: Equibiaxial stress. 62

Figure 5.24. Major strain-minor strain evolution comparison between experimental and numerical results of the nonlinear test (Uniaxial tension + mini-Nakazima). 64

Figure 5.25. Evolution of the predicted force applied to the specimen in the nonlinear test (Uniaxial tension + mini-Nakazima): (a) First phase; (b) Second phase. 64

Figure 5.26. Equivalent plastic strain in the specimen of the nonlinear test (Uniaxial tension + mini-Nakazima): (a) Swift/Hill48, (b) Swift/Yld91, (c) S_V/Yld91; (d) Strain distribution in the center of the specimen, as predicted with the S_V/Yld91 model. 65

Figure 5.27. Evolution of triaxiality (a) and Lode parameter (b) in the nonlinear test (Uniaxial tension + mini-Nakazima). Continuous line: phase one; Dashed line: phase two. 65

Figure 5.28. Comparison of the major strain-minor strain evolution between experimental and numerical results of the nonlinear test (5.5 inch Marciniak + mini-Nakazima). 66

Figure 5.29. Evolution of the predicted force applied to the specimen in the nonlinear test (5.5 inch Marciniak + mini-Nakazima): (a) First phase; (b) Second phase. 67

Figure 5.30. Equivalent plastic strain in the specimen of the nonlinear test (5.5 inch Marciniak + mini-Nakazima): (a) Swift/Hill48, (b) Swift/Yld91, (c) S_V/Yld91; (d) Strain distribution in the center of the specimen, as predicted with the S_V/Yld91 model. 67

Figure 5.31. Evolution of triaxiality (a) and Lode parameter (b) in the nonlinear test (5.5 inch Marciniak + mini-Nakazima). Continuous line: phase one; Dashed line: phase two. 68

Figure 5.32. Comparison of the major strain-minor strain evolution between experimental and numerical results of the nonlinear test (6.5 inch Marciniak + mini-Nakazima). 69

Figure 5.33. Evolution of the predicted force applied to the specimen in the nonlinear test (6.5 inch Marciniak + mini-Nakazima): (a) First phase; (b) Second phase. 69

Figure 5.34. Equivalent plastic strain in the specimen of the nonlinear test (6.5 inch Marciniak + mini-Nakazima): (a) Swift/Hill48, (b) Swift/Yld91, (c) S_V/Yld91; (d) Strain distribution in the center of the specimen, as predicted with the S_V/Yld91 model. 70

Figure 5.35. Evolution of the strain along the thickness direction, at the center of the specimen, in function of the punch displacement (Swift/Yld91 model). 71

Figure A. 1. Usual values for stress states in the space of ($\boldsymbol{\eta}$, $\boldsymbol{\xi}$) [44]. 80

Figure A. 2. Usual values for stress states in the space of ($\boldsymbol{\eta}$, $\boldsymbol{\theta}$) [45]. 81

LIST OF TABLES

Table 2.1. Adapted table from the data provided by Numisheet 2020 benchmark 2 committee with the stages for nonlinear tests. [3]. 18

Table 3.1. Hardening laws parameters obtained from the experimental results of the uniaxial test (UN) and the bulge test (BI). 23

Table 3.2. Improved hardening laws parameters. 25

Table 3.3. Parameters of the yield criteria Hill 1948 and Barlat 1991 provided by the benchmark committee. 26

Table 5.1. Computational times of the Marciniak test with and without drawbead. 45

Table 5.2. Computational times of the Marciniak test specimen with 1 inch width using different values of friction coefficient. 49

Table A.1. Usual values for $\boldsymbol{\eta}$, $\boldsymbol{\xi}$ and $\boldsymbol{\theta}$ for each stress state condition [44][45]. 81

LIST OF SIMBOLS AND ACRONYMS/ ABBREVIATIONS

List of Symbols

α – weighting parameter

δ_{ij} – Kronecker symbol

ε_0 – Swift hardening law material parameter

ε_1 – major strain

ε_2 – minor strain

$\varepsilon_1^{\mathrm{f}}$ – true circumferential tensile strain at fracture

$\varepsilon_2^{\mathrm{f}}$ – minor strain at the outer edge at fracture

$\varepsilon_{\mathrm{neck}}$ – strain on necking

$\varepsilon_{\mathrm{RD}}$ – strain in the rolling direction

ε_t – strain along the thickness direction

$\varepsilon_{\mathrm{TD}}$ – strain in the transversal direction

ε_{w} – strain in the width direction

$\bar{\varepsilon}_{\mathrm{p}}$ – equivalent plastic strain

η – stress triaxiality

θ – angle to the rolling direction

θ_L – Lode angle

$\bar{\theta}$ – normalized Lode angle

ξ – normalized third stress invariant

$\boldsymbol{\sigma}$ – Cauchy stress tensor

σ_0 – initial yield stress

σ_m – mean stress

σ_{RD} – stress in the rolling direction

σ_{TD} – stress in the transversal direction

$\bar{\sigma}$ – Von Mises yield criterion equivalent stress

υ – Poisson coefficient

φ – loading direction

A – Voce hardening law material parameter

A_H – Hockett-Sherby hardening law material parameter

b_H – Hockett-Sherby hardening law material parameter

B – Voce hardening law material parameter

B_H – Hockett-Sherby hardening law material parameter

$c_i, i = 1, \ldots, 6$ – Barlat91 anisotropy coefficients

C – Voce hardening law material parameter

C_H – Hockett-Sherby hardening law material parameter

d_0 – initial diameter

$d_{\mathrm{f}}^{\mathrm{out}}$ – external diameter at fracture

E – Young modulus

F – Hill48 anisotropy coefficients

G – Hill48 anisotropy coefficients

H – Hill48 anisotropy coefficients

I_1, I_2, I_3 – Cauchy stress tensor invariants

J_1, J_2, J_3 – deviatoric stress tensor invariants

K – Swift hardening law material parameter

L – Hill48 anisotropy coefficients

m – Barlat91 exponent based on the crystallographic structure

M – Hill48 anisotropy coefficients

n – Swift hardening law material parameter

N – Hill48 anisotropy coefficients

r – r-value

$R_{\theta+90}$ – r-value at 90 degrees to the cracking orientation

$\mathbf{S}$ – linear transformation of the deviator stress tensor

$\mathbf{s}$ – deviatoric component of the Cauchy stress tensor

S_1, S_2, S_3 – principal stresses of the linear transformed stress tensor

Y – flow stress

Acronyms/Abbreviations

ASTM – American Society for Testing and Materials

CNC – Computer Numeric Control

DD3IMP – Deep Drawing 3D IMPlicit finite element code

DIC – Digital Image Correlation

FLD – Forming Limit Diagram

RD – Rolling Direction

TD – Transversal Direction

1. INTRODUCTION

1.1. Motivation

Numerical methods, such as the finite element method, have evolved over time, enabling the representation of increasingly complex physical phenomena, with more accurate results. The simulations processing time has also undergone developments and various techniques have been introduced to optimize the calculations and reduce the computational cost, in addition to the evolution of the processing power of computers. The future of engineering has been directed towards the increasing use of computational methods, due to all the benefits they provide. Today these methods are used in almost all industrial sectors in different engineering applications, from structural simulations, to fluid dynamics, and electromagnetic simulations, in addition to simulations using coupled multiphysics, as shown in the example in **Figure 1.1** [1].

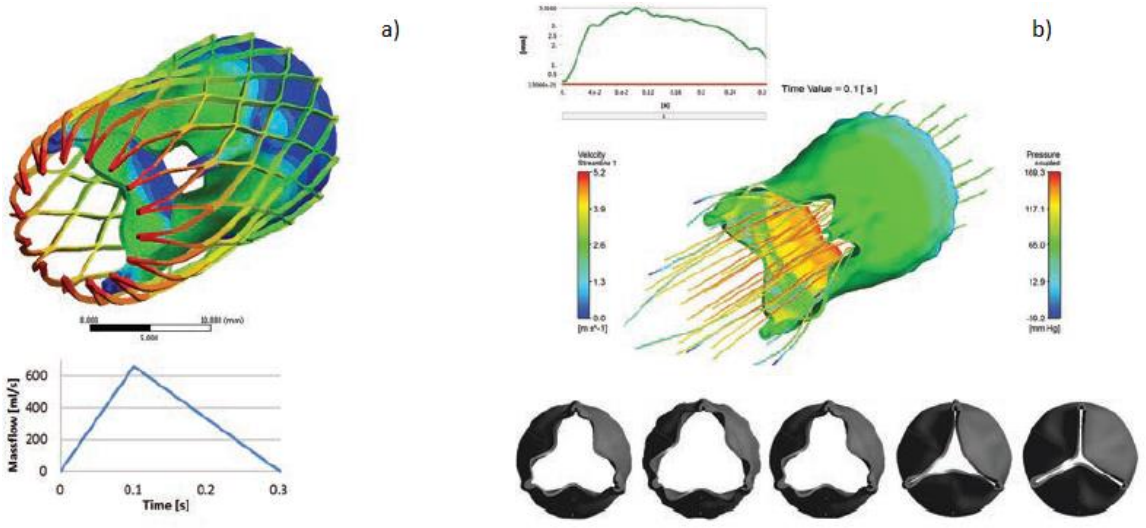

Figure 1.1. (a) Deformation of a stent due to the blood flow as predicted by multiphysics. (b) Fluid–structure interaction tracks displacement of the heart valve [1].

According to Banabic, “The concept of virtual manufacturing has been developed in order to increase the industrial performances, being one of the most efficient ways of reducing the manufacturing times and improving the quality of the products” [2]. The finite element method has been one of the most used numerical approaches for performing simulations of manufacturing processes, due to its great versatility of solutions and the great accuracy of its results, leading to a substantial reduction in design time and cost reduction in prototyping tests

[2]. In this context, many experimental and numerical methodologies have been proposed for the characterization and prediction of failure occurrence during sheet metal forming processes and crash tests of automotive components. Nevertheless, the inconsistency in the results obtained with these models reflects a general lack of maturity in the field of failure modelling.

1.2. Objective

One of the challenges in industry is the reliable prediction of failure under complex deformation histories, since it poses questions not only to the model selection but also to its calibration. In this context, the Numisheet 2020 conference proposed a benchmark with the objective to evaluate the state of the art in the prediction of fracture, during deformation of advanced high strength steel and aluminum alloys, under nonlinear strain paths. Localized necking plays an important role in fracture events, being also an unwanted effect during the forming process, as highlighted in **Figure 1.2**, which shows an example of localized thinning prediction in a simulation of an automotive component. Therefore, participants were also asked to predict if localized necking occurs in each test [3].

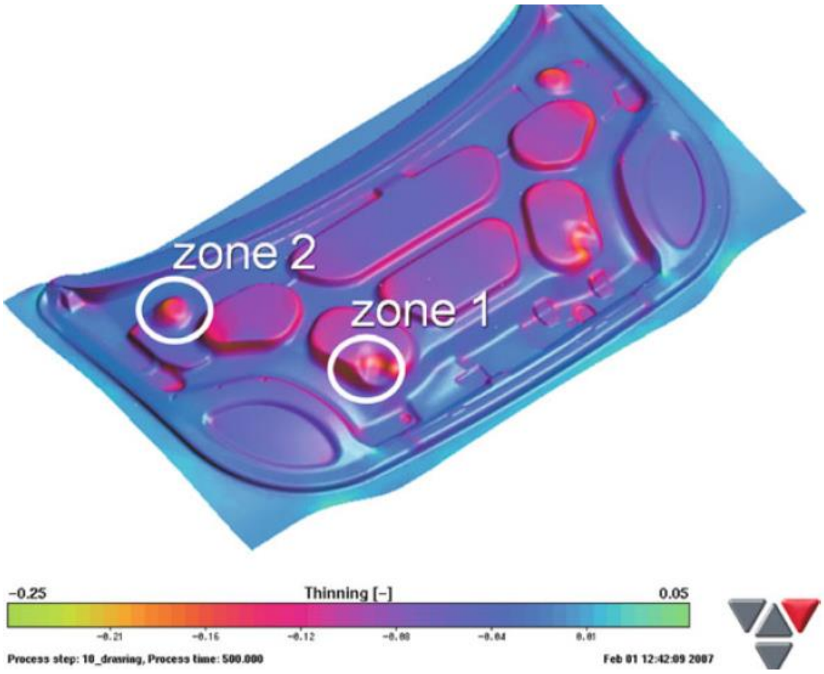

Figure 1.2. Thinning distribution on an automotive inner hood [2].

The present work aims to contribute to the objective of this benchmark. The focus will be given for one of the materials, the DP1180 steel. Since necking is mainly controlled by the plastic behavior of the material, particular focus was given to the selection of models that best describe this behavior. Moreover, the numerical models for some linear and bilinear strain paths were built and analyzed, allowing to evaluate the ability to forecast localized necking, without using damage models. The study of the monotonic trajectories was performed to improve the understanding about the differences observed between the different plasticity models selected in the prediction of the strain paths and the strain localization.

1.3. Dissertation outline

The dissertation structure was organized into six chapters and an appendix. Chapter **2** contains a brief theoretical presentation of each experimental result supplied by the Numisheet 2020 benchmark 2 committee and used in the constitutive models definition. Chapter **3** describes the procedure adopted for the calibration of the work hardening laws and the plasticity criteria.

In chapter **4**, details of the numerical model are provided, as well as a description of the discretization process of the specimens' geometries and the tools used in each simulation. In chapter **5**, the numerical results are presented and discussed, including their comparison with the experimental results provided by the Numisheet 2020 benchmark 2 committee.

Chapter **6** presents a brief summary of the conclusions obtained from the work carried out, as well as some recommendations for future work.

2. ANALYSIS OF THE EXPERIMENTAL DATA

2.1. Tests for characterizing the elastoplastic behavior

2.1.1. Uniaxial Tensile/Compression Test

The uniaxial tensile test is one of the most used for characterizing the mechanical properties of materials, including metallic sheets. It is a standardized test that allows obtaining the engineering or real stress-strain curve of the material, as shown in **Figure 2.1** [4]. This test enables determining properties such as the Young's modulus, the yield stress and the yield strength [5]. Moreover, thin metallic sheets are generally anisotropic materials, since they are produced using the rolling process. In order to evaluate their anisotropic behavior, besides the yield stress it is also usual to evaluate the *r*-value, also known as the Lankford anisotropy coefficient. This parameter is defined as:

$$r = \frac{\varepsilon_{\mathrm{w}}}{\varepsilon_{\mathrm{t}}}, \tag{1}$$

where ε_{w} is the strain in the width direction and ε_t is the strain along the thickness direction, both perpendicular to the loading (length) direction. For metallic sheets, uniaxial tensile tests are commonly performed with samples taken at different angles from the rolling direction (RD), as shown in **Figure 2.2** (a) [6], allowing to evaluate the in-plane distribution of the yield stress and of the *r*-value. These results are used to characterize the orthotropic behavior and, accordingly, to calibrate the anisotropic yield criterion parameters. Therefore, the benchmark committee supplied results for uniaxial tensile tests, performed for every 15 degrees to the RD, from 0 to 90 degrees, repeating the test three times for each angle. The data was acquired up to the maximum load point, using a virtual strain gauge of 50 mm from the centerline of the specimen, but it was also recorded with Digital Image Correlation (DIC) technology [7].

The traditional application of the virtual strain gauge is only able to characterize the material behavior while the onset of necking does not occur. Indeed, it can lead to errors in the stress evaluation once a triaxial stress state is installed. Therefore, it can only be used to determine the stress-strain curve until the maximum load. However, this means that data can only be extracted for strain values much lower than the ones commonly attained in forming processes. On the other hand, the use of DIC during the test enables a more aggressive approach to measure deformations after the onset of necking, as proposed by Min et al. [8] and others. In this work, the DIC technology was applied to 201 points positioned along the specimen's centerline; each point positioned at 0.25 mm from each other, and treated assuming an average gauge length of 0.5 mm. This allows the identification of the points where the strain localization occurs, as well as the evaluation of the stress-strain evolution for those specific points. The data obtained using this second approach, combined with the one from the traditional 50 mm strain gauge can be used to determine the material hardening behavior [8]. Moreover, the DIC data concerning the deformations after necking, until the material fractures, is used to determine the fracture strain for the uniaxial stress state [9].

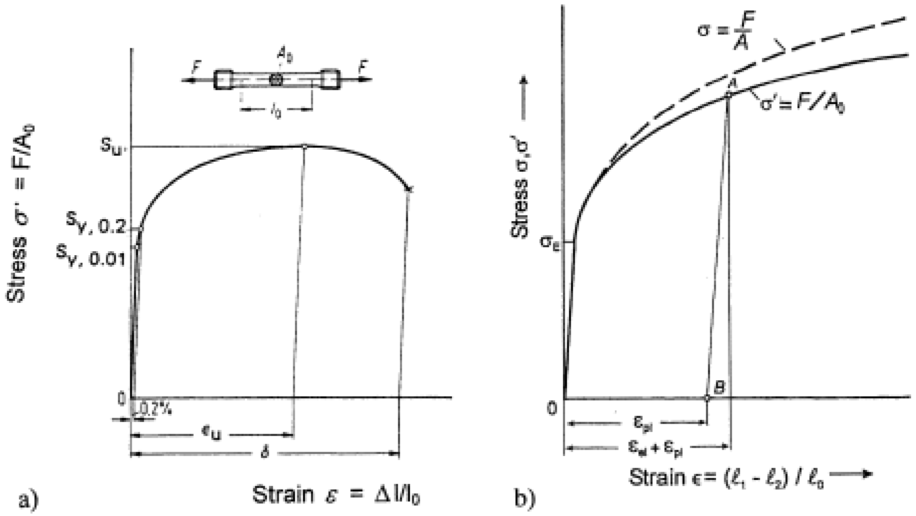

Figure 2.1. Schematic representation of the stress-strain curve obtained from the tensile test: (a) engineering stress-strain curve ; (b) beginning of the stress-strain diagram, comparing the real and the engineering stress-strain curves [5].

Besides the isotropic hardening behavior, highlighted in **Figure 2.1**, metallic materials can also show sensitivity to strain paths changes. Therefore, uniaxial tension followed by compression and tension were also performed, for specimens oriented only in the RD. The specimen used in these tests was a sample of thin rectangular section, as shown in the **Figure 2.3**. The average thickness of the specimens was 1.055 mm [7]. To avoid buckling effects of the thin sheet, an anti-buckling device that follows the ASTM E9 standard was used, as shown in **Figure 2.2** (b). To reduce the friction between the anti-buckling device and the plunger body, PTFE adhesives were glued to the contact regions, as highlighted also in **Figure 2.2** (b). These tests with strain path reversal were performed using a sequence of 6 steps: (i) load control, to adjust the machine and leave it with zero load; (ii) displacement control, to apply a fixed displacement that produces a nominal strain of about 75 % of the maximum uniform strain; (iii) holding for 10 s; (iv) displacement control, to apply a fixed inverse displacement until the axial strain is close to zero; (v) holding for 10 s; (v) displacement control, until the tension failure of the material. The test parameters were defined according to the ASTM E8 and E9 standard [10][4][11].

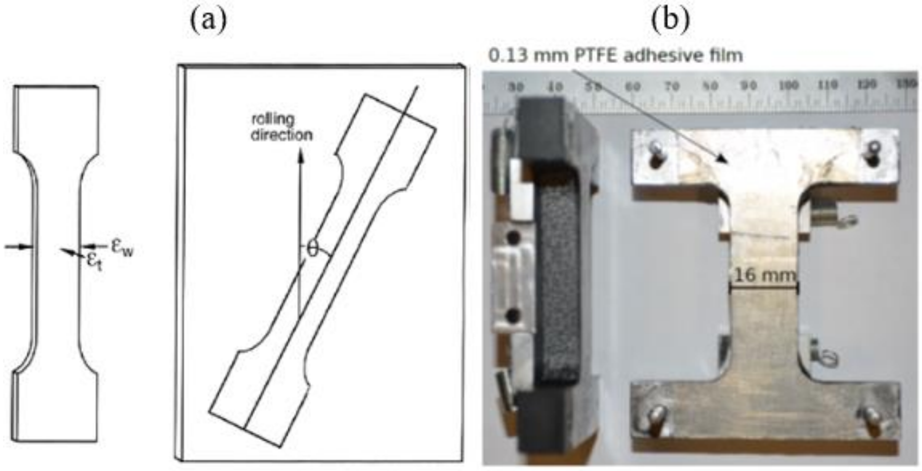

Figure 2.2. Tensile specimen with:(a)(left) the indication of the lateral strains, εw/εt, during the extension; (right) the indication of the cut direction from a sheet, according to the RD [6]; (b) Anti-buckling fixture used in the uniaxial tension-compression-tension.

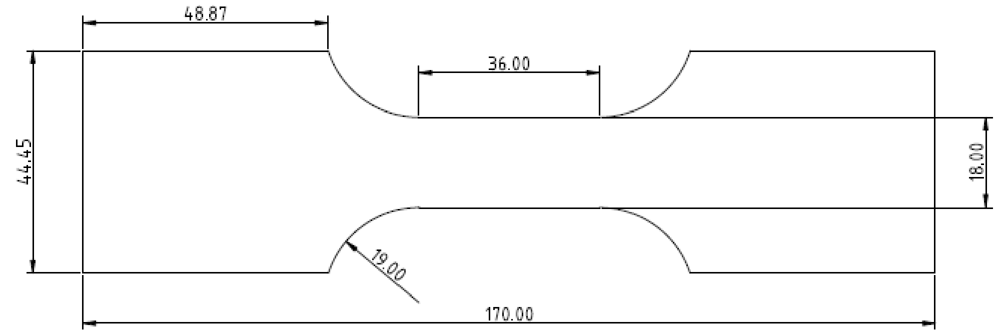

Figure 2.3. Specimen used for the tension-compression and uniaxial tensile tests [7].

The tension/compression test seeks to characterize the material behavior under reverse strain-paths, allowing to define the parameters to describe the isotropic and kinematic hardening behavior. The latter is typically described as the translation of the yield surface with the plastic deformation, associated to a change in the flow stress due to the strain reversal, as shown in **Figure 2.4** (a) [2]. The stress-strain curves obtained for the material under analysis are shown in **Figure 2.4** (b), highlighting the fact that the hardening behavior is quite sensible to the inversion of the strain path. However, since the region of interest for this study, i.e. the central point of the metal sheet, is not submitted to strain paths reversal, this effect will not be taken into account in this work.

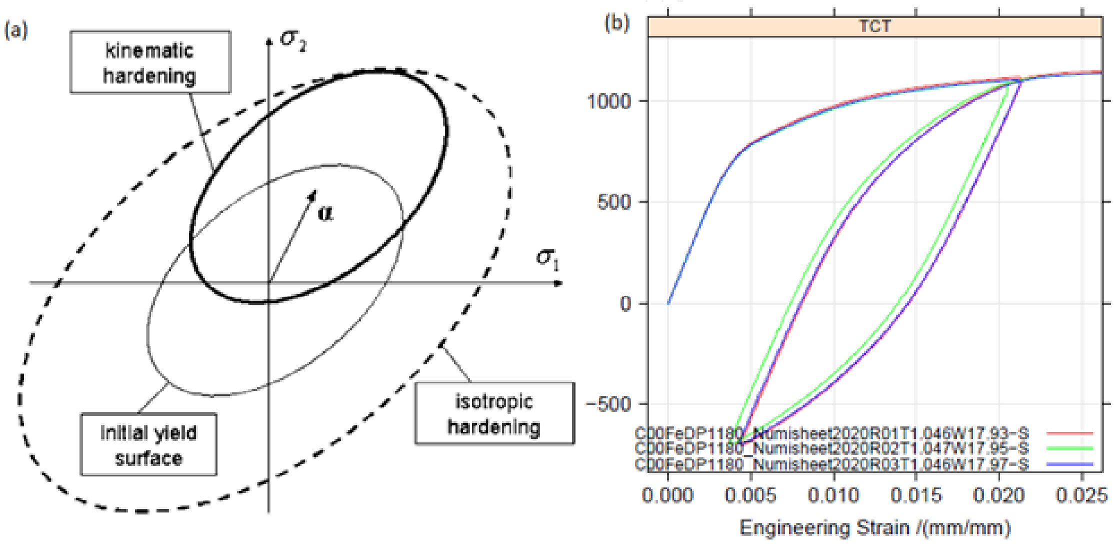

Figure 2.4. (a) Isotropic hardening – homothetic dilatation of the yield surface and kinematic hardening—translation of the yield surface with the same shape and size [2]. (b) Engineering stress-strain diagram for DP1180 in the low-strain region [10].

2.1.2. Hydraulic Bulge Test

The hydraulic bulge test is used to determine the strain hardening properties of sheet materials in biaxial tension stress state. Usually, in sheet metal forming processes the attained strains are larger than the uniform strain obtained under the uniaxial tension test conditions. This makes the bulge test a better option for the characterization of the hardening properties of metal sheets at large strains [12]. The test is performed by restraining the boundary edges of the metal sheet with a drawbead, to prevent the occurrence of radial displacements. Applying hydraulic pressure to the metal blank, the geometry changes to a hemispherical shape. Since there is no use of a punch, the influence of contact with friction is reduced to a minimum. **Figure 2.5** shows a schematic representation of the test layout [13].

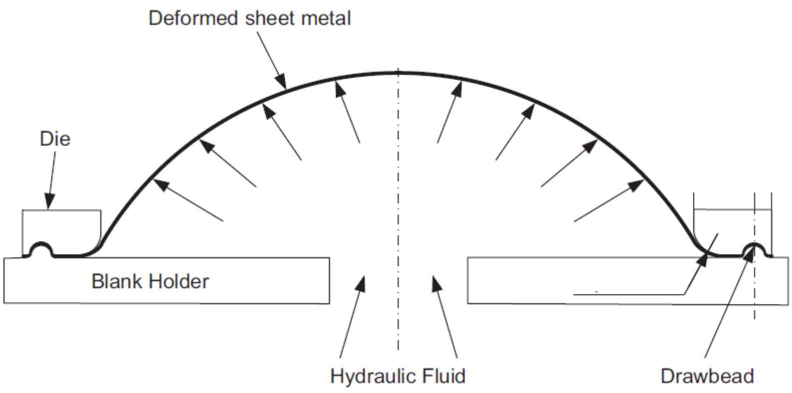

Figure 2.5. Schematic representation of the bulge test, with the identification of the tools (adapted from [13]).

The data acquired in both the uniaxial tensile tests and the bulge tests was analyzed using the software CalSysSmart™, developed by Yoon [3]. It calculates an average of the values that follow a non-discrepant behavior, to determine mechanical properties in a more representative way, i.e. it identifies and excludes outliers. The software automatically adjusts the test data determining the elastic and plastic properties of the material. Along with the Young modulus data, the program also determines the parameters of some hardening laws, such as Swift, Voce, Hockett-Sherby, modified Voce, modified Hockett-Sherby. Moreover, it also identifies the parameters of some yield criteria, such as the Hill48, Hill90, Barlat91, Barlat2000 and Barlat2004 [7].

2.2. Tests for characterizing the fracture behavior

The approaches for sheet metal forming processes have to consider the material's ability to undergo plastic deformation to the desired shape without the appearance of defects. Necking is a limiting factor not only for the appearance of fracture, but also for other undesirable effects in the sheet metal forming process. In fact, it represents the beginning of the structural instability of the material. Usually, the occurrence of necking and/or fracture is evaluated based on specific experimental tests, which enable the determination of the forming limit diagram (FLD). This was originally proposed by Keeler and Goodwin and is used to evaluate the material formability, as shown in **Figure 2.6** (a). The diagram provides the major (ε_1) and minor (ε_2) strain at the onset of necking. Currently, different diagrams are used depending on the type of application desired, which can consider only the onset of necking or also fracture, as shown in **Figure 2.6** (b) [5].

The data supplied by the benchmark committee for the calibration of fracture models, under nearly monotonic strain paths, was acquired from the following seven tests: (i) Simple shear; (ii) Uniaxial Tension: JIS Tensile Test, Hole Tension Test, Conical Hole Expansion Test; (iii) Plane Strain Tension: V-Bend Test and Plane Strain Notch Test; (iv) Biaxial Stretching: Hemispherical Punch test with a 5 mm or 10 mm Radius [3]. These tests try to cover a wide range of stress states, enabling the proper calibration of fracture models. In the context of the present work, they are relevant because they allow the study of different monotonic strain paths. Nevertheless, several tests were performed under uniaxial tension conditions, meaning that more information is available for this specific path. In the following section, some details concerning the tests under uniaxial tension are given, to highlight the difficulties inherent to the evaluation of the fracture strain, even under nearly linear strain path conditions.

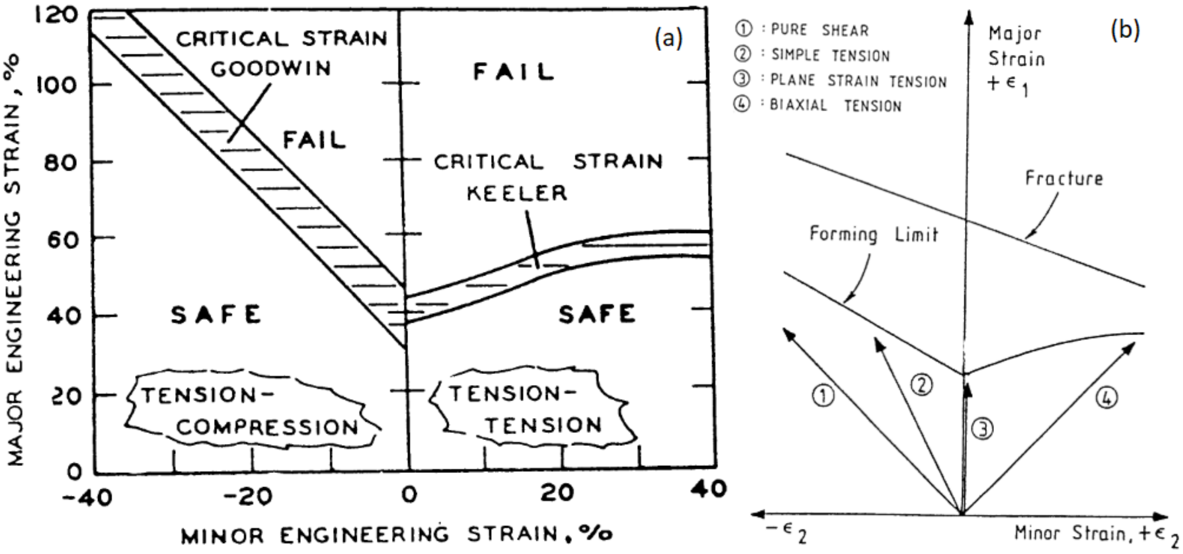

Figure 2.6. Diagrams for predict the occurrence of necking and/or fracture: (a) FLD concept as defined by Keeler and Goodwin; (b) FLD for necking and for fracture [5].

2.2.1. Fracture Characterization in Uniaxial Tension

One of the reasons for using different test methodologies to determine the strain at fracture is that, in uniaxial tests, the strain values may be slightly different depending on the strategy adopted for their evaluation. The use of DIC enables the measurement of strains in the specimen surface, but it may not correctly capture the large gradient in the strain field that occurs in the material, due to the instability caused by the necking, which occurs before fracture. Therefore, the measured value may be below the actual fracture strain value. Accordingly, post-Mortem thickness measurement can also be used to assist in the evaluation of the fracture strain, trying to approximate better the actual value. In this procedure, the thickness of the specimen is measured near the fracture site using optical microscopy. Using the principle that the behavior of the material follows plastic incompressibility, the principal strains in the sheet metal plane can be determined from the thickness strain at the fracture location. However, since the other two principal strains are unknown, it is necessary to assume that the strain path (ratio between the in-plane principal strains) is also known. This is commonly evaluated based on the average strain path within the neck [9].

2.2.2. Uniaxial Tension Test according to the Japanese Industrial Standards

All tests were performed at a cross-head velocity of 0.05 mm/s and at least three repetitions were performed per orientation. **Figure 2.7** shows the geometry of the specimen used in the tests [9]. In the JIS Uniaxial Tension Test, the major strain presents a uniform distribution until the onset of necking, as shown in **Figure 2.8** (a). The plastic instability will occur on the surface of the specimen in a strain localization band that extends along the width of the gauge region. Necking can occur at any point along the length of the test piece and the localization band will form an angle in relation to the principal stress generated in the test piece, as shown in **Figure 2.8** (b). The virtual strain gauge, 50 mm long and 25 mm wide, is also displayed in **Figure 2.8** (a). For the local analysis of the strains along the necking region, the aggressive approach was also applied, considering an average gauge length of 0.2 mm for the analysis. After the fracture, the post-mortem thickness measurement procedure was applied using an optical microscopy, as shown in the **Figure 2.8** (c) [9].

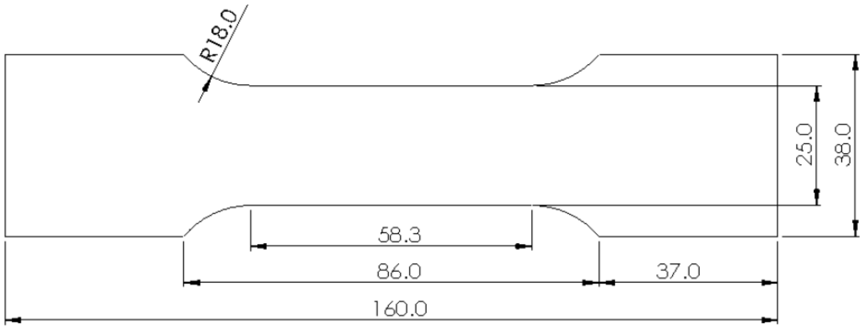

Figure 2.7. Uniaxial tension specimen geometry. All dimensions are in millimeters [9].

The DIC analysis enables the definition of the strain path, until the last point before fracture. The post-mortem thickness measurement allows defining the thickness strain, ε_t. The assumption of volume conservation enables the definition of the relation between the major and minor strain: $\varepsilon_1 + \varepsilon_2 = -\,\varepsilon_t$. Therefore, the fracture strain can be estimated using one of two methodologies for correction, as shown in the **Figure 2.9** [9]. Method I was proposed by Gorji et al. [14], based on the principle that all deformations, between the last measurement by DIC images and fracture, occur under plane strain condition. Method II is based on the extrapolation of the DIC strain path. Although the two methodologies provide the same final thickness strain, the strains paths and stress states are different [9]. The analysis of these methods also highlights the fact that the change of the strain path due to the onset of necking is acknowledge by many researchers.

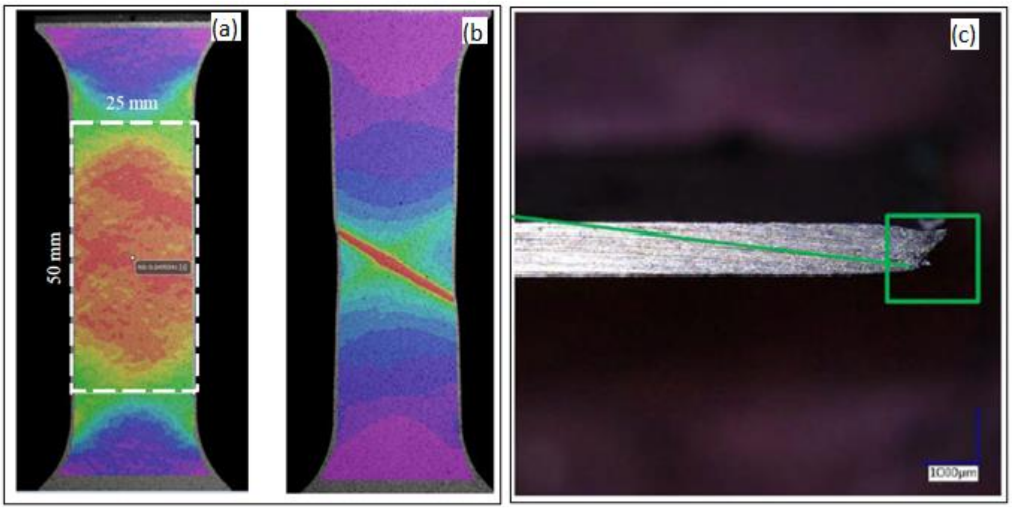

Figure 2.8. JIS uniaxial tension test: (a) major strain distribution obtained by DIC and the box inspector tool at the Ultimate Tensile Strength; (b) Strain distribution one image prior to fracture; (c) Thickness at the minimum cross-section in the specimen [9].

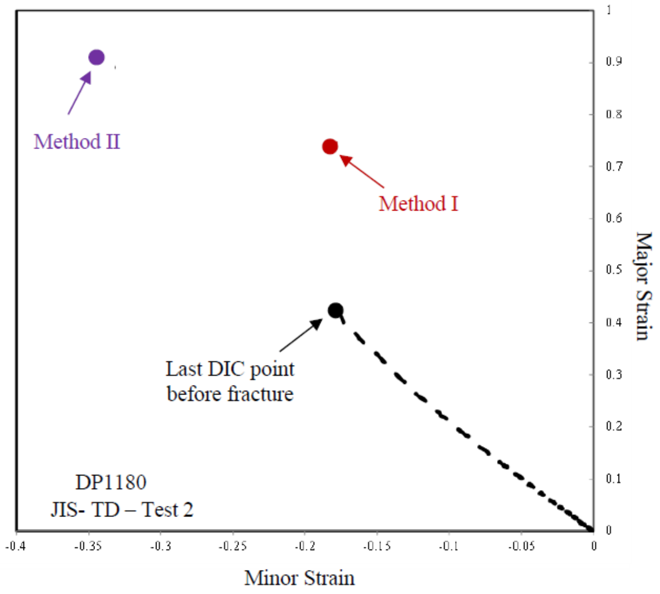

Figure 2.9. Example of a re-construction of the strain path to failure based upon the post-mortem thickness strain and the DIC measured strain path in a JIS tensile test [9].

2.2.3. Hole Tension Test

The specimens used in this test were manufactured by CNC machining with a central hole of 5 mm, as shown in the **Figure 2.10** (a). The other dimensions of the specimen were the same as those defined for the JIS tensile test. For DP1180 steel, the specimens were manufactured with the length aligned with the transversal direction to the rolling (TD). The tests were performed with displacement control with a crosshead speed of 0.005 mm/s. The hole in the specimen generates a stress concentration at the edges of the hole, as shown in the **Figure 2.10** (b). Previous works shown that the stress state at the free edges correspond to uniaxial [15], [16]. Therefore, fracture occurs in the plane perpendicular to the tensile direction. Although the fracture is ideally formed at the edge of the hole, it can occur in a short distance from the edge because of imperfections in the material and defects generated in the manufacturing process. Thus, post-mortem thickness was measured at two locations: at the edge and at the point where the greatest reduction in cross section occurs, as shown in the **Figure 2.11** [9].

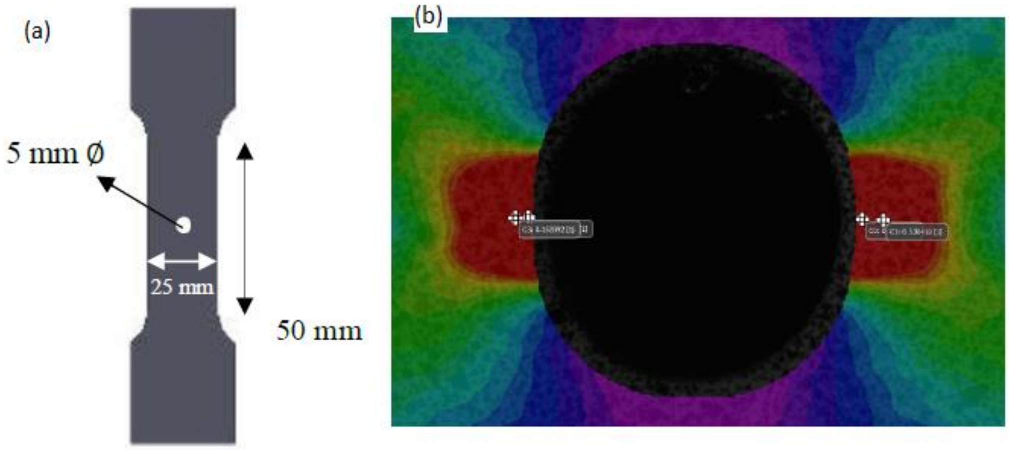

Figure 2.10. Hole tension test: (a) specimen geometry; (b) Zoomed-in view of the major strain distribution [9].

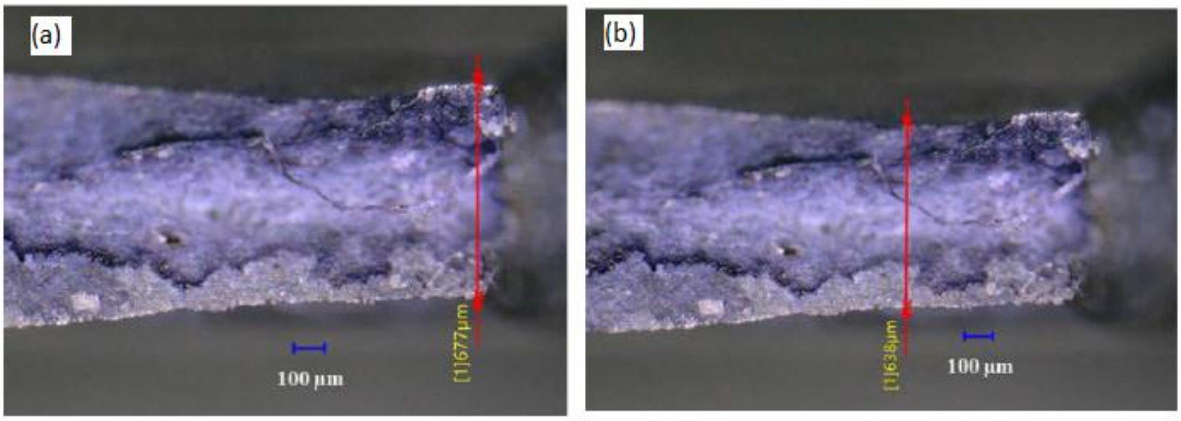

Figure 2.11. Cross-section of a DP1180 hole tension specimen showing the thickness: (a) at the hole edge; (b) maximum thinning location behind the edge [9].

2.2.4. Conical Hole Expansion Test

According to Pathak et al. [17]–[19], the Conical hole expansion test allows the characterization of fracture in uniaxial tension, since this stress state occurs at the free edge of the expanding circumferential hole. The occurrence of fracture behind the edge of the hole is prevented by the conical shape of the punch, phenomenon that occurs in hole expansion tests performed with cylindrical and flat punches. In addition, the flat punch also changes the results, providing smaller strains due to the failure generated behind the edge, which is in plane strain mode. **Figure 2.12** (a) shows the geometry and dimensions of the metallic sheet used in the test while the tools are shown in **Figure 2.12** (b). The test was performed on a double-acting hydraulic MTS formability press with an annular die with an external diameter of 225 mm and an internal diameter of 30 mm, in addition to a 12 mm inlet radius. A constant clamping force of 640 kN was used to prevent the metal sheet from sliding. At least four tests were performed. In the results, there was a tendency for cracks to form approximately in line with the rolling direction [9].

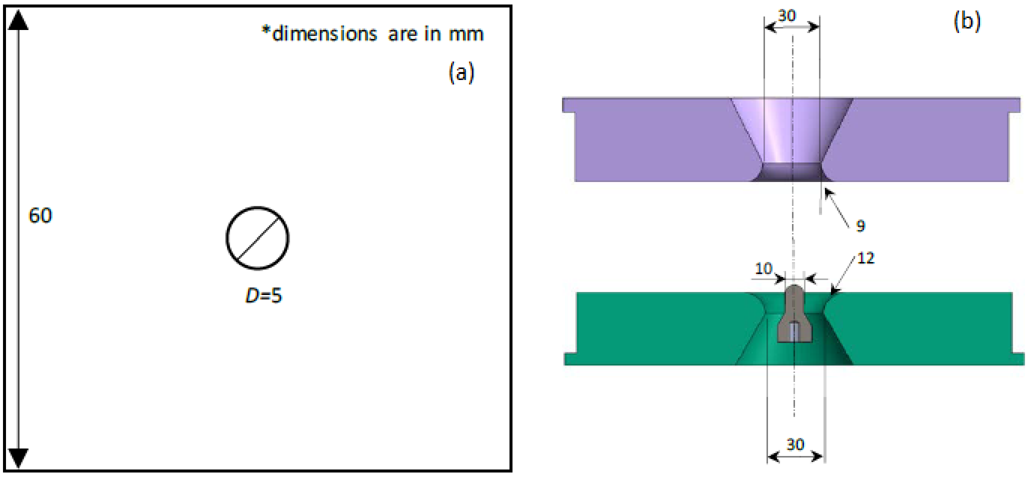

Figure 2.12. Conical hole expansion test: (a) geometry of the specimen; (b) Schematic of the toolset. All dimensions are in millimeters. The conical punch head has an angle of 60 degrees with a truncated tip with a diameter of 3 mm and a base diameter of 20 mm [9].

This test presents difficulties in performing accurate strain measurements using DIC technology, since it is difficult to measure the thickness of the edge from the images. As an alternative, the DIC system was used to measure the internal and external diameters of the hole, until the moment before fracture. The true circumferential tensile strain at fracture is defined as:

$$\varepsilon_1^{\mathrm{f}} = \ln\left(\frac{d_{\mathrm{f}}^{\mathrm{out}}}{d_0}\right), \tag{2}$$

where d_0 is the initial diameter and $d_{\mathrm{f}}^{\mathrm{out}}$ is the external diameter (at fracture). From the value determined with equation (2) it is possible to estimate the minor strain at the outer edge, which can be defined as:

$$\varepsilon_2^{\mathrm{f}} = -\left(\frac{R_{\theta+90}}{R_{\theta+90}+1}\right)\varepsilon_1^{\mathrm{f}}\,, \tag{3}$$

where $R_{\theta+90}$ is the *r*-value at 90 degrees to the cracking orientation [9]. This is related with the fact that the major strain occurs along the circumferential direction.

In order to locate any necking at the fracture location, two methods were used for post-mortem thickness measurements. The first assumes that the edge is under uniaxial tension conditions and the local thickness strain is used to determine the major and minor strains. The second combines circumferential and thickness strains into an equivalent strain. As in the other tests, post-mortem thickness measurements were also obtained by optical microscopy, as shown in the **Figure 2.13** [9].

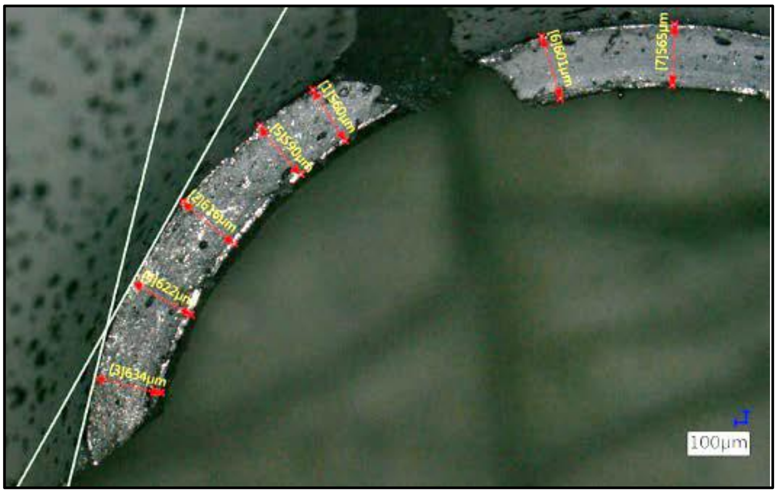

Figure 2.13. Fracture location in the hole expansion test and thickness measurement [8].

2.2.5. Fracture Characterization in Biaxial Tension

The determination of the FLD is standardized in the international standard 12004-2 [2] by two different experimental methods, the Marciniak- and the Nakazima-test. The use of these type of tests enables the description of monotonic strain paths from nearly equibiaxial tension up to uniaxial tension, under the same test conditions. This section describes both methods, following the approaches adopted by the benchmark committee.

2.2.5.1. Nakazima Test

The Nakazima test uses a spherical punch and a circular die, as shown in **Figure 2.14** (a) [2]. In order to generate different strain paths, the specimen geometry is modified, from a perfect circle into a specimen with a rectangular shape in the central part, as schematically shown in **Figure 2.14** (b). The change in width of the specimen, as shown in **Figure 2.15**, enables to cover the major-minor strain space from uniaxial tension to nearly equibiaxial. Nevertheless, it is important to mention that it is known that the results obtained are sensitive to the lubrication conditions, as a result of the contact between the punch and the blank [20]. In this context, another test was proposed: Marciniak test, which will be described latter. Nevertheless, the Nakazima test uses a simpler geometry than the one adopted in the Marciniak. Moreover, the Nakazima test can also be performed with a miniaturized set of tools, enabling the use of smaller samples. This was the approach followed in this benchmark, resorting to a punch with a radius of 5 mm, to perform only tests under biaxial conditions [21].

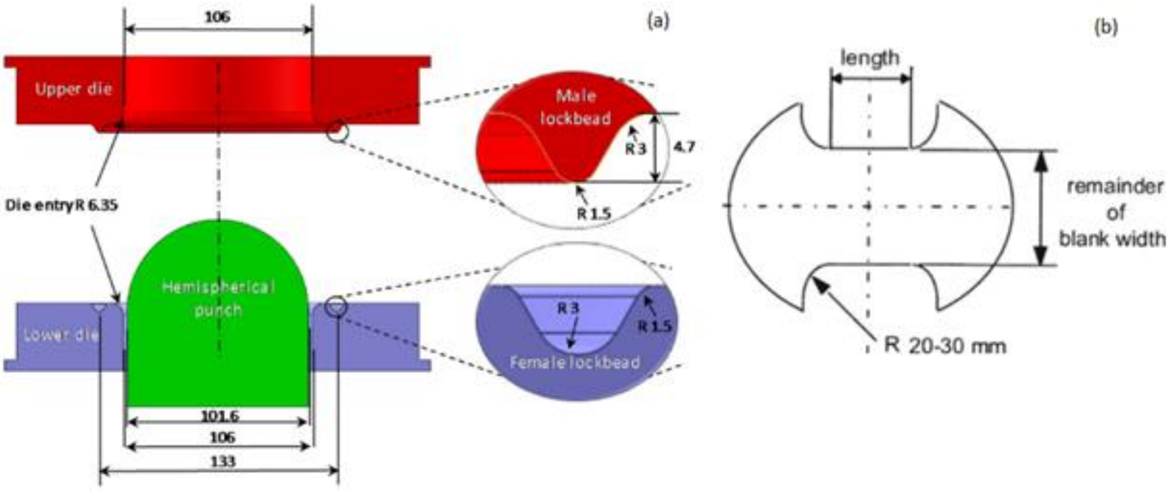
106
(a)
Upper die
Male lockbead
R3
4.7
R1.5
Die entry R 6.35
Hemispherical punch
Lower die
R3
R1.5
Female lockbead
101.6
106
133
(b)
length
remainder of blank width
R 20-30 mm

Figure 2.14. Nakazima test: (a) Schematic of the tool set (Adapted from [22]); (b) Shape of the specimens [2].

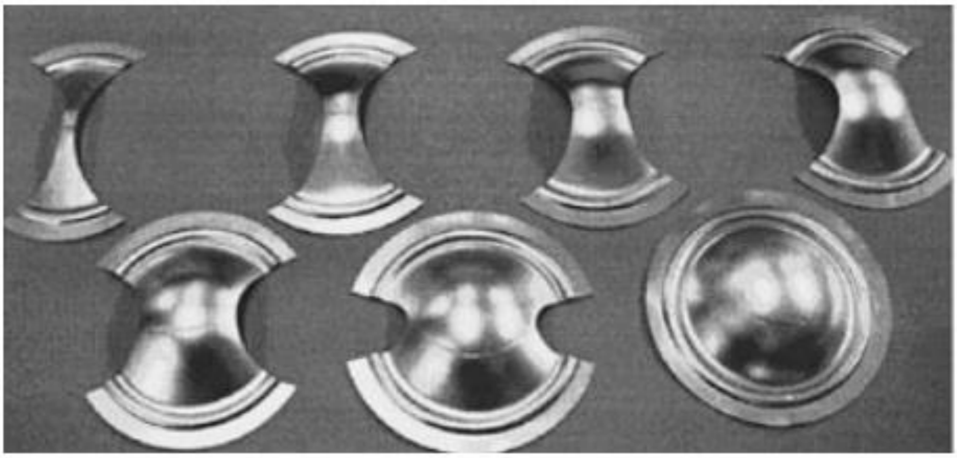

Figure 2.15. Set of specimens used in the Nakazima test for a complete FLD [2].

2.2.5.2. Marciniak Test

This test was proposed by Marciniak [23] and it is performed using a flat punch, instead of the spherical one used in the Nakazima test, as shown in the **Figure 2.16**.

Moreover, in order to minimize the influence of lubrication conditions, an intermediate blank, with a circular hole, is placed between the punch and the metallic specimen. This way the tearing in the material located in the planar bottom of the cup is guaranteed. In order to obtain different strain paths, punches with different cross sections can be used, such as circular, elliptical or rectangular. Nevertheless, the most used solution is to vary the width of the specimen, as schematically shown in the **Figure 2.14** (b), obtaining all regions of the FLD [2]. In the context of the current work, this test was selected for imposing the pre-strain because it is relatively easy to extract specimens for the following test, from the flat central region of the metallic pre-deform blanks.

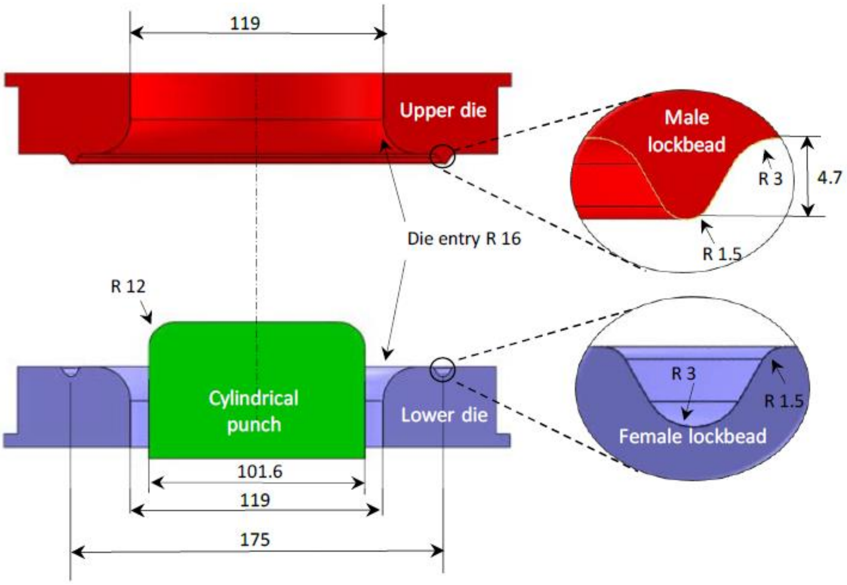

Figure 2.16. Schematic layout of the device used in the Marciniak test [21].

2.2.6. Fracture Characterization in nonlinear strain paths

As mentioned before, the aim of this benchmark is to evaluate the fracture model's ability to predict strain localization and fracture occurrence under nonlinear strain-paths. In this context, several tests were carried out to characterize the fracture strain under monotonous deformation trajectories, enabling the fracture models calibration. Moreover, experimental tests were performed considering a strain-path change. According to the preliminary instructions, the first strain path was always performed using the Marciniak's test, using different specimen geometries, to attain a pre-tension. The different trajectories considered are presented in **Table 2.1**, as well as the tests used to perform the first and second strain-path, until fracture [3]. This approach was adopted to guarantee the required specimen size, for instance, to perform the Nakazima with a miniaturized set of tools.

Table 2.1. Adapted table from the data provided by Numisheet 2020 benchmark 2 committee with the stages for nonlinear tests. [3].

Pre-strain	Second stage deformation to fracture
Uniaxial (TD) *	Equibiaxial using mini-Nakazima tool set
Plane strain in a 5.5 in specimen (TD) **	
Biaxial in a 6.5 in specimen (TD) **	

* Using uniaxial tensile test on a wide blank (250x70 mm)

** Using Marciniak tooling

3. CONSTITUTIVE MODELS

The constitutive models used in the numerical simulation of sheet metal forming processes consist basically of the laws that enable the description of the elastic, the plastic and the damage behavior. The description of damage can be performed either using a coupled or an uncoupled approach. In the first, the internal variable(s) used to represent damage affect the material elastoplastic behavior. In the uncoupled approach, the damage has no effect on the material behavior and, consequently, these types of models are usually named as fracture criterion. For metallic sheets, it is more or less consensual that the elastoplastic model controls the material behavior until the onset of necking. Therefore, the current study was performed without taking into account the damage behavior. For metallic sheets, the elastic behavior is assumed as isotropic. The Hooke's law is adopted, which requires de definition of the Young's modulus, that for DP1180 steel is $E = 202822\ MPa$, and of the Poisson coefficient, $\upsilon = 0.292$. The plastic behavior is defined by a flow rule, a hardening law and a yield criterion [24]. In the current study, an associated flow rule is adopted, meaning that the yield criterion has the dual role of plastic potential. The following sections present the details concerning the hardening laws and yield criteria considered in this work.

3.1. Hardening laws

The benchmark committee suggested the use of a hardening law that adds two well-known laws: Swift and Hockett-Sherby. The Swift's law is described as:

$$Y = K\left(\varepsilon_0 + \bar{\varepsilon}_{\mathrm{p}}\right)^n \,, \qquad \textbf{(4)}$$

where Y is the flow stress and $\bar{\varepsilon}_{\mathrm{p}}$ is the equivalent plastic strain. ε_0, K and n are material parameters, with the latter being commonly referred as the strain-hardening coefficients [25]. The initial yield stress is defined as $\sigma_0 = K(\varepsilon_0)^n$. The Hockett-Sherby hardening law corresponds to:

$$Y = A_H - B_H e^{\left(-C_H \bar{\varepsilon}_{\mathrm{p}}{}^{b_H}\right)} \,, \qquad \textbf{(5)}$$

where A_H, B_H, C_H and b_H are material parameters [3][26], such that the initial yield stress $\sigma_0 = A_H - B_H$. The material parameters for the combination of these laws were determined by benchmark committee, based on the uniaxial tensile test results (all directions) and on the results of the hydraulic bulge tests. **Figure 3.1** (a) shows the comparison between the experimental result and each individual law, as well as their sum, labelled as Swift+Hockett-Sherby. All series are labelled with BM to highlight that they correspond to the identification supplied by the benchmark committee. The combined law allows to describe the hardening behavior, but it is clear the discrepancy for low values of equivalent plastic strain. Unfortunately, the direct sum of these two laws is not implemented in DD3IMP. The option available corresponds to the weighted combination of the Swift and Voce law (S_V), where the latter is defined as:

$$Y = A - Be^{(-C\cdot\bar{\varepsilon}_\mathrm{p})}, \tag{6}$$

where A, B and C are material parameters [3][26], such that the initial yield stress $\sigma_0 = A - B$. The weighted combination of these two laws is defined as follows:

$$Y = \alpha\left[K\left(\varepsilon_0 + \bar{\varepsilon}_\mathrm{p}\right)^n\right] + (1-\alpha)\left[A - Be^{(-C\cdot\bar{\varepsilon}_\mathrm{p})}\right], \tag{7}$$

where α is the weighting parameter.

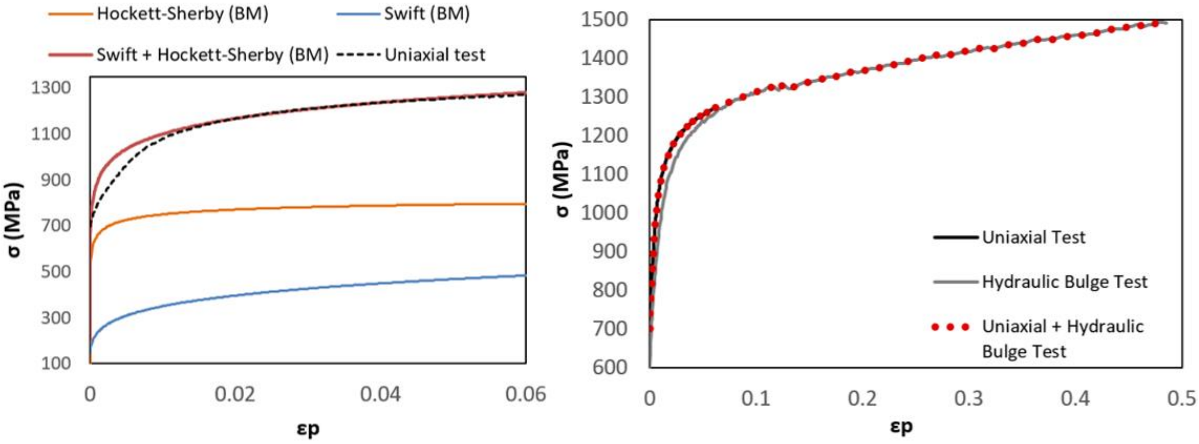

Figure 3.1. Comparison between experimental and numerical stress-strain: (a) Experimental data obtained from the uniaxial tensile test at RD and the numerical results obtained using the Benchmark parameters of Swift, Hockett-Sherby and the combined Swift with Hockett-Sherby law; (b) Experimental data from uniaxial test, bulge test and the combined curve using the uniaxial test results for the first part until 0.063 of equivalent plastic strain and the bulge test for the rest of the curve.

Since it was not possible to use the law suggested by the benchmark committee, it was decided to perform the identification of the parameters of the isotropic hardening laws available in DD3IMP, using the experimental results of the uniaxial tensile test at the RD, as well as from the bulge tests [3]. By adding the information from the bulge test, it is expected to improve the description of the hardening behavior, namely for a wider strain range, since the tensile specimens attain the onset of necking for very small strain values, as shown in the **Figure 3.1** (a).

The benchmark committee supplied three results for the uniaxial tensile test, at RD, as well as for the bulge test. The first step that had to be performed was to convert the true stress- true strain curves into true stress- equivalent plastic strain ones, assuming the von Mises yield criterion. This also involves the evaluation of the initial yield stress, i.e. the identification of the strain value corresponding to the transition between the linear elastic regime and the plastic one. To estimate the elastic limit, a parameter $\mathrm{d}E$ was defined, corresponding to the value of the Young modulus for every 10 experimental points. An average $\mathrm{d}E$ value was calculated in the central region of the linear elastic part. It was considered that the elastic regime ended when the $\mathrm{d}E$ value is less than 10% of the average value. This strain value was assumed as the elastic limit and a correction was made in the following points, in order to assure the proper representation of the equivalent plastic strain. This procedure was applied to both the uniaxial test results and the ones from the bulge test. **Figure 3.1** (b) exemplifies the true stress- equivalent plastic strain curves obtained following this procedure, for the uniaxial tensile test and the bulge test. Note that in this case, the extension of the hardening curve with the bulge test results does not requires any correction. Thus, the first points of the plastic strain region of the bulge test were replaced by the points of the plastic strain region of the uniaxial test. These curves were the ones used as input data for the hardening parameters identification procedure adopted, which will be described in the following sections [27].

3.1.1. Identification of the Swift law parameters

The Swift hardening law (see equation **(4)**) can be linearized as follows:

$$\ln(Y) = \ln(K) + n \cdot \ln(\bar{\varepsilon}_{\mathrm{p}}) \,, \tag{8}$$

This allows applying the Least Square Method to determine the coefficients of the polynomial function of degree one, $y = a_0 + a_1 x$, which minimizes the difference to all experimental points, using for instance Excel. **Figure 3.2** illustrates this procedure, considering only the results from the uniaxial tensile test, leading to the following parameters for Swift's law: $n = a_1$ and $K = \exp(a_0)$. The same procedure was repeated for the experimental data of the bulge test and the results are listed in the **Table 3.1**.

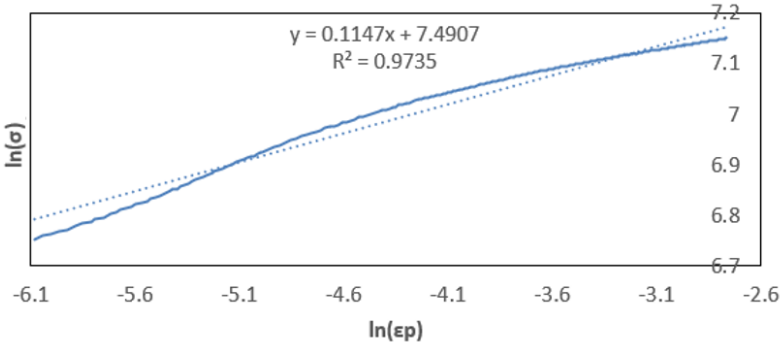

Figure 3.2. Linear regression of the set of points ln(σ) x ln(εp) obtained from the uniaxial test 1.

3.1.2. Identification of the Voce parameters

The identification of the parameters for the Voce hardening law was more challenging because the equation is more difficult to manipulate, since it is not possible to linearize. Thus, the identification was performed with the aid of the software Maple, through the nonlinear curve fitting option [28]. In a general sense, the objective consists of adjusting the parameters of the hardening law to best fit the experimental data set. The data set consists of n points (data pairs) $(\varepsilon_i^{\mathrm{p}}, \sigma_i)$, $i = 1, \ldots, n$, where $\varepsilon_i^{\mathrm{p}}$ is the independent variable and σ_i is the dependent variable, which has to be fitted. The model function has the form $\sigma(\varepsilon^{\mathrm{p}}, \boldsymbol{\beta})$ were $\boldsymbol{\beta}$ is the vector containing the material parameters. The fit of a model to a data point is measured by its residual, defined as the difference between the actual value of the dependent variable and the value predicted by the model:

$$r_i = \sigma_i - \sigma(\varepsilon_i^{\mathrm{p}}, \boldsymbol{\beta}). \tag{9}$$

The least-squares method finds the optimal parameter values by minimizing the sum of the squared residuals,

$$S_i = \sum_{i=1}^{n} (r_i)^2. \tag{10}$$

A standard measure of the goodness of fit for mathematical models fitted to experimental data by means of least squares regression is the coefficient of determination, which for nonlinear models should be defined as:

$$R^2 = 1 - \frac{\sum_{i=1}^{n} (r_i)^2}{\sum_{i=1}^{n} (\sigma_i - \sigma_m)^2}, \tag{11}$$

where σ_m is the mean of the experimental values.

The nonlinear curve fitting function randomly generates parameters that follow the experimental data provided in a minimally acceptable way. However, some refinements of the command were necessary, in order to reliably represent the mechanical behavior, such as the introduction of initial search values: 1500, 1000 and 1, for constants A, B and C of equation **(6)**, respectively. These values were selected based on values found in the literature for the same material [29]. The parameters obtained with this procedure for the Voce hardening law are listed in **Table 3.1**.

However, the Voce hardening law was not considered in its isolated form, but always combined with the Swift hardening law, as defined in equation **(7)**. The weighting factor α was calculated with the aid of the Solver function, available in Excel. It was determined such that the value of R^2 is minimized, considering always the experimental stress-strain curve build with the uniaxial tensile test and the bulge test results. The analysis of the R^2 values presented in **Table 3.1** for the Swift hardening law, R^2_{Swift}, and for the combined law (S_V), $R^2_{\text{Swift+Voce}}$, indicates that this approach leads to the improvement of the fit.

Table 3.1. Hardening laws parameters obtained from the experimental results of the uniaxial test (UN) and the bulge test (BI).

	Swift			**Voce**					
	n [-]	K[MPa]	ε_0[-]	A[MPa]	B[MPa]	C[-]	R^2_{Swift}[-]	α[-]	$R^2_{\text{Swift+Voce}}$[-]
UN	0.12	1802.8	0.000293	1242.3	500.8	99.9	0.901	0.390	0.982
BI	0.84	1574.5	1.5E-05	1392.3	615.4	30.4	0.966	0.565	0.980

3.1.3. Improvement of hardening law parameters

Figure 3.3 presents the comparison between the experimental and the fitted hardening laws. Despite the fact that the R^2 values are very close to 1, which would indicate that the curve presents a good approximation, it is possible to observe some discrepancies. **Figure 3.3** (a) shows that the combined law identified with the uniaxial tension test renders an excellent fit for an equivalent plastic strain lower that 0.06, but results in an underestimation of the hardening behavior for higher strain value (**Figure 3.3** (b)). On the other hand, the models that allow a better description of the hardening behavior for high values of equivalent plastic strain, present some deviation from the trend observed for the uniaxial tensile test. Therefore, some identification procedure was applied to the experimental data set that considers the uniaxial test for low strain values and from the ones from the bulge test for high values, as shown in the **Figure 3.1** (b). Note that it is known that the bulge test results are more sensitivity to inaccuracies in the measurement of the radius of curvature and the thickness, for low strain values [30].

The material parameters determined using the combined experimental data are shown in **Table 3.2**. As it is possible to see in **Figure 3.4**, although the R^2values are very close to the ones previously obtained using exclusively the bulge test results (see **Table 3.1**), the new set of parameters enable an improved fitting for the complete strain range. Nevertheless, it should be noted that, the Swift law overestimates the hardening behavior, while the combined law underestimates, for large strain values. Finally, the criterion for the onset of necking for a uniaxial tensile stress state states that it occurs for a strain $\varepsilon_{\mathrm{neck}}$ such that $d\sigma/d\varepsilon = \sigma$. According to this condition, for the Swift law $\varepsilon_{\mathrm{neck}}$ corresponds to 0.093 while for the combined law it is slightly smaller, with a value of 0.083.

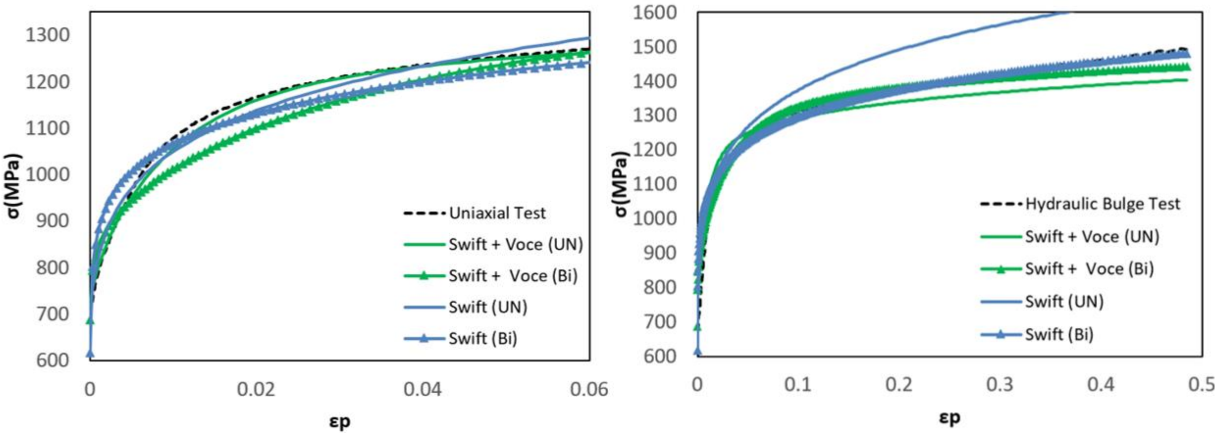

Figure 3.3. Comparison between experimental and numerical stress-strain curves: (a) experimental stress-strain curve of the uniaxial test with the hardening laws determined using either the uniaxial test or the bulge test results; (b) experimental stress-strain curve of the bulge test with the hardening laws determined using either the uniaxial test or the bulge test results.

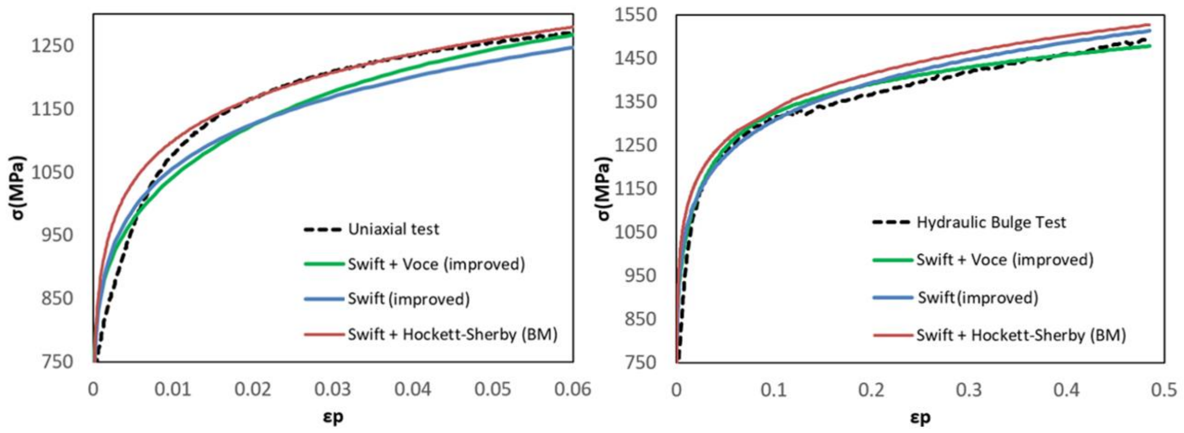

Figure 3.4. Comparison between experimental and numerical stress-strain curves: (a) experimental data from the uniaxial test with the hardening laws determined using the combined experimental data; (b) experimental data from the bulge test with the hardening laws determined using the combined experimental data.

Table 3.2. Improved hardening laws parameters.

	Swift			Voce					
	n [-]	K[MPa]	ε_0[-]	A[MPa]	B[MPa]	C[-]	R^2_{Swift}[-]	α[-]	$R^2_{\text{Swift+Voce}}$[-]
Improved	0.093	1619	0.0001	1383.1	542.6	36.1	0.966	0.73	0.985

3.2. Yield criteria

Among the yield criteria for which the Benchmark committee provided the set of anisotropy parameters, two were available in the software DD3IMP: the Hill 1948 and Barlat 1991. These yield criteria are briefly described in this section.

The Hill 1948 yield criterion was proposed as a generalization of the Huber-Mises-Hencky isotropic criterion for anisotropic materials, assuming the yield function as [5][2]:

$$F\left(\sigma_y-\sigma_z\right)^2+G(\sigma_z-\sigma_{\mathrm{x}})^2+H\left(\sigma_{\mathrm{x}}-\sigma_{\mathrm{y}}\right)^2+2L\tau_{\mathrm{yz}}^2+2M\tau_{\mathrm{zx}}^2+2N\tau_{\mathrm{xy}}^2 = Y^2, \tag{12}$$

where F, G, H, L, M and N are the anisotropy coefficients defined in the material axis. The normal and shear stress subscripts x, y, and z are related, respectively, to the rolling, transverse, and thickness directions of the metal sheet [25].

The Barlat 1991 yield criterion (Yld91) was proposed as a generalization for anisotropic materials of the Hershey isotropic criterion, which is based on the crystallographic structure of the material [5][2]. The yield criterion is defined by:

$$|S_1-S_2|^m+|S_2-S_3|^m+|S_3-S_1|^m=2\cdot Y^m, \tag{13}$$

where S_1, S_2 and S_3 are the principal stresses of the deviator stress tensor, obtained from the linear transformation of the Cauchy stress tensor, $\boldsymbol{\sigma}$, to an equivalent isotropic stress state, defined as follows:

$$\mathbf{S}=\mathbf{L}:\boldsymbol{\sigma}. \tag{14}$$

The tensor **L** can be defined, using Voigt notation, as follows:

$$\mathbf{L}=\begin{bmatrix} (c_2+c_3)/3 & -c_3/3 & -c_2/3 & 0 & 0 & 0 \\ -c_3/3 & (c_3+c_1)/3 & -c_1/3 & 0 & 0 & 0 \\ -c_2/3 & -c_1/3 & (c_1+c_2)/3 & 0 & 0 & 0 \\ 0 & 0 & 0 & c_4 & 0 & 0 \\ 0 & 0 & 0 & 0 & c_5 & 0 \\ 0 & 0 & 0 & 0 & 0 & c_6 \end{bmatrix}, \tag{15}$$

where $c_i, i=1,\dots,6$ are the anisotropy coefficients [31]. The value of the exponent m is based on the crystallographic structure (m = 6 for BCC materials and m = 8 for FCC materials)[5][2]. As previously mentioned, the parameters of the yield criteria were provided by the benchmark committee, which are listed in Table 3.3 for each criterion.

The comparison between experimental and predicted in-plane variation of the normalized yield stress and r-value is shown in **Figure 3.5** (a) and (b), respectively. Globally, both yield criteria overestimate the increasing trend for the yield stress while the r-values predicted by both criteria overlap and are very close to the experimental values provided by the benchmark committee, with a slight deviation only for angles of 30 and 60 degrees. The benchmark committee provided only yield stress in-plane variation for a strain value of 0.2%. Thus, in the **Figure 3.6** it is plotted the comparison between the experimental and predicted yield stress distribution for an equivalent plastic strain of 0.2%. The figure also shows the initial yield stress in-plane distribution to highlight the different hardening behavior predicted by both hardening laws (see also **Figure 3.4**). The differences observed in the initial yield stress become less evident for slightly higher strain values, but the trend changes with the hardening behavior. The results highlight that the differences are less relevant for an equivalent plastic strain of 0.2%. In fact, as shown in **Figure 3.6**, the differences in the trend can be quite sensitive to the value selected for the equivalent plastic strain.

Table 3.3. Parameters of the yield criteria Hill 1948 and Barlat 1991 provided by the benchmark committee.

Hill 1948					
F[-]	G[-]	H[-]	L[-]	M[-]	N[-]
0.401317	0.529207	0.470793	1.5	1.5	1.302234

Barlat 1991						
c_1[-]	c_2[-]	c_3[-]	c_4[-]	c_5[-]	c_6[-]	m[-]
0.9221	1.0225	0.9772	1	1	0.9476	6

Figure 3.5 (c) shows the yield surfaces for the two yield criteria projected in the plane corresponding to σ_{TD}-σ_{RD}, assuming that all other stress components are null. Since these surfaces are plotted for a null value of the equivalent plastic strain, it is possible to observe that the plastic deformation will occur for lower stress values when the Swift law is selected. Regarding the differences between the two yield criteria, the Barlat91 criterion will also lead to initial yielding at lower stress values, particularly around plane strain stress states.

In order to better understand the differences between both yield criteria, **Figure 3.7** presents the strain ratios distribution as a function of the loading direction (φ), defined by equation **(16)**, obtained analytically with the Hill48 and the Barlat91 yield criterion. The normal to the yield surface defines the ratio between the two in-plane strains: $\varepsilon_{\mathrm{RD}}$ and $\varepsilon_{\mathrm{TD}}$. From this ratio it is possible to determine which one of these two in-plane strains will be the highest, ε_1, and the lowest, ε_2. The strain occurring in the thickness direction, ε_t, can always be estimated based on the condition of volume conservation.

$$\varphi = \tan^{-1}\left(\frac{\sigma_{\mathrm{TD}}}{\sigma_{\mathrm{RD}}}\right), \tag{16}$$

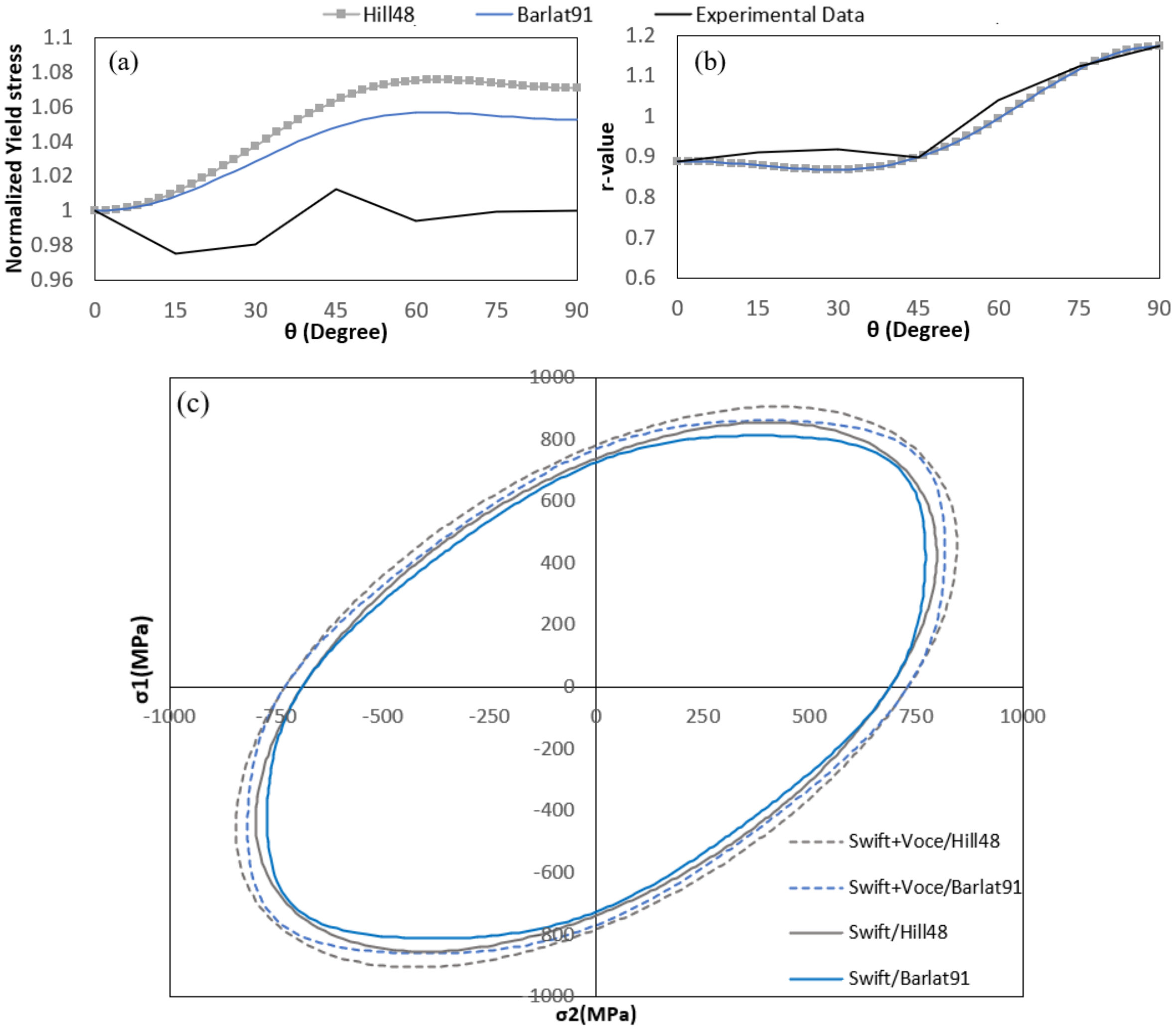

Figure 3.5. In-plane variation of the: (a) Normalized yield stress – θ (angle from the RD). (b) *r*-value – θ. (c) Yield surface assuming plane stress conditions with the $\boldsymbol{\sigma_3 = 0}$.

Figure 3.7 (a) presents the $\varepsilon_2/\varepsilon_t$ ratio, which corresponds to the r-values for the loading direction of 0º and 90º. This figure highlights that both yield criteria lead also to a similar ratio for the equibiaxial stress state (loading direction of 45º). Besides, the plane strain condition along RD occurs for both yield criteria for a similar loading direction of approximately 28º, while for TD it occurs at approximately 61º. Also, it is observed that, for stress states between uniaxial tension and plane strain, the $\varepsilon_2/\varepsilon_t$ is higher for the Hill48 yield criterion, which indicates that for a similar in plane minor strain the material will deform less through the thickness direction. The opposite is observed for stress states between plane strain and equibiaxial tension.

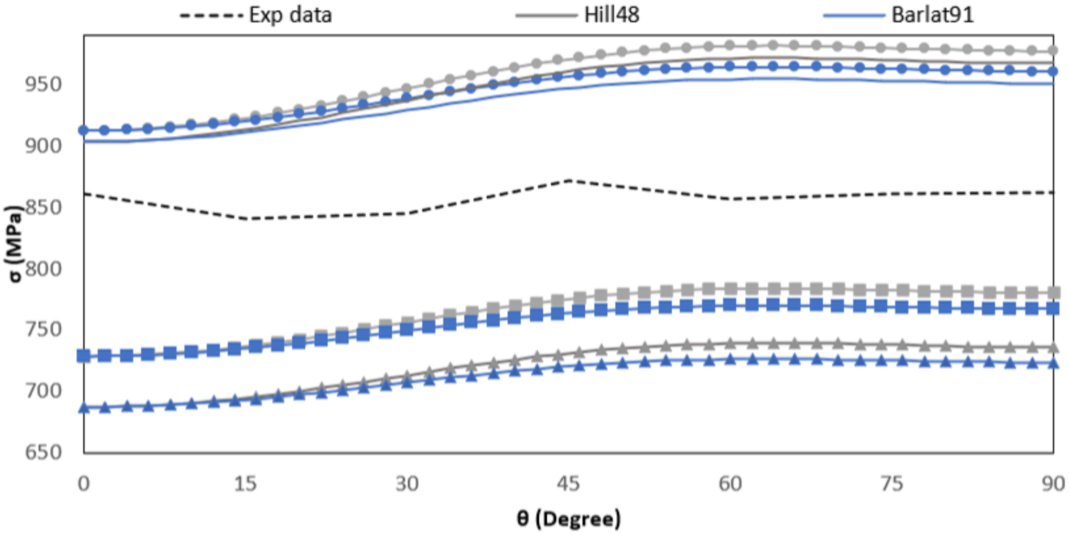

Figure 3.6. Comparison between experimental and numerical in-plane variation of the yield stress, comparing different combinations of yield criteria and hardening laws. Continuous line: Swift+Voce 0.2%; circle marker: Swift 0.2%; square marker: Swift+Voce; triangular marker: Swift.

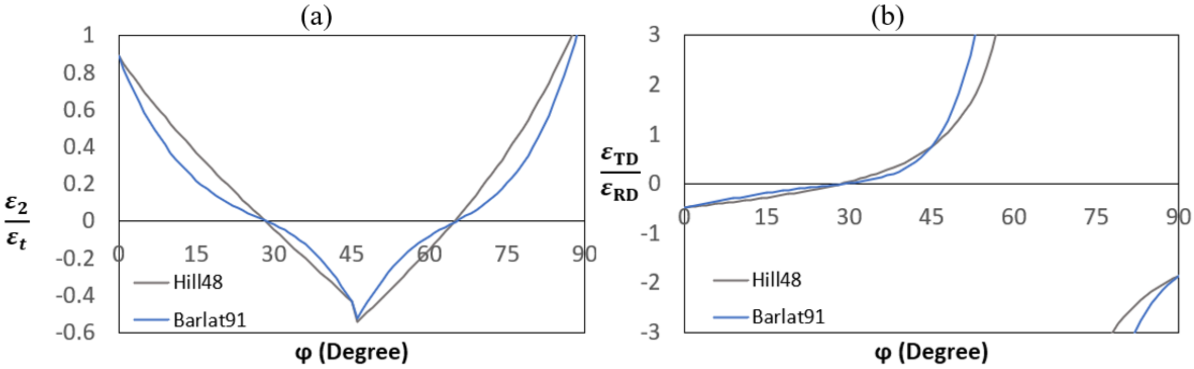

Figure 3.7. Strain ratio evolution as a function of the loading direction obtained analytically with the Hill48 and the Barlat91 yield criterion: (a) ratio between the minor and the through-thickness strain; and (b) ratio between the strain in the transverse and the rolling directions.

Figure 3.7 (b) presents the $\varepsilon_{\mathrm{TD}}/\varepsilon_{\mathrm{RD}}$ ratio, which corresponds to the biaxial value for a loading direction of 45º. As previously mentioned, both yield criteria lead to a similar value, which can be confirmed in the figure to be of approximately 0.76. This figure is also interesting because it allows the analysis of the slope of the $\varepsilon_1/\varepsilon_2$ strain paths expected for specific loading directions. Thus, for uniaxial tension along RD, the strain path will present a slope equal to approximately -2.1 (=1/(-0.47)) for both yield criteria, since the *r*-value for this direction is lower than 1.0 (slope of -2.0). For uniaxial tension along TD, the strain path will present a slope equal to approximately -1.9 for both yield criteria, since the *r*-value for this direction is higher than 1.0. For equibiaxial tension, the slope is of approximately 1.3 (=1/(0.76)).

4. NUMERICAL MODEL

The numerical models for analyzing the evolution of the strain path under some specific conditions were built, as described in this chapter. All numerical simulations were performed with the in-house finite element solver DD3IMP (Deep Drawing 3D IMPlicit) [32][33]. The mesh generation, for both the tools and the blanks, and the post processing analysis of the results was performed with the help of the software GID [34].

In order to reduce the computational time, only a quarter of each mechanical test was modelled, taking advantage of the geometrical, loading and material symmetry conditions. This implies that symmetry boundary conditions were always applied to the surfaces of the blank located in the symmetry plane. The blank sheet was always discretized with 3D 8-node hexahedral finite elements, combined with a selective reduced integration technique [35]. The mesh of the blank sheet is always composed of two layers through the thickness, which allows an accurate evaluation of the through-thickness stress gradients. The construction of the mesh for the blank resorted to structured meshes, with zones with an element size defined based on the contact conditions. Moreover, a smaller element size was also applied in the central area of the blank, where it is intended to follow the evolution of the strain path. In some cases, a mesh sensitivity analysis was performed, but in this chapter, only the selected meshes are reported. The blank rolling direction was always assumed to be oriented along *Ox*.

All forming tools are considered rigid and were modelled by Nagata patches [36]. This approach requires the definition of the CAD model for the tools (IGES file), as well as the finite element mesh of the outer surface. The finite element mesh adopted can be coarse and the rules proposed for its construction in [37] were followed. The contact with friction conditions were modelled with the Coulomb friction model. As previously mentioned, these tests are performed using lubricants to reduce friction, in order to minimize the influence of this parameter in the FLD [38]. Thus, the numerical simulations were mainly performed using a null friction coefficient value. This simplification can also help reducing the computational time, although this depends on the influence on the overall displacement of the blank.

The numerical simulations were mainly performed until the occurrence of strain localization in the specimen. This means that, in general, the final displacement imposed to the punch was not fixed to a constant value, since it is known that the plasticity model affects the strain localization.

4.1. Monotonic strain paths

The analysis of monotonic strain paths was mainly performed with the Marciniak test. The dimensions of the Marciniak tool set are shown in **Figure 2.16**. However, as previously mentioned, in this test an intermediate blank, with a circular hole, is placed between the punch and the metallic specimen, to minimize the influence of friction. This implies that during the test there is contact between two deformable bodies, the two blanks. In order to minimize the computational time, the numerical model adopted neglect the deformation of the intermediate blank, which was replaced by an offset to the dimensions of the punch and lower die, equal to the thickness of the intermediate blank.

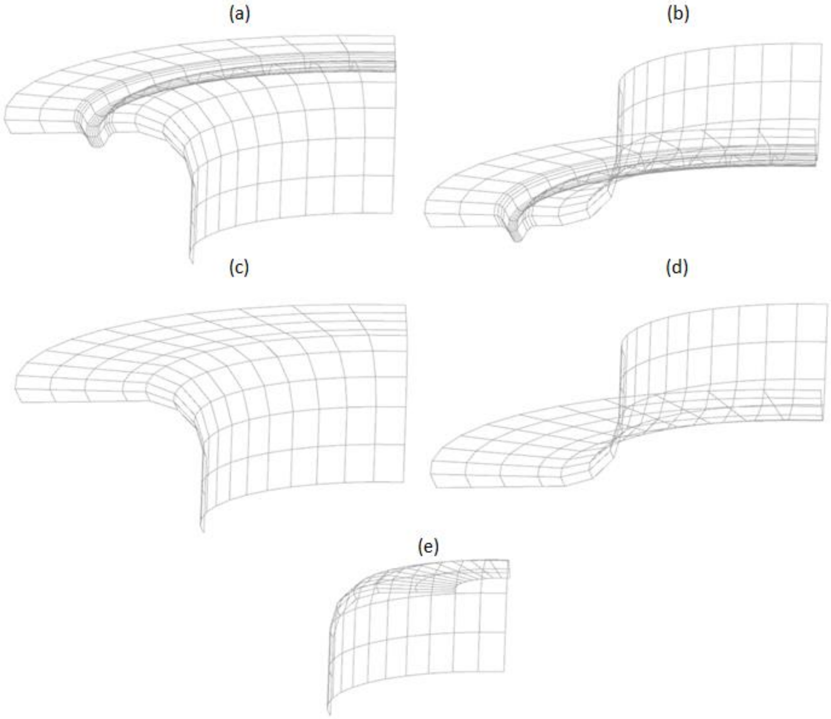

Figure 4.1: Meshes adopted for the tools of the Marciniak test: (a) Blank-holder (with draw bead); (b) Die (with draw bead); (c) Blank-holder (without draw bead); (d) Die (without draw bead); and (e) Punch.

Figure 4.1 shows the meshes adopted for the Marciniak tools. The tools present a draw bead to restrain the radial displacement of the blank. The numerical simulation of the draw bead requires the use of a refined mesh in the contact area, due to the small radius presented by this detail. Therefore, in order to reduce the computational time, the geometrical draw bead can be replaced by a boundary condition, imposing a null displacement to the external radius where the draw bead is located. The impact of this simplification on the results depends on the influence of the bending step, imposed by the draw bead, on the central area of the blank [39]. Therefore, the two models were considered and **Figure 4.1** also presents the tools used in the numerical model that uses simplified boundary conditions to represent the draw bead.

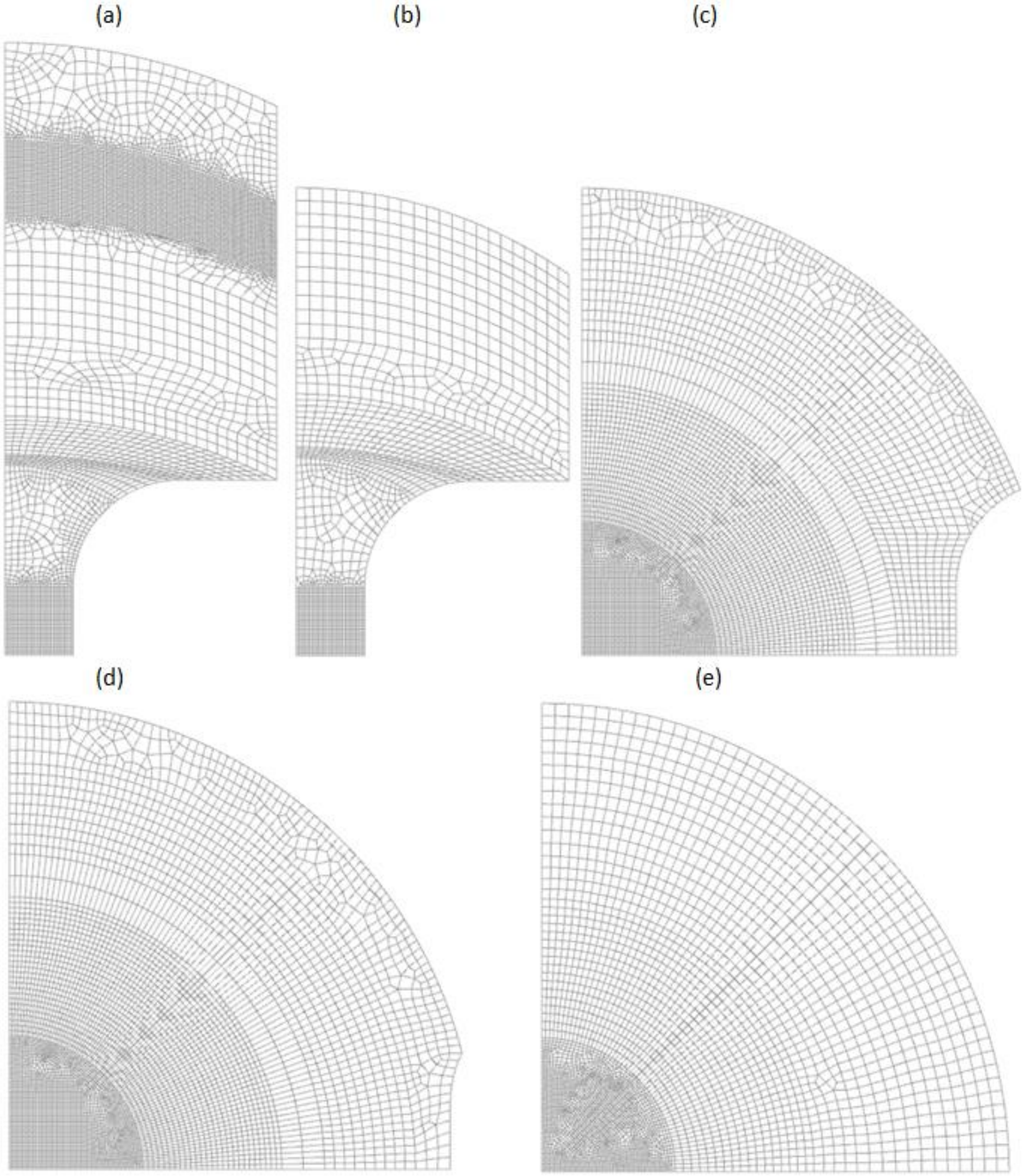

Figure 4.2: Meshes adopted for the blank of the Marciniak test: (a) 1 inch width (with draw bead); (b) 1 inch width (without draw bead); (c) 5.5 inches width; (d) 6.5 inches width; and (e) 8 inches width.

As previously mentioned, different monotonic strain paths can be achieved by changing the blank shape (see **Figure 2.15**). In this study, four different shapes for the blank were considered. The nomenclature used to identify each shape is the same used in the benchmark, i.e. the width of the specimen in inches. The four different widths considered were 1, 5.5, 6.5 and 8, since they enable covering the strain space from uniaxial tension until equibiaxial stress. **Figure 4.2** shows these geometries, as well as the meshes adopted in the numerical models. The blank with a width of 1 inch was used to analyze the influence of the presence of the draw bead in the numerical model. Thus, **Figure 4.2** shows the two meshes adopted for this blank. The simulations were always performed considering a constant blank-holder force of 160 kN (1/4 model) [21].

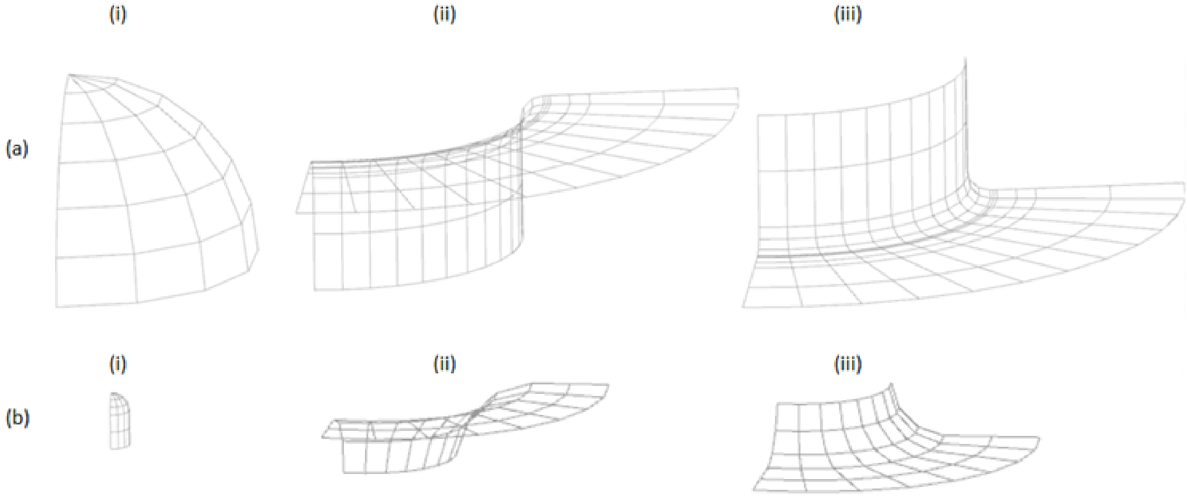

Figure 4.3: Meshes adopted for the tools of the (a): Nakazima test: (i) Punch (101.6 mm); (ii) Blank-holder; and (iii) Die; (b) Mini-Nakazima test: (i) Punch (5 mm); (ii) Blank-holder; and (iii) Die.

The analysis of the equibiaxial strain path was also performed considering the Nakazima and the Mini-Nakazima test conditions. The tools used for the Nakazima test are shown in **Figure 2.14** and the corresponding models are presented in **Figure 4.3** (a). In this case, the draw bead was always replaced by adequate boundary conditions. The Mini-Nakazima tool set is the same used for the Hole Expansion test (see **Figure 2.12**). However, the conical punch with a 3 mm radius on the tip is replaced by a spherical punch with a radius of 5 mm. The corresponding models for the Mini-Nakazima are presented in **Figure 4.3** (b). The simulations were always performed considering a constant blank-holder force of 160 kN (1/4 models) for both Nakazima and Mini-Nakazima [9], [40]. The Nakazima tests were performed considering the equibiaxial stress state, with a circular blank identical to the one used in the Marciniak test, whose mesh is presented in **Figure 4.4** (a). Regarding the Mini-

Nakazima test conditions, it was used to reproduce the equibiaxial monotonic strain path, using the geometry and specimen discretization shown in **Figure 4.4** (b). Moreover, it was also used to reproduce the equibiaxial strain path after a pre-strain, as indicated in **Table 2.1**. The pre-strain was performed using both the Marciniak test conditions and a wide blank submitted to uniaxial tensile test conditions. For the Marciniak test conditions, the blank geometry shown in **Figure 4.2** was adopted.

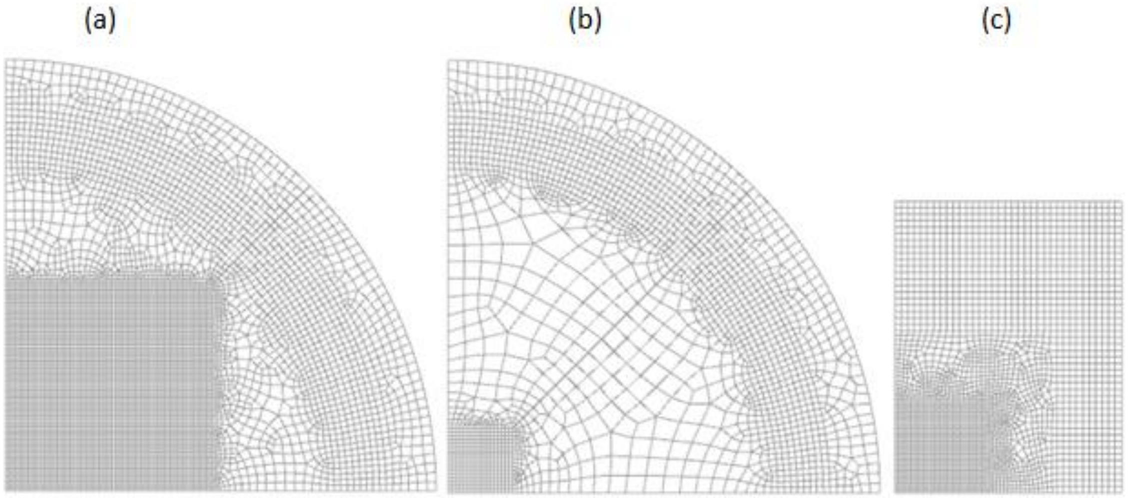

Figure 4.4: Mesh adopted for the blank: (a) Nakazima test (8 inches width); (b) Mini-Nakazima test with 8 inches width; (c) Specimen used for uniaxial pre-strain followed by equibiaxial trajectory.

4.2. Nonlinear strain paths

The complex strain paths considered in the analysis comprise mainly two monotonic branches. The first branch, also called pre-strain, was attained using two different approaches. The first approach involves a uniaxial tensile test on a wide blank, i.e. the pre-strain follows the uniaxial tension paths. In the second approach, the pre-strain is performed using the Marciniak test conditions, in particular the specimens with a width of 5.5 and 6.5 inches. The following subsections describe the specific details of the numerical models adopted for each approach. It should be mentioned that both approaches try to resemble the tests conditions, i.e. they consider the unloading stage that occurs between the two monotonic branches.

4.2.1. Pre-strain in uniaxial tension

The numerical model considers a total of four phases: (i) pre-strain loading; (ii) pre-strain unloading; (iii) blank-holder closure and (iv) punch displacement. The blank used in the numerical model is a rectangular geometry with a length of 90 mm in length and a width of 70 mm. Note that in the experimental procedure the blank submitted to uniaxial tension had a length of 250 mm and a width of 70 mm. Then, the specimen geometry used in the Mini-Nakajima test was cut from that metallic sheet. The numerical model considered a smaller length, in order to avoid any trimming operations. The discretization of the specimen adopted in the model is shown in **Figure 4.4** (c).

For the uniaxial tensile pre-strain phase, a displacement of 2.7 mm was imposed in the direction along the length of the specimen, in order to obtain a final major strain of 6%, as defined by the benchmark committee [41]. Note that this value of displacement was determined based on a preliminary numerical simulation. The second phase corresponds to the removal of the imposed displacement, until the force attains a null value. The third phase corresponds to the closure of the blank-holder, until the predefined force is attained. The last phase corresponds to the punch displacement.

4.2.2. Pre-strain using Marciniak test conditions

Adopting this approach, the pre-strain is attained with the Marciniak test conditions (see **Figure 4.1**, without draw bead) and the second strain path with the Mini-Nakazima (**Figure 4.3** (b)). The specimens used presents 5.5 inches width (**Figure 4.2** (c)), which imposes a pre-strain path in approximately plane strain conditions; and the other with a width of 6.5 inches (see **Figure 4.2** (d)), for a pre-strain under biaxial condition. The numerical model considers four phases: (i) closure of the blank-holder of the Marciniak tool; (ii) displacement of the Marciniak punch; (iii) closure of the Blank-holder of the Mini-Nakazima tool; and (iv) displacement of the Mini-Nakazima punch. In order to impose major true strains identical to the ones provided by the benchmark committee for the Marciniak test conditions, the punch displacements applied were of: 11.05 mm, for the plane strain condition; and 18, 18.22 and 18.45 mm, respectively for the Swift/Hill48, Swift/Barlat91 and Swift+Voce/Barlat91 models, for the biaxial condition.

The numerical models consider the existence of all tools from the beginning. The tools of the Marciniak test are active during the first two phases and afterwards are defined as inactive. The opposite happens for the Mini-Nakazima tools. Nevertheless, this implies that the initial position Mini-Nakajima tools must be defined taking into account the deformation of the blank in the previous phases. An example of the assembly model is shown in the **Figure 4.5**, highlighting the necessary correction to the initial position of the Mini-

Nakazima tools. It should be mentioned that when the tools from the Marciniak test are deactivated, the blank has no contact with the other tools (or the contact occurs with very low forces). This means that in the first increments of this phase the sheet springbacks. However, the boundary condition associated to the draw bead remains active during the simulation. The results do not seem to be affected by this condition due to the restraining force imposed by the blank-holder of the Mini-Marciniak.

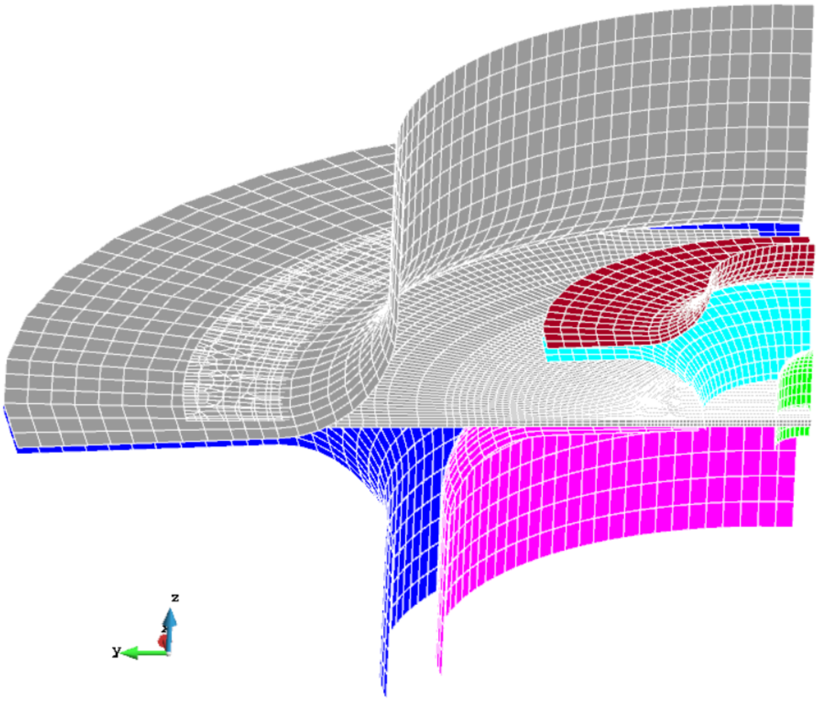

Figure 4.5: Assembly used for the model with the specimen with 5.5 inches, using the Marciniak tool (dark-blue: Blank-holder; grey: Die and pink: Punch) followed by Mini-Nakazima tool (light-blue: Blank-holder; brown: Die and green: Punch). The mesh shown in this figure is constructed in GID only for visualization purposes.

5. RESULTS AND DISCUSSIONS

In this section, the numerical results are analyzed and compared with the experimental ones, in order to access the ability of the constitutive models to describe the material plastic behavior. The numerical simulations were always performed considering the two yield criteria previously presented in section **3.2**: Hill 1948, which will be labelled Hill48 and the Barlat 1991, designated as Yld91. Both are tested combined with the Swift hardening law. For the Yld91, the combined Swift plus Voce hardening law is also considered and will be labelled S_V. All simulations were run on hardware computer equipped with an intel i5-7300HQ processor, with four 2.50GHz cores, 16GB of RAM memory and a 64-bit operating system.

The results reported by the Benchmark committee correspond to the strain measured at the specimen's center. Therefore, the data for the integration point (Gauss point) closer to this location was collected in all numerical simulations performed. This data includes the stress and strain paths as well as the evolution of the stress triaxiality and Lode parameter, which are commonly used to define the stress state in uncoupled ductile fracture models. The stress triaxiality and Lode parameter are defined in **APPENDIX A,** as well as their values for tests performed under plane stress conditions. Besides these results, the evolution of the punch force with its displacement is also presented to help undertaking the differences between the constitutive models.

As mentioned in the previous chapter, both the Marciniak and the Nakazima tests are performing using a drawbead to restrain the material flow. Thus, the influence of the geometrical drawbead was assessed for the 1 inch width specimen in the Marciniak test. The same geometry was also used to evaluate the impact of the friction coefficient. This specimen was selected because it is the one reported has being closer to the uniaxial tension stress state, for which both yield criteria are expected to lead to similar strain paths (see **Figure 3.7**).

5.1. Monotonic strain paths simulations

5.1.1. Marciniak tests

5.1.1.1. Specimen with 1 inch width (uniaxial tension)

5.1.1.1.1. Influence of the drawbead

The specimen with 1 inch width was used to assess the influence of the drawbead on the numerical results. Accordingly, the two sets of forming tools are adopted, namely the upper/lower die with and without drawbead. In both cases, a friction coefficient equal to 0.15 was used. **Figure 5.1** displays the strain paths obtained numerically and experimentally. For both hardening laws and yield criteria analyzed, the effect of the drawbead on the predicted strain path is negligible, for an equivalent plastic strain value lower than 0.016, for which the predicted strain paths are almost overlapping. This corresponds to a punch displacement of approximately 5.75 mm.

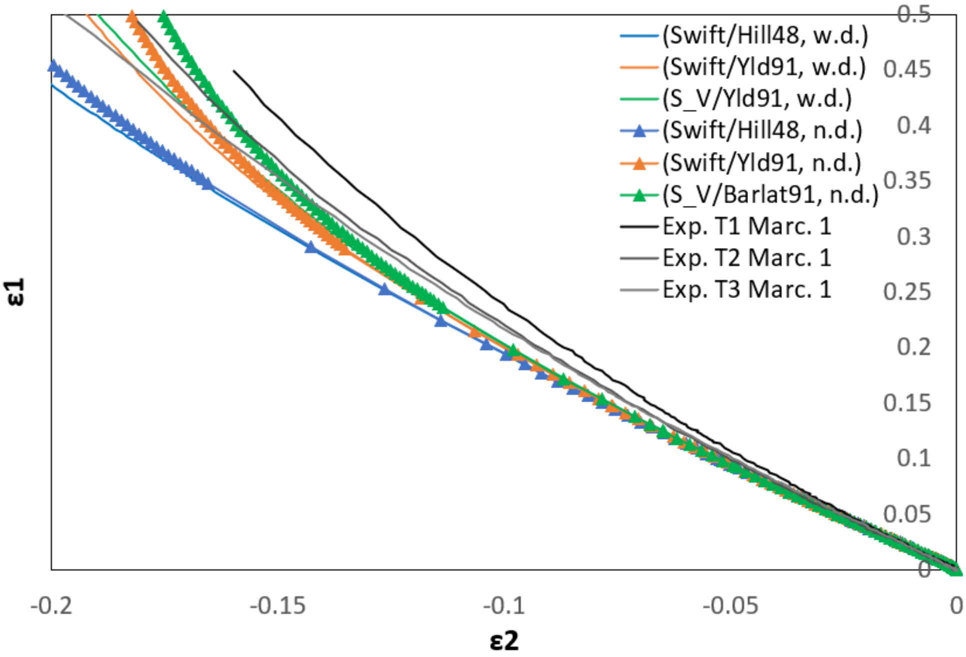

Figure 5.1. Evolution of the major strain-minor strain in the Marciniak test using the specimen with 1 inch width, comparing numerical predictions with experimental results. Simulations with drawbead (w.d.) and without drawbead (n.d.), both using a friction coefficient of 0.15.

Figure 5.2 shows the punch force as a function of punch displacement, comparing the different constitutive models and the effect of drawbead. The deformation generated by the geometrical drawbead makes the specimen center lifting upwards. Thus, when the punch starts its displacement from the reference position it has no contact with the blank. The results shown in **Figure 5.2** are corrected in order to guarantee that the null displacement corresponds to the instant previous to the first increment of punch force. The closing of the geometrical drawbead generates a plastic strain in the major strain axis of

0.013 and an equivalent plastic strain of 0.08. Nevertheless, as shown in **Figure 5.1** its impact on the strain path during the forming step seems negligible.

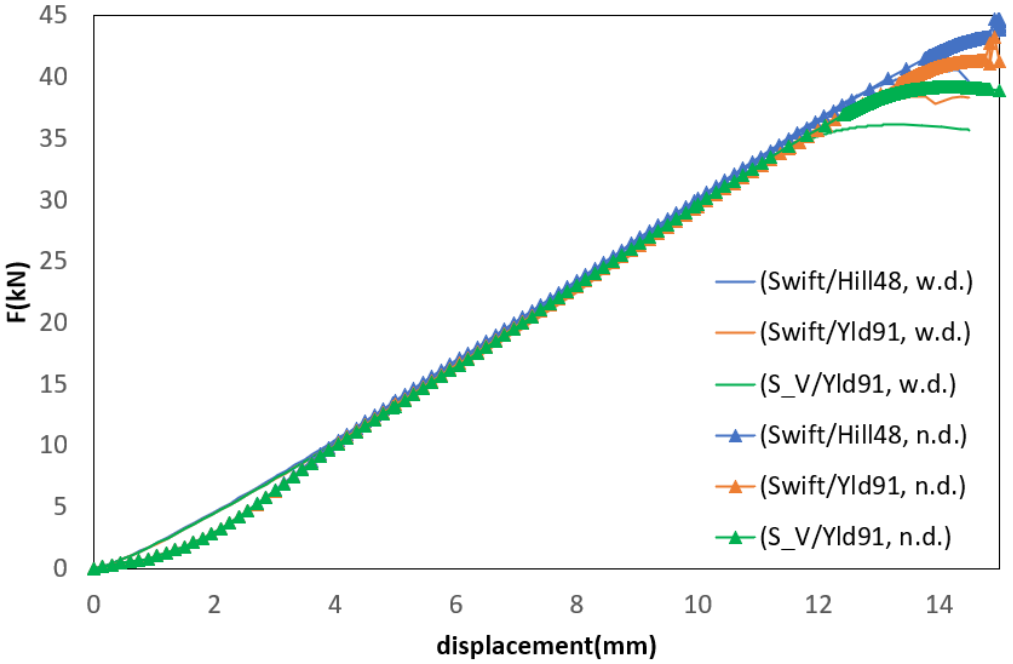

Figure 5.2. Evolution of the predicted punch force in the Marciniak test specimen with 1 inch width, comparing the situations with drawbead (w.d.) and without drawbead (n.d.) (friction coefficient of 0.15).

Figure 5.2 shows that the onset of necking occurs for lower punch displacements when using the forming tools with the geometrical drawbead. In fact, the maximum punch force obtained is smaller when the tools have a geometrical drawbead. The maximum punch forces found without the geometrical drawbead were 43.3, 41.3 and 39.15 kN, respectively for the Swift/Hill48, Swift/Yld91 and S_V/Yld91, a difference of 6.46%, 6.92% and 7.66% in relation to results with the geometrical drawbead. It should be mentioned that the oscillations on the punch force at the of the simulations performed without drawbead are caused by the reduction of the increment size to reach convergence.

Figure 5.3 presents the evolution of both stress triaxiality and Lode parameter without punch displacement correction, evaluated in the center of the specimen. Before the onset of necking, all models have similar values for both parameters, close to the ones expected for the uniaxial tension stress state (reference values presented in **Table A.1** of Appendix A), i.e. around 0.33(1/3) for triaxiality and 1.0 for the Lode parameter. As previously mentioned, all models with the geometrical drawbead enter the plastic regime during the drawbead closure. This does not correspond to a null punch displacement only because of the lifting induced to the blank, which delays the contact between the punch and the blank. After the onset of necking, the triaxiality increases and the Lode parameter decreases, i.e. the stress state change to one closer to plane strain, as also highlighted in **Figure 5.1**. The differences between the models with and without the geometrical drawbead are higher when the Yld91 yield criteria is used, which seems to be correlated with its shape being more sensitive to small changes of the stress state, for a loading angle of 90º (see **Figure 3.7**). This figure indicates that for a small variation in the loading direction, the Yld91 will predict larger differences in the thickness strain than the Hill48 yield criterion.

Figure 5.4 shows the distribution of the equivalent plastic strain in the specimen for 15 mm of punch displacement. Globally, the equivalent plastic strain predicted by the model using the geometrical drawbead is larger than the one predicted with the boundary condition, which is a consequence of the pre-strain generated during the geometrical drawbead closing. Considering the geometrical drawbead, the maximum equivalent plastic strain is 1.44, 1.66 and 2.09 for the models Swift/Hill48, Swift/Yld91 and S_V/Yld91, respectively. This is a consequence of the onset of necking occurring for lower punch displacements when the Yld91 criterion is adopted, particularly when using the combined hardening law. This result is coherent with the analysis made for the uniaxial tensile test, in section **3.1**. Therefore, the same trend is observed for the results without the physical drawbead. In brief, both models seem to impose a similar constrain to the material flow, leading to similar strain paths, enabling the prediction of the strain localization, without taking into account any damage model. However, neglecting the pre-strain induced by the geometrical drawbead leads to an overestimation of the equivalent plastic strain attained with a linear strain path. In fact, it leads to an underestimation of the plastic work, as also highlighted in the punch force evolution in the beginning of its displacement (see **Figure 5.2**).

The CPU and Wall times of each simulation are displayed in the **Table 5.1**. The simplification performed by removing the geometrical drawbead resulted in a reduction in the CPU time of 86.7%, 81% and 77.5% respectively for the model Swift/Hill48, Swift/Yld91 and S_V/Yld91. For the present work, the substantial reduction in the computational time, with an almost negligible difference in the predicted strain paths, justifies the use of simplification, a conclusion similar to that found in the work by Alves et al [39]. Therefore, all other numerical simulations were performed without considering the geometrical drawbead.

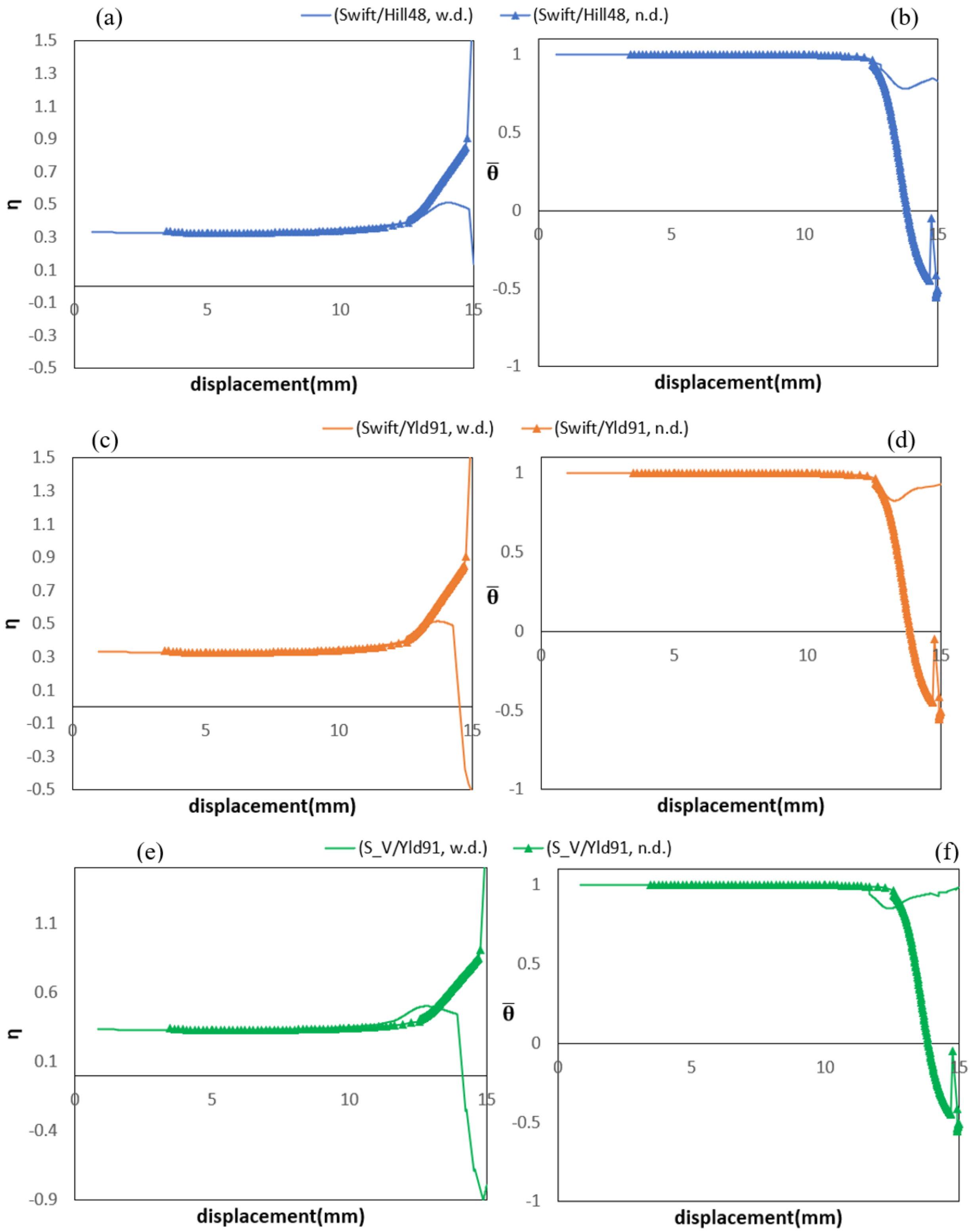

Figure 5.3. Evolution of triaxiality (a, c and e) and Lode parameter (b, d and f) with the punch displacement in the Marciniak test specimen with 1 inch width from simulations with drawbead (w.d.) and without drawbead (n.d.) (all with friction coefficient of 0.15).

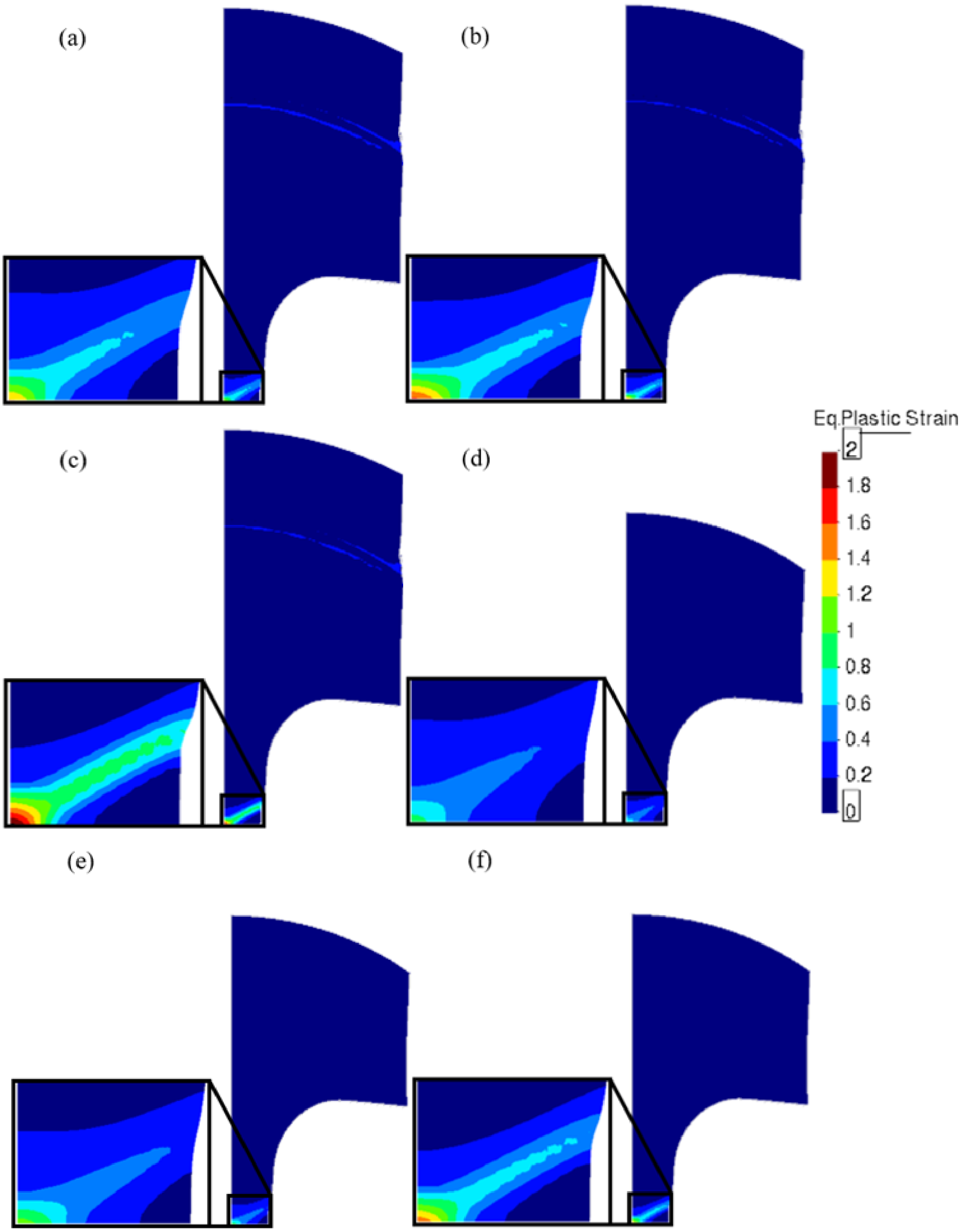
(a)
(b)
(c)
(d)
(e)
(f)
Eq.Plastic Strain
2
1.8
1.6
1.4
1.2
1
0.8
0.6
0.4
0.2
0

Figure 5.4. Equivalent plastic strain distribution in the Marciniak test specimen with 1 inch width: With drawbead (a) Swift/Hill48, (b) Swift/Yld91, (c) S_V/Yld91; without drawbead (d) Swift/Hill48, (e) Swift/Yld91, (f) S_V/Yld91.

Table 5.1. Computational times of the Marciniak test with and without drawbead.

	With drawbead		Without drawbead	
Model	**Wall Time (s)**	**CPU Time (s)**	**Wall Time (s)**	**CPU Time (s)**
Swift/Hill48	2719	8434	311	1118
Swift/Barlat91	3260	10523	748	1999
Swift+Voce/Barlat91	4981	12500	1115	2807

5.1.1.1.2. Influence of the friction coefficient

The influence of the friction coefficient on the numerical solution is evaluated using the same specimen (1 inch width). Adopting the model without drawbeads, the frictionless condition is compared with the constant value for the friction coefficient of 0.15. **Figure 5.5** shows both numerical and experimental results of major strain-minor strain evolution. The effect of the friction coefficient on the strain measured in the center of the specimen is negligible, i.e. the curves are almost overlapped with a slight difference after the onset of necking.

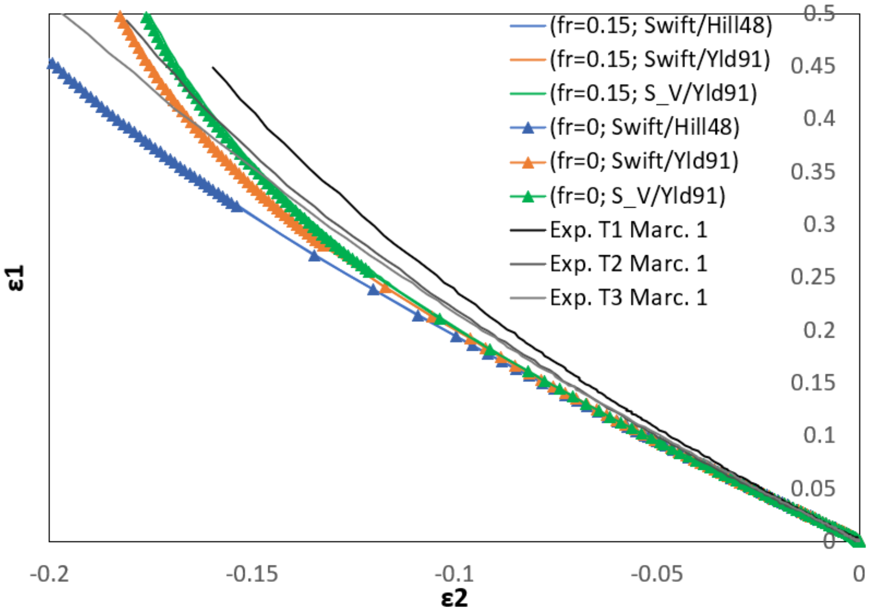

Figure 5.5. Evolution of the major strain-minor strain in the Marciniak test using the specimen with 1 inch width and the friction coefficient of 0.15 (fr=0.15) or null friction coefficient (fr=0) in the numerical predictions.

Figure 5.6 shows the influence of the friction coefficient on the predicted punch force evolution. The influence of the friction coefficient becomes apparent for a punch displacement higher that 6 mm. The maximum punch force is slightly higher in the simulations performed with the friction coefficient of 0.15. This increase of the punch force with the increase of the friction coefficient was already expected, due to the friction force arising in the contact surfaces. The maximum difference is about 5.3% in relation to results with a null friction coefficient. The increase of the friction coefficient does not affect the trend between the different constitutive models.

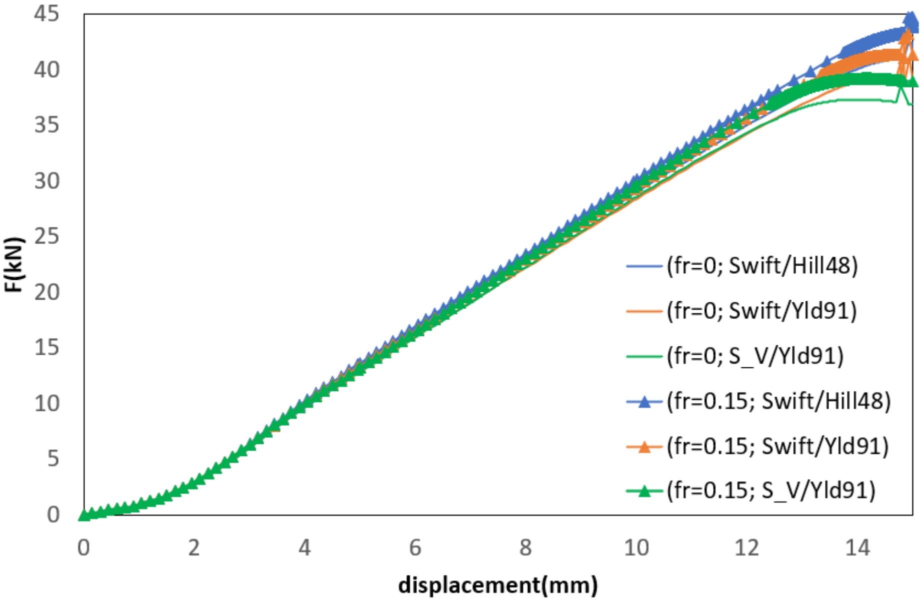

Figure 5.6. Evolution of the predicted punch force in the Marciniak test specimen with 1 inch width, for friction coefficient of 0.15 (fr=0.15) and null friction coefficient (fr=0), using the model without drawbeads.

Figure 5.7 presents the evolution of both stress triaxiality and Lode parameter in function of the punch displacement, evaluated in the center of the specimen. Before the onset of necking, all models have values close to the ones related with the uniaxial tension stress state, as previously observed in **Figure 5.3**. The evolution of the stress triaxiality and the Lode parameter is similar for all models, both under frictionless and friction situations, which is in agreement with the results shown in **Figure 5.5**. Although it is almost imperceptible, the plastic strain starts for lower values of punch displacement in the models with the higher friction coefficient, due to the additional frictional forces arising in the model. However, the impact in the strain path observed in the center of the specimen is negligible. Thus, although the models with the higher friction coefficient present higher values for the maximum force, the displacement for which the onset of necking occurs is not affected by the friction coefficient value.

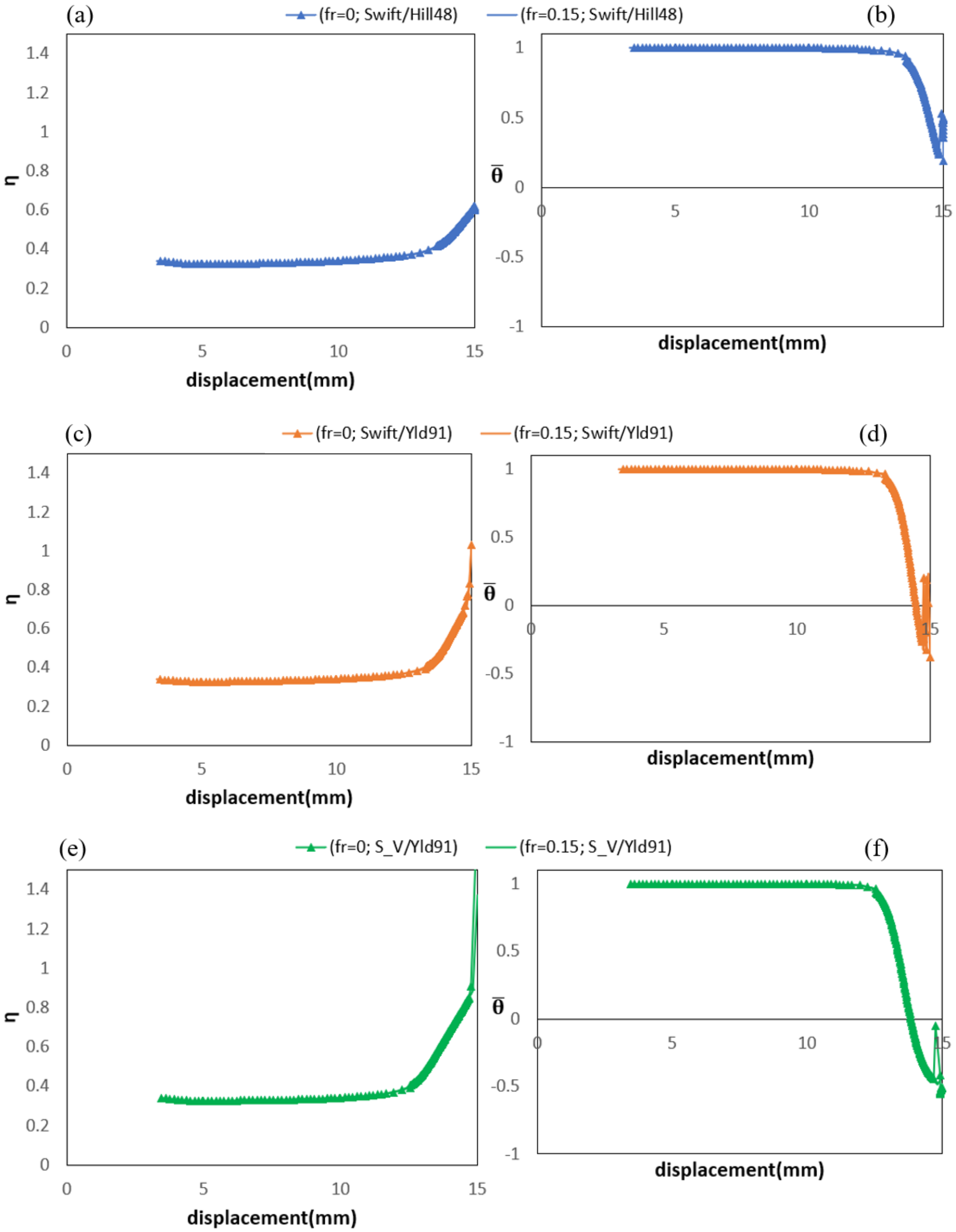

Figure 5.7. Evolution of triaxiality (a, c and e) and Lode parameter (b, d and f) with the punch displacement in the Marciniak test specimen with 1 inch width from simulations (without drawbeads) with friction coefficient of 0.15 (fr=0.15) and with null friction coefficient (fr=0).

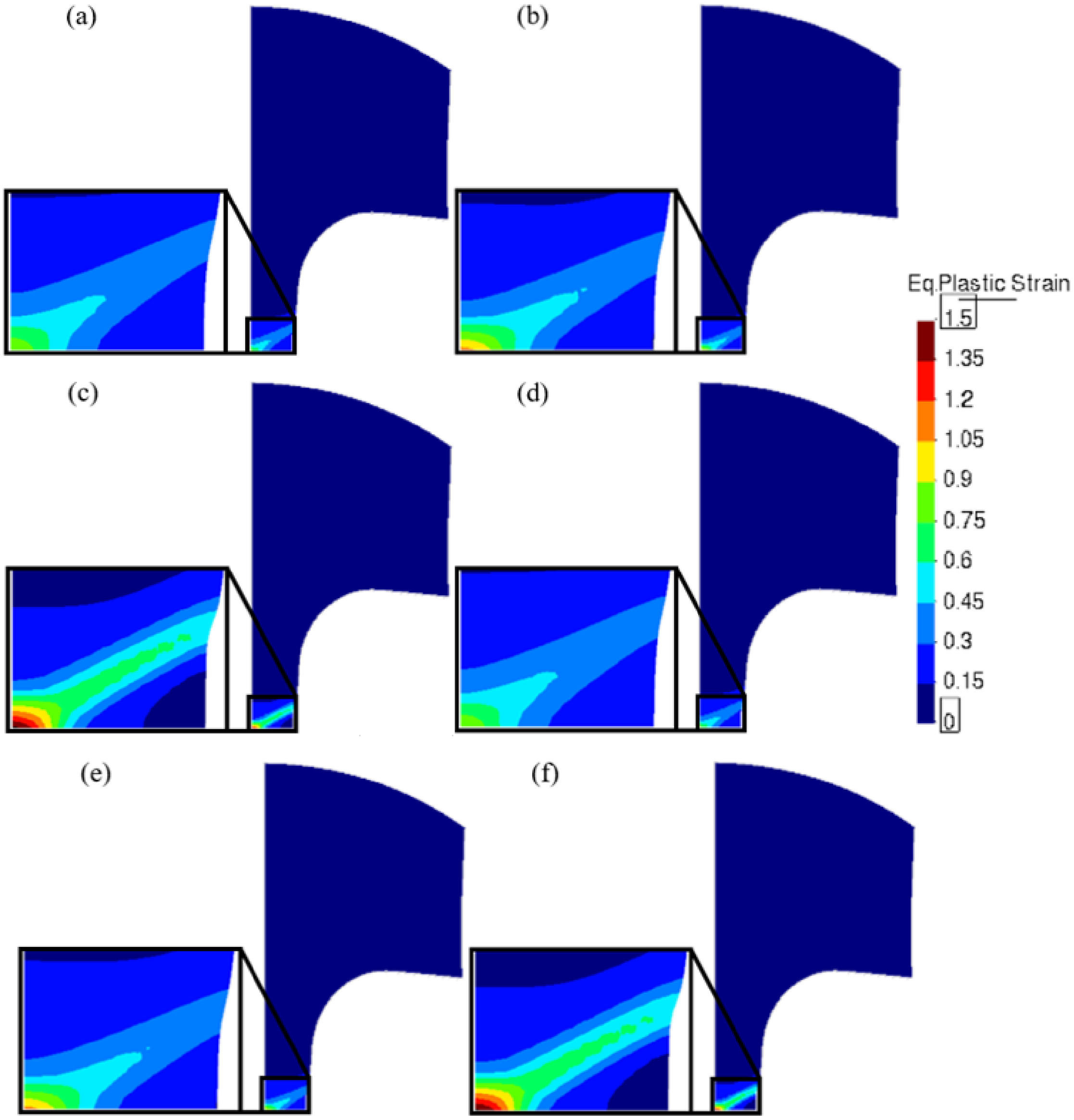

Figure 5.8. Equivalent plastic strain distribution in the Marciniak test specimen with 1 inch width: with friction coefficient of 0.15 (a) Swift/Hill48, (b) Swift/Yld91, (c) S_V/Yld91; with null friction coefficient (d) Swift/Hill48, (e) Swift/Yld91, (f) S_V/Yld91.

Figure 5.8 shows the distribution of the equivalent plastic strain in the specimens for 15 mm of punch displacement. The maximum value of equivalent plastic strain in the models with null friction coefficient is 0.90, 1.11 and 1.56, for Swift/Hill48, Swift/Yld91 and S_V/Yld91, respectively. Although the values of equivalent plastic strain are higher in models with 0.15 of friction coefficient, the difference is almost negligible.

Table 5.2 presents the computational times for each simulation. Although there was a reduction of the computational cost under frictionless conditions, the difference is lower than 8.5% for Swift/Hill48 and Swift/Yld91, being a little more significant for the model S_V/Yld91, with a difference of 10.9%. Since the strain paths predicted are almost overlapped in both models, this simplification (frictionless and without drawbeads) is adopted for all the other simulations performed in this work.

Table 5.2. Computational times of the Marciniak test specimen with 1 inch width using different values of friction coefficient.

	Fr=0.15		Fr=0	
Model	**Wall Time (s)**	**CPU Time (s)**	**Wall Time (s)**	**CPU Time (s)**
Swift/Hill48	311	1118	286	1059
Swift/Barlat91	748	1999	673	1830
Swift+Voce/Barlat91	1115	2807	1001	2499

The yield criteria were calibrated considering a Lankford coefficient from the uniaxial tensile test, performed at TD, of 1.1731 (as seen in the **Figure 3.5** (b)). As shown in **Figure 3.7** (a), both yield criteria lead to slightly lower values, of 1.1725 for Hill48 and 1.1719 for Yld91. In terms of the ratio between the in-plane strains, **Figure 3.7** (b) shows that $\varepsilon_{\mathrm{TD}}/\varepsilon_{\mathrm{RD}}$ is equal to -1.9061 for Hill48, while for Yld91 it is -1.8533. Note that $\varepsilon_{\mathrm{TD}} = \varepsilon_1$ and $\varepsilon_{\mathrm{RD}} = \varepsilon_2$ and that for an isotropic material $\varepsilon_1 = -2\varepsilon_2$. The analysis of **Figure 5.1** and **Figure 5.5** shows that the $\varepsilon_{\mathrm{TD}}/\varepsilon_{\mathrm{RD}}$ are closer to these values in the numerical models. However, the experimental results show higher negative values for the $\varepsilon_{\mathrm{TD}}/\varepsilon_{\mathrm{RD}}$, indicating that this geometry for the specimen does not reproduce exactly the same stress conditions as the uniaxial tensile test. Despite the dispersion observed in the experimental results (3 tests under identical conditions), the numerical predictions using the Barlat yield criterion leads to a strain path closer to the experimental one.

5.1.1.2. Specimen with 5.5 inch width

According with the experimental results, the increase of the specimen width from 1 inch to 5.5 inch leads to a change in the strain path from close to uniaxial tension to approximately plane strain. Therefore, this specimen configuration is used to assess the accuracy of the numerical model. In this context, it should be mentioned that both yield criteria were calibrated without using any information concerning plane strain conditions.

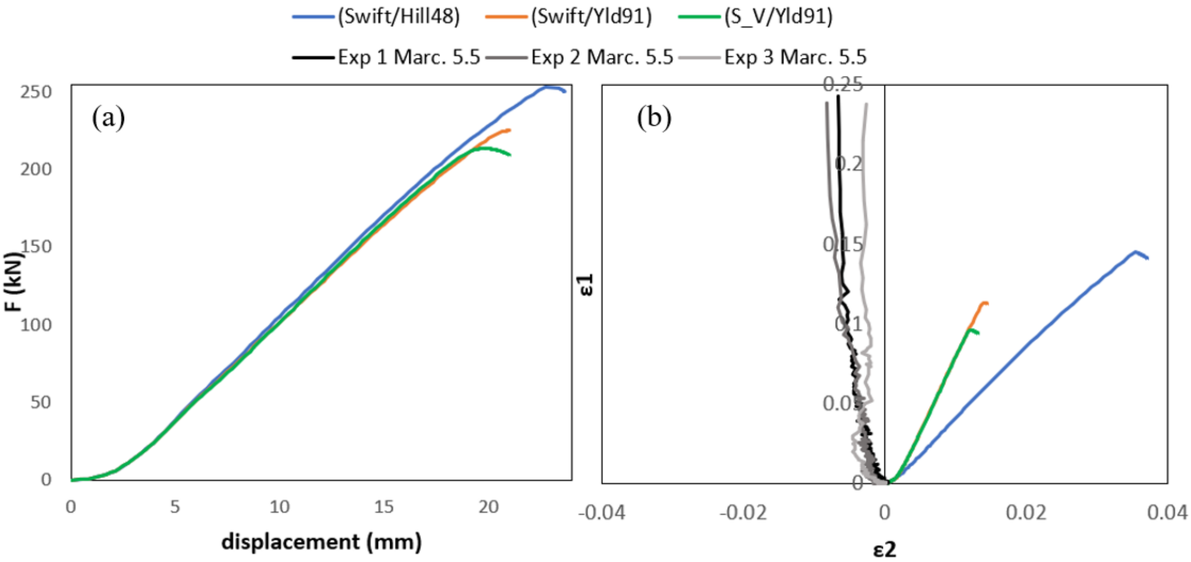

Figure 5.9. Evolution in the Marciniak test specimen with 5.5 inch width of the predicted: (a) punch force and (b) major versus minor strain, including the experimental results.

Figure 5.9 (a) shows the punch force evolution, comparing the three constitutive models previously described. The maximum punch force predicted by the constitutive models Swift/Hill48, Swift/Yld91 and S_V/Yld91 is 253.3, 225.4 and 213.8 kN, respectively. Besides, the displacements for which the maximum force is attained are different, namely 22.7, 21.0 and 19.89 mm, respectively. **Figure 5.9** (b) shows the comparison between numerical and experimental results of major strain-minor strain evolution. The predicted maximum values for the major strain were 0.14, 0.094 and 0.11, using the constitutive models Swift/Hill48, Swift/Yld91 and S_Voce/Yld91, respectively. However, the minor strains also present clearly positive values, while the experimental results show slightly negative ones. The ratio between the major and minor strain ($\varepsilon_{\mathrm{TD}}/\varepsilon_{\mathrm{RD}}$) were of 4.36 for Swift/48 and 8.53 for the Swift/Yld91 and S_V/YLd91 models. These ratio values are compatible with those predicted analytically in **Figure 3.7** (b), which show that there are big differences between the two yield criteria for loading directions close to plane strain.

Figure 5.10 shows the distribution of the equivalent plastic strain in the specimen with 5.5 inch width. The maximum values of equivalent plastic strain for 21 mm of punch displacement are 0.33, 0.44 and 0.71 for the model's combinations Swift/Hill48, Swift/Yld91 and S_V/Yld91, respectively. Nevertheless, it is important to mention that the strain localization occurs on the outer edge of the punch, as shown in **Figure 5.10** (d), whatever the constitutive model adopted. As in the simulation with the 1 inch specimen, the

S_V/Yld91 model was the first to localize, followed by SwiftYld91 and finally the Swift/Hill48. This trend is similar because the strain localization occurs associated to a tensile stress state induced by the punch shoulder radius. This also explains why the specimen center stops deforming, as shown in **Figure 5.9** (b). Thus, for this stress path no strain localization in the specimen center is predicted, without taking into account any damage model.

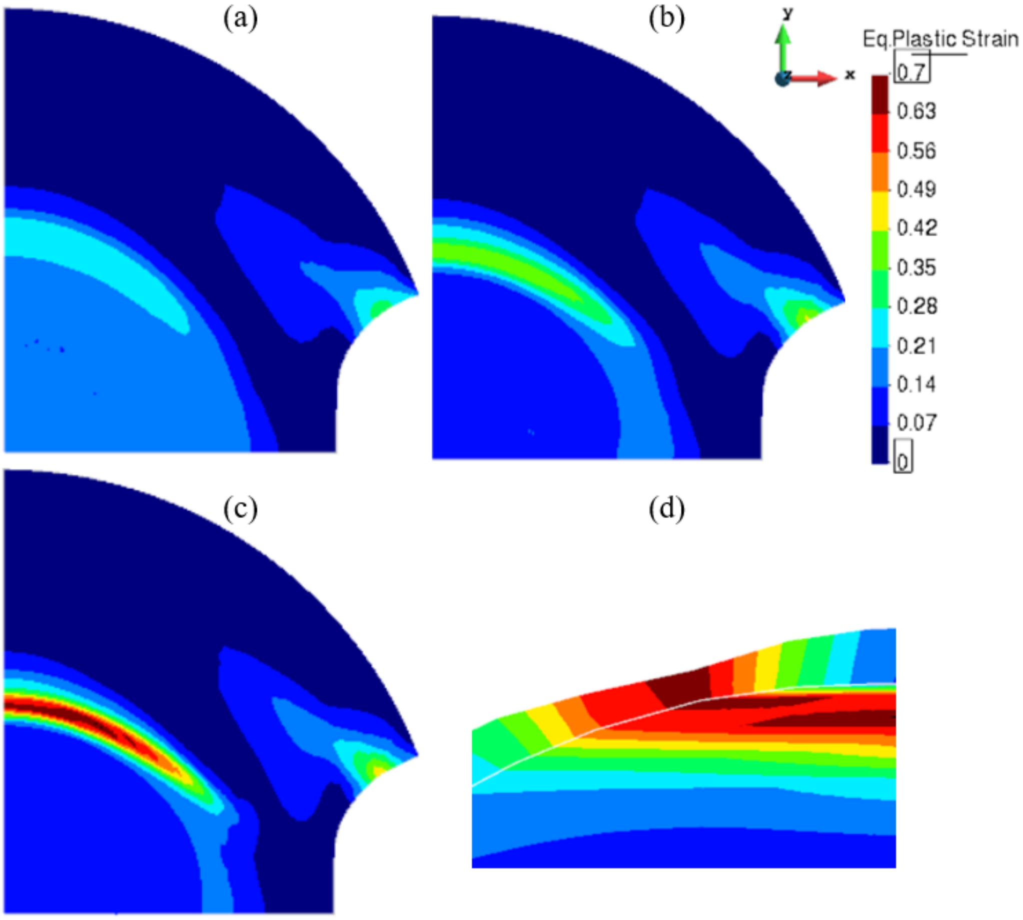

Figure 5.10. Equivalent plastic strain on the specimen with 5.5 inch width predicted by the models: (a) Swift/Hill48, (b) Swift/Yld91, (c) S_V/ Yld91; (d) Strain localization in the location corresponding to the outer edge of the punch shoulder radius.

The evolution of the stress triaxiality in the specimen is presented in **Figure 5.11** (a), comparing the three different constitutive models. The mean values of stress triaxiality are close 0.61 for all models, which is higher than to the reference value of 0.577 ($\sqrt{3}/3$) for plane strain, as presented in the **Table A.1**. **Figure 5.11** (b) shows the evolution of the Lode parameter. The average value for Lode parameter was -0.33 for all constitutive models, which is quite different from 0.0, which is the reference value for plane strain (see **Table A.1**). This confirms that both yield criteria do not enable to reproduce the stress state of the plane strain using the 5.5 inch specimen. According to **Figure 5.9** (b) the stress state is between plane strain and equibiaxial tension. It is also worth mentioning that since the strain localization occurs in the punch shoulder radius, the center of the specimens stops to deform, for punch displacements of 22.6, 20.63 and 19.2 mm, for the Swift/Hill48, Swift/Yld91 and S_V/Yld91 models, respectively. This explains the changes of the trend observed in **Figure 5.11** as well as in **Figure 5.9** (b), since there is some elastic recovery after the necking around the punch shoulder radius.

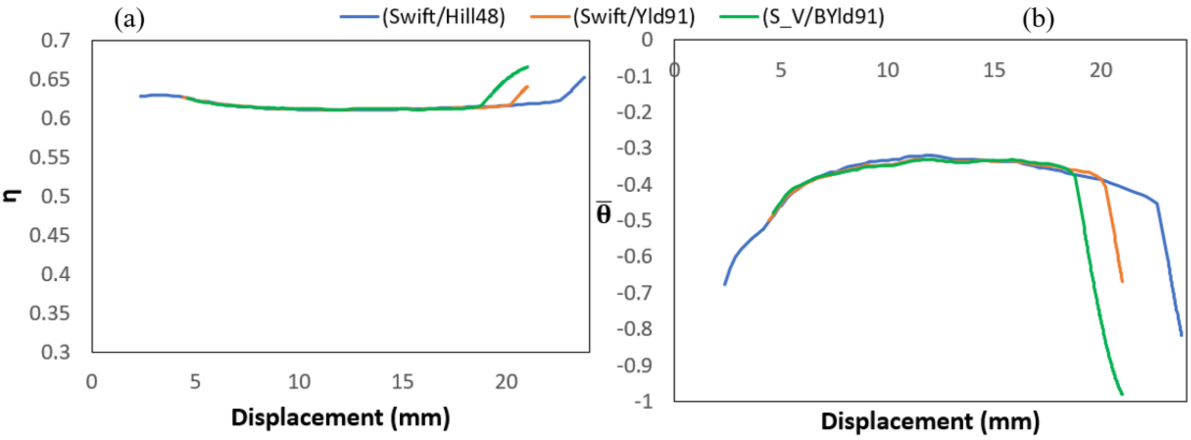

Figure 5.11. Evolution of triaxiality (a) and Lode parameter (b) with the punch displacement in the Marciniak test specimen with 5.5 inch width comparing different constitutive models.

5.1.1.3. Specimen with 6.5 inch width

The main objective of using the specimen with a width of 6.5 inch in the experimental procedure is to obtain a strain path between plane strain and equibiaxial. **Figure 5.12** (a) presents the comparison between numerical and experimental evolutions of the major strain- minor strain. The maximum values for the major strain were 0.22, 0.12 and 0.11, for the Swift/Hill48, Swift/Yld91 and S_V/Yld91 constitutive models, respectively. The ratio between the major and minor strain were of 1.31 for Swift/Hill48 and 1.85 for both the Swift/Yld91 and S_V/Yld91 models. These values are considerably lower than the experimental ones. Moreover, they are considerably lower than the ones obtained with the 5.5 inch specimen, which confirms the ability of the numerical models to predict the strain path change associated with the specimen width. However, both yield criteria do not allow a proper estimate of the linear strain path for both specimens.

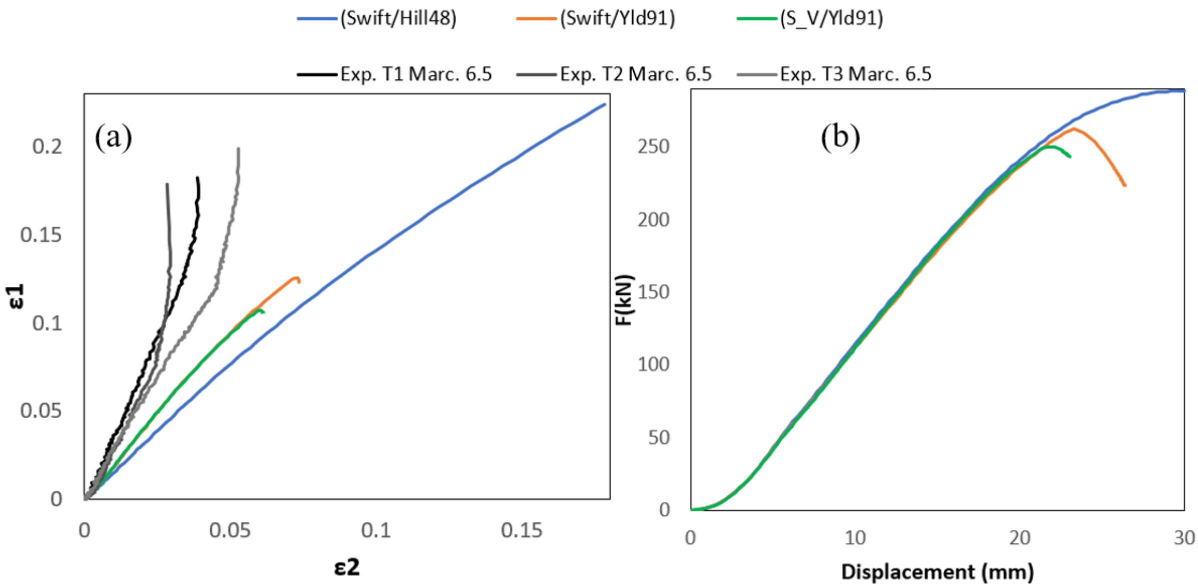

Figure 5.12. Evolution in the Marciniak test specimen with 6.5 inch width of the predicted: (a) major versus minor strain, including the experimental results and (b) punch force.

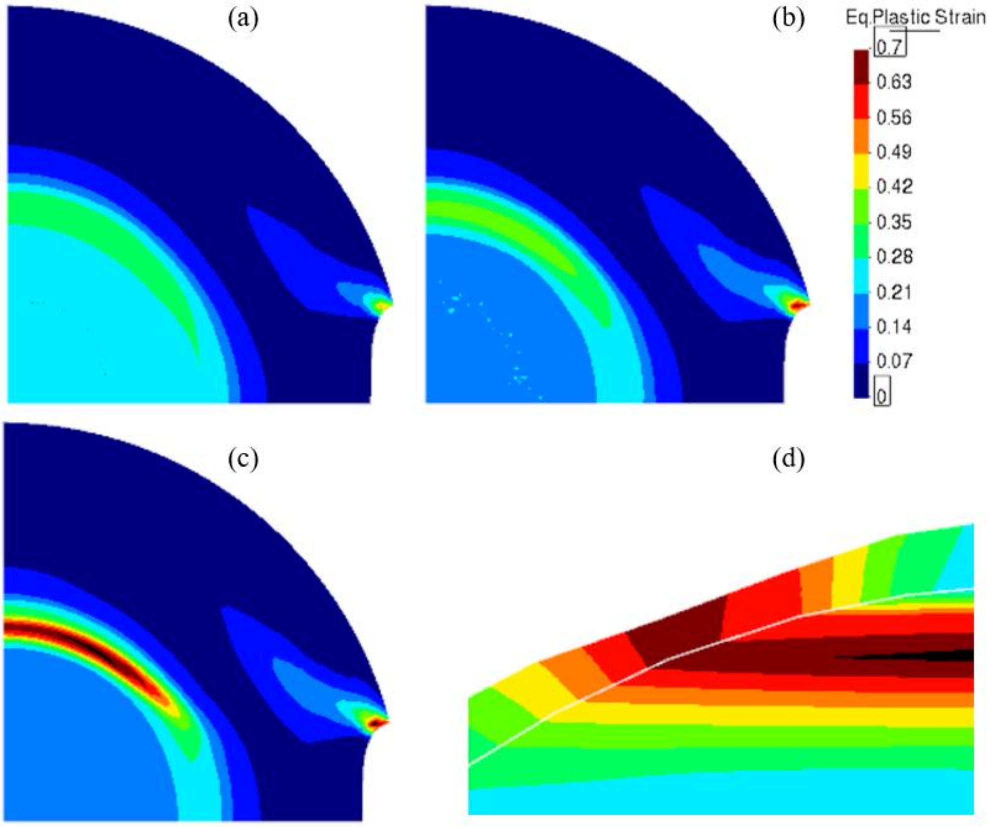

Figure 5.13. Equivalent plastic strain on the specimen with 6.5-inch width predicted by the models: (a) Swift/Hill48, (b) Swift/Yld91, (c) S_V/Yld91; (d) Strain localization in the location corresponding to the outer edge of the punch shoulder radius.

Figure 5.12 (b) shows the punch force evolution. The predicted maximum punch force values were 288.57, 262.4 and 250.19 kN, for displacements of 29.8, 23.3 and 21.61

mm, for Swift/Hill48, Swift/Yld91 and S_Voce/Yld91 constitutive models, respectively. Such as for the specimen with a width of 5.5 inch, the decrease of the force occurs associated with the strain localization on the outer edge of the punch shoulder radius, as highlighted in the **Figure 5.13** (d). **Figure 5.13** shows the distribution of the equivalent plastic strain in the specimen, comparing the three constitutive models. The maximum equivalent plastic strain, evaluated for 23 mm of punch displacement is 0.50, 0.68 and 0.75 for the Swift/Hill48, Swift/Yld91 and S_V/Yld91, respectively. The analysis of the evolution of the Lode parameter and the stress triaxiality for this test confirms that also this specimen leads to a stress state between plane strain an equibiaxial tension, but closer to the equibiaxial tension.

5.1.1.4. Specimen with 8 inch width (equibiaxial)

The last specimen used to perform the Marciniak test presents 8 inch width, which provides an equibiaxial stress state. **Figure 5.14** (a) presents the comparison between numerical and experimental evolutions of the major and minor strains. Using the Swift/Hill48, Swift/Yld91 and S_V/Yld91 models, the maximum values for the major strain were 0.19, 0.13 and 0.11, respectively. The ratio between major and minor strains was 1.02 for all the constitutive models. According with the analytical results shown in **Figure 3.7** (b), the $\varepsilon_{\mathrm{TD}}/\varepsilon_{\mathrm{RD}}$ ratio for a loading direction of 45° is 0.7585 and 0.7589, for the Hill48 and the Yld91 criteria. Thus, the ratio between major and minor strain should be the inverse, i.e. 1.3184 and 1.3176. The value reported in the experimental results is 1.16. Thus, the numerical model leads to a smaller ratio, which can be related to the fact that the stress state is not exactly equibiaxial, due to the constrains imposed by the tools geometry. This result seems to be corroborated by the fact that the strain path is identical for both yield criteria. The maximum values of strains attained in each test are different as a consequence of the occurrence of strain localization, once again in the punch shoulder radius. The strain localization occurs for different values of punch displacement, as shown in **Figure 5.14** (b). Considering the Swift/48, Swift/Yld91 and S_V/Yld91 models, the maximum values for the punch force were 283.13, 268.72 and 259.1 kN, respectively, which occurs for 28.8, 24.9 and 23.1 mm of punch displacement. **Figure 5.15** shows the distribution of the equivalent plastic strain in the specimen. For a punch displacement of 28 mm, the maximum equivalent plastic strain is 0.48, 1.06 and 1.20 using the Swift/Hill48, Swift/Yld91 and S_Voce/Yld91 models, respectively. As for the other specimens submitted to expansion, the strain localization occurs in the punch shoulder radius, as shown in **Figure 5.15** (d).

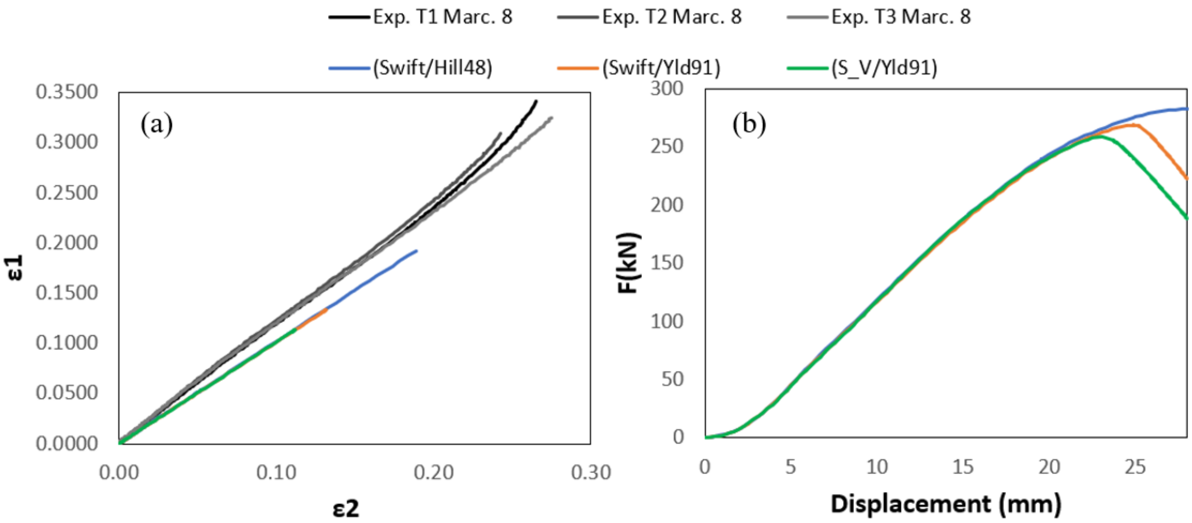

Figure 5.14. Evolution in the Marciniak test specimen with 8 inch width of the predicted: (a) major versus minor strain, including the experimental results and (b) punch force.

The evolution of the predicted stress triaxiality in the specimen is presented in **Figure 5.16** (a) for the three constitutive models. The predicted value for the stress triaxiality was 0.66 for all models. **Figure 5.16** (b) shows the evolution of the Lode Parameter, highlighting a mean value of -0.99 for all models. The reference values for stress triaxiality and Lode parameter for the equibiaxial stress state (see **Table A.1)** are 0.66 (2/3) and -1.0, which are both very close to the average numerical values. Thus, the circular specimen enables to reproduce a stress state close to the equibiaxial. Nevertheless, the strain path is closer to equibiaxial strain (see also **Figure 3.7** (b)). For this specimen, the effect of the unloading of the center, once the strain localization occurs in the punch radius, is not so evident in the stress triaxiality and the Lode parameter. In fact, only for the Swift/Yld91 and S_V/Yld91 models, it is possible to observe the unloading, which occurs for 25.2 and 23.1 mm of punch displacement. Moreover, as for the other cases, it is not possible to predict the fracture in the center, as normally reported in the literature [22], [42], without taking into account a damage model. Note that all simulations were performed with similar element sizes in the critical regions and curvature regions of the Marciniak tools. Thus, the blank discretization is not limiting the analysis, since it was possible to reproduce the strain localization in the specimen center for the 1 inch Marciniak specimen.

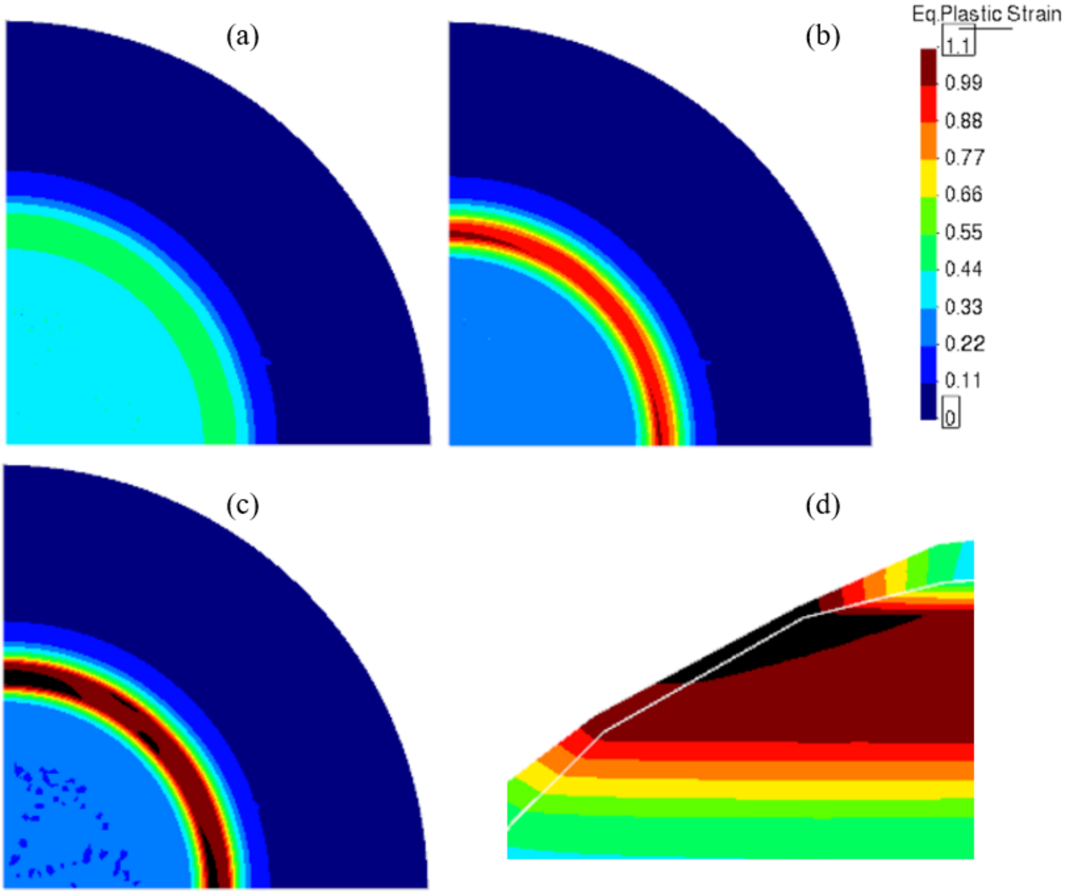

Figure 5.15. Equivalent plastic strain on the specimen with 8-inch width predicted by the models: (a) Swift/Hill48, (b) Swift/Barlat91, (c) Swift+Voce/Barlat91; (d) Necking effect in the location corresponding to the outer edge of the punch.

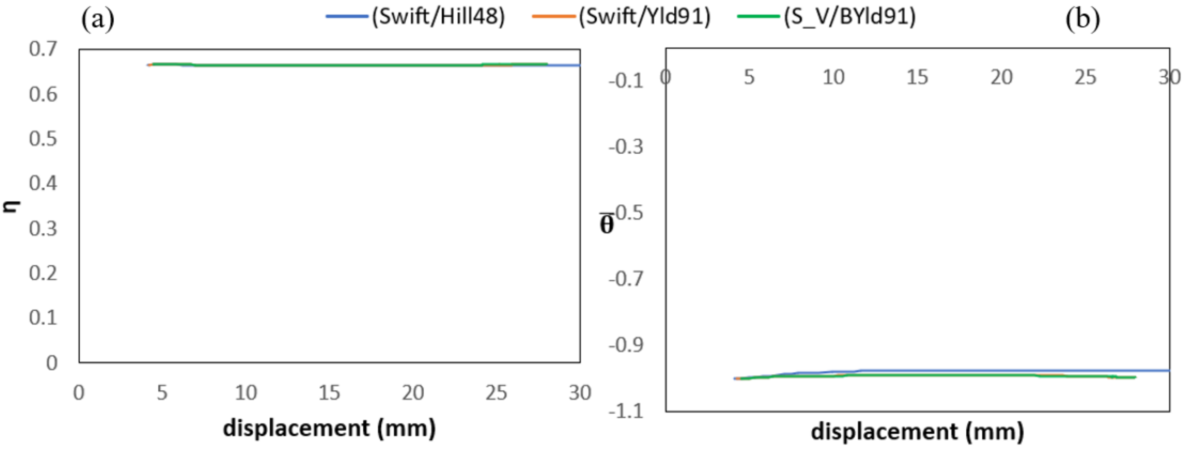

Figure 5.16. Evolution of triaxiality (a) and Lode parameter (b) with the punch displacement in the Marciniak test specimen with 8 inch width comparing different constitutive models.

5.1.2. Nakazima tests

The simulations with the Nakazima tool set have the same objective as the Marciniak tests with the 8 inch specimen, i.e. both are representative of the equibiaxial stress state. As previously mentioned, simulations were performed with the punch radius of 50.8 mm and 5 mm. The smaller punch dimension makes it easier to perform tests with a specimen submitted to a pre-strain. In this section, both Nakazima tests are performed without any pre-strain to evaluate if the reduction of the punch size induces any changes in the stress and strain paths.

5.1.2.1. Punch with 50.8 mm radius

Figure 5.17 (a) shows the comparison between numerical and experimental evolution of the major and minor strains, during the Nakazima test using the punch with 50.8 mm of radius. Using the constitutive models Swift/Hill48, Swift/Yld91 and S_V/Yld91, the maximum values of major strain were 0.42, 0.51 and 0.55, respectively. The ratio between the major and minor strain were identical (1.04) for all constitutive models. In fact, the evolution of the major strain-minor strain curve is similar to the one reported for the Marciniak test (see **Figure 5.14** (a)), with their overlapping until the end of the simulation. However, when comparing the experimental with the numerical strain paths, they are now closer, at least in the initial part. Nevertheless, the experimental results show an evolution of the strain path, which tends to the plane strain condition, which is not observed in the numerical results.

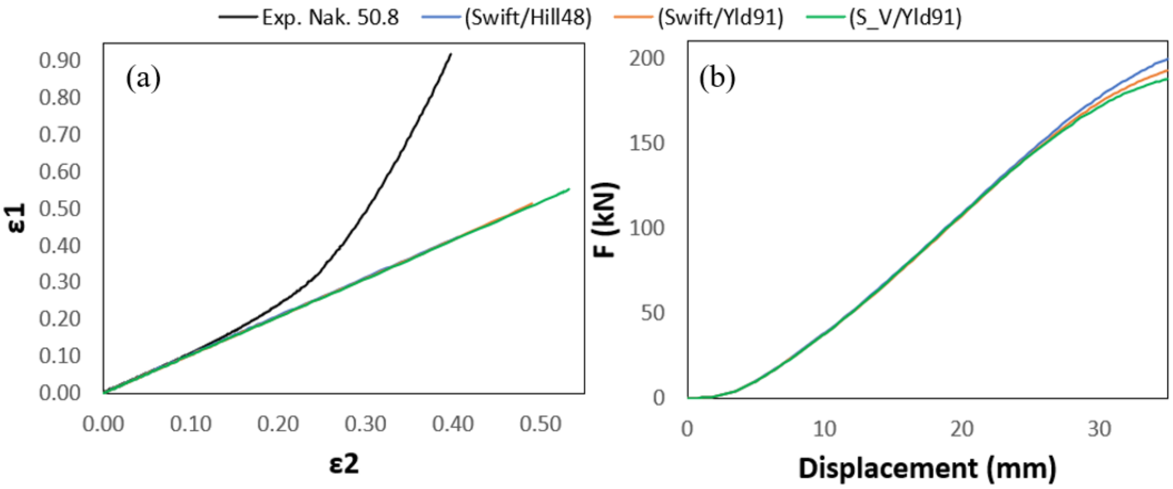

Figure 5.17. Evolution in the Nakazima test specimen (with 50.8 mm punch) of the predicted: (a) major versus minor strain, including the experimental results and (b) punch force.

Figure 5.17 (b) shows the punch force evolution predicted by each constitutive model. In this case, all simulations were performed until the same punch displacement, without the occurrence of a clear drop in the punch force.

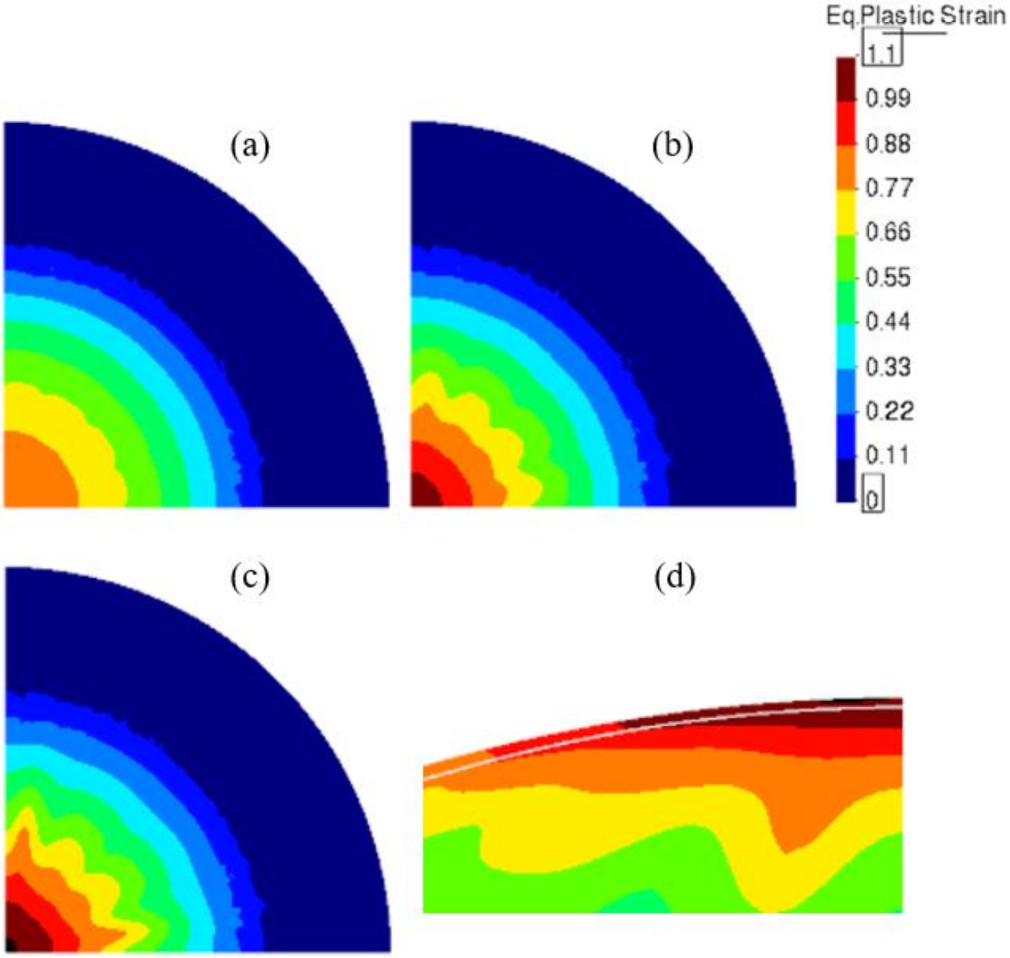

Figure 5.18. Equivalent plastic strain in the Nakazima test specimen using 50.8 mm punch predicted by the models: (a) Swift/Hill48, (b) Swift/Yld91, (c) S_V/Yld91; (d) Strain distribution in the center of the specimen, as predicted with the S_V/Yld91 model.

Figure 5.18 shows the distribution of the equivalent plastic strain in the specimen, predicted by the three different constitutive models. The specimen presents a clear thinning in its center, as shown in **Figure 5.18** (d), which is responsible for the reduction in the increase of the punch force. However, the thickness reduction is quite uniform around the center, presenting a clear localization. This explains why the strain path remains unaltered, although high values of thinning have already been attained. This suggests that in order to predict the strain localization it is necessary to include softening effects, related with damage evolution. For 35 mm of punch displacement, the maximum equivalent plastic strain is 0.85, 1.02 and 1.10 using the Swift/Hill48, Swift/Yld91 and S_V/Yld91 models, respectively. As shown in **Figure 4.4**, the blank discretization adopted in the specimen center is regular. It is interesting to note that for the Hill48 criterion, the distribution of the equivalent plastic strain is quite axisymmetric. However, the Yld91 leads to a more irregular distribution of the equivalent plastic strain. This more irregular distribution does not seem to result from mesh size effects, since the elements used in this region were very small. In fact, the element size is similar to the one used in the simulations of the Marciniak tests, which did not show this effect. Moreover, the contact forces are well distributed, showing no visible peaks.

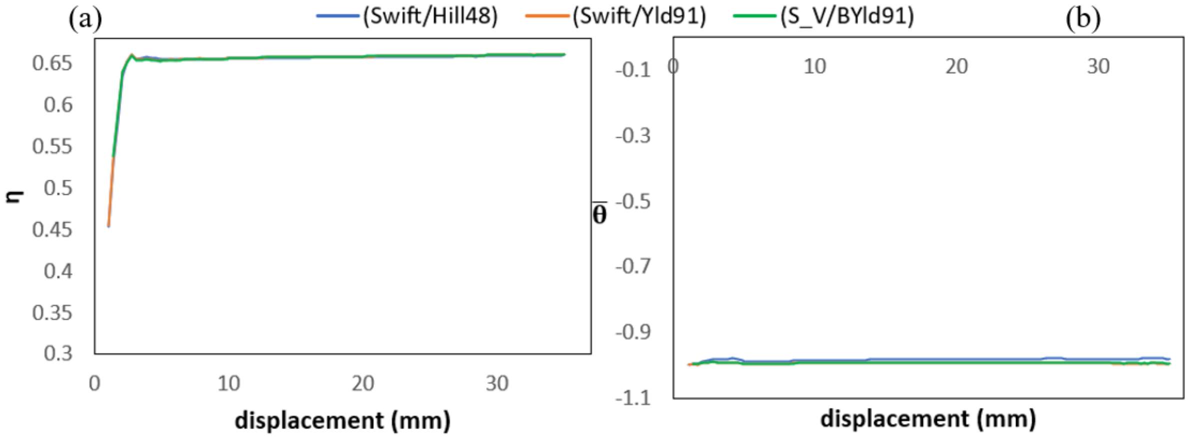

Figure 5.19. Evolution of triaxiality (a) and Lode parameter (b) with the punch displacement in the Nakazima test specimen with 50.8 mm punch.

Figure 5.19 (a) presents the evolution of the predicted stress triaxiality, which presents a mean value of about 0.65 for all constitutive models. **Figure 5.19** (b) shows the evolution of the predicted Lode parameter, which presents a value of -0.99 for all constitutive models. Both are very close to the ones reported for the Marciniak test (see **Figure 5.16)** and in **Table A.1**, for the equibiaxial stress state.

5.1.2.2. Punch with 5 mm radius

Figure 5.20 (a) shows the numerical and experimental results of major strain-minor strain evolutions in the Nakazima test, performed with the 5.0 mm punch radius. Using the Swift/Hill48, Swift/Yld91 and S_V/Yld91 models, the maximum major strain values were 0.6, 0.64 and 0.66, respectively. The ratio between major and minor strain is approximately 1.05 in all models, which is in good agreement with the experimental results, and very close to those found in the previous equibiaxial tests. **Figure 5.20** (b) shows the predicted punch force evolution. The maximum punch force predicted by the constitutive models Swift/Hill48, Swift/Yld91 and S_V/Yld91 was 18.16, 17.72 and 17.19 kN, respectively, for a punch displacement of approximately 11.5 mm.

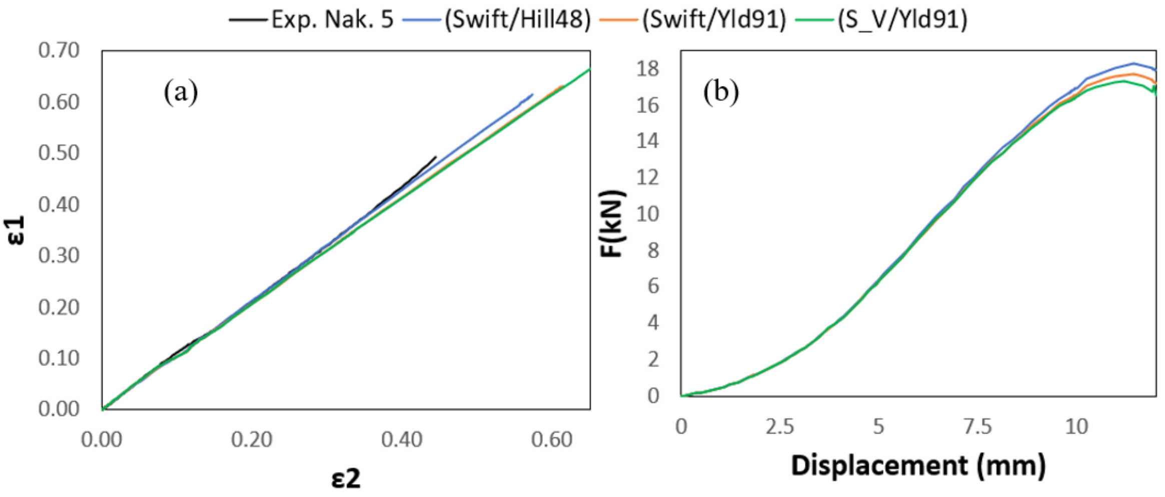

Figure 5.20. Evolution in the Nakazima test specimen (with 5 mm punch) of the predicted: (a) major versus minor strain, including the experimental results and (b) punch force.

Figure 5.21 shows the predicted distribution of the equivalent plastic strain in the specimen. For 12 mm of punch displacement, the maximum value is 1.28, 1.34 and 1.44 for the model’s Swift/Hill48, Swift/Yld91 and S_V/Yld91, respectively. The thinning of the center of the specimen (see **Figure 5.21** (d)) is clearly visible, as in the Nakazima test with the 50.8 mm punch.

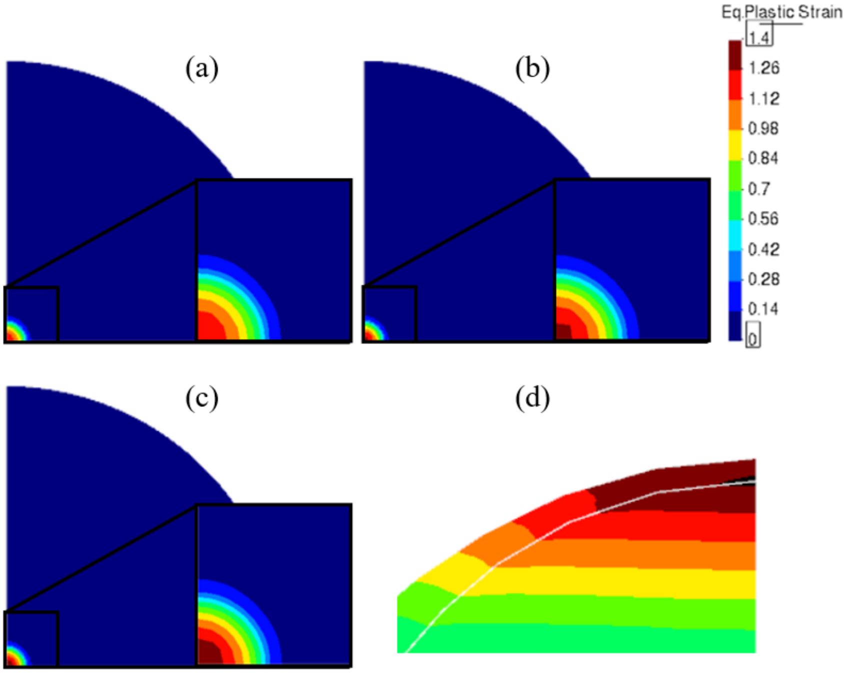

Figure 5.21. Equivalent plastic strain in the Nakazima test specimen using 5 mm punch predicted by the models: (a) Swift/Hill48, (b) Swift/Yld91, (c) S_V/ Yld91; (d) Strain distribution in the center of the specimen, as predicted with the S_V/Yld91 model.

Figure 5.22 (a) presents the predicted evolution for the stress triaxiality, which ranges between 0.55 and 0.65 for all the constitutive models. **Figure 5.22** (b) shows the evolution of the predicted Lode parameter, which is approximately -0.99 for all the constitutive models. In this case, although both values remain close to the reference ones for the equibiaxial stress state (see **Table A.1)**, there are more oscillations, particularly in the stress triaxiality. This may be related to the element size being not ideal for such a small punch.

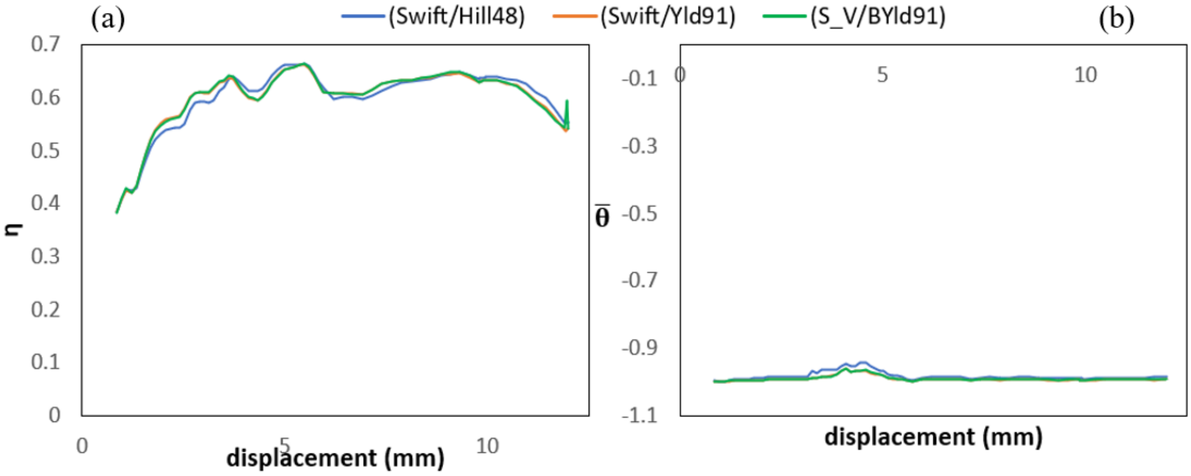

Figure 5.22. Evolution of triaxiality (a) and Lode parameter (b) with the punch displacement in the Nakazima test specimen with 5 mm punch.

5.1.3. Comparisons of monotonic strain path results and discussion

The shape of the specimen used in the Marciniak tests allows to obtain monotonic strain paths ranging from uniaxial stress (1 inch width) to equibiaxial strain (8-inch width). Globally, the numerical perditions are in good agreement with the experimental results, particularly under uniaxial tension and equibiaxial stress. In fact, for these strain paths the influence of the yield criterion seems negligible. On the other hand, for the specimen with 5.5 inch of width, for which the experimental results lead to an approximately plane strain path, the differences are significant. First, both yield criteria lead to a strain path between plane strain and equibiaxial stress. Moreover, the yield criteria lead to different strain paths.

According to **Figure 3.7**, both yield criteria predict a plane strain path for a similar loading direction. However, for loading directions slightly deviated, the in-plane strain ratio predicted by both yield criteria is quite different. In this context, it is important to mention that the yield criteria were calibrated using uniaxial tensile and bulge test results. Thus, no data concerning the plane strain state was used, which seems to have a direct impact in the model's prediction accuracy. This can also have an influence of the results for other tests, for which the experimental strain paths show an evolution towards the plane strain, after the onset of necking, as seen in the work of Ha et al [43]. The only example for which this behavior was predicted was the 1 inch Marciniak specimen.

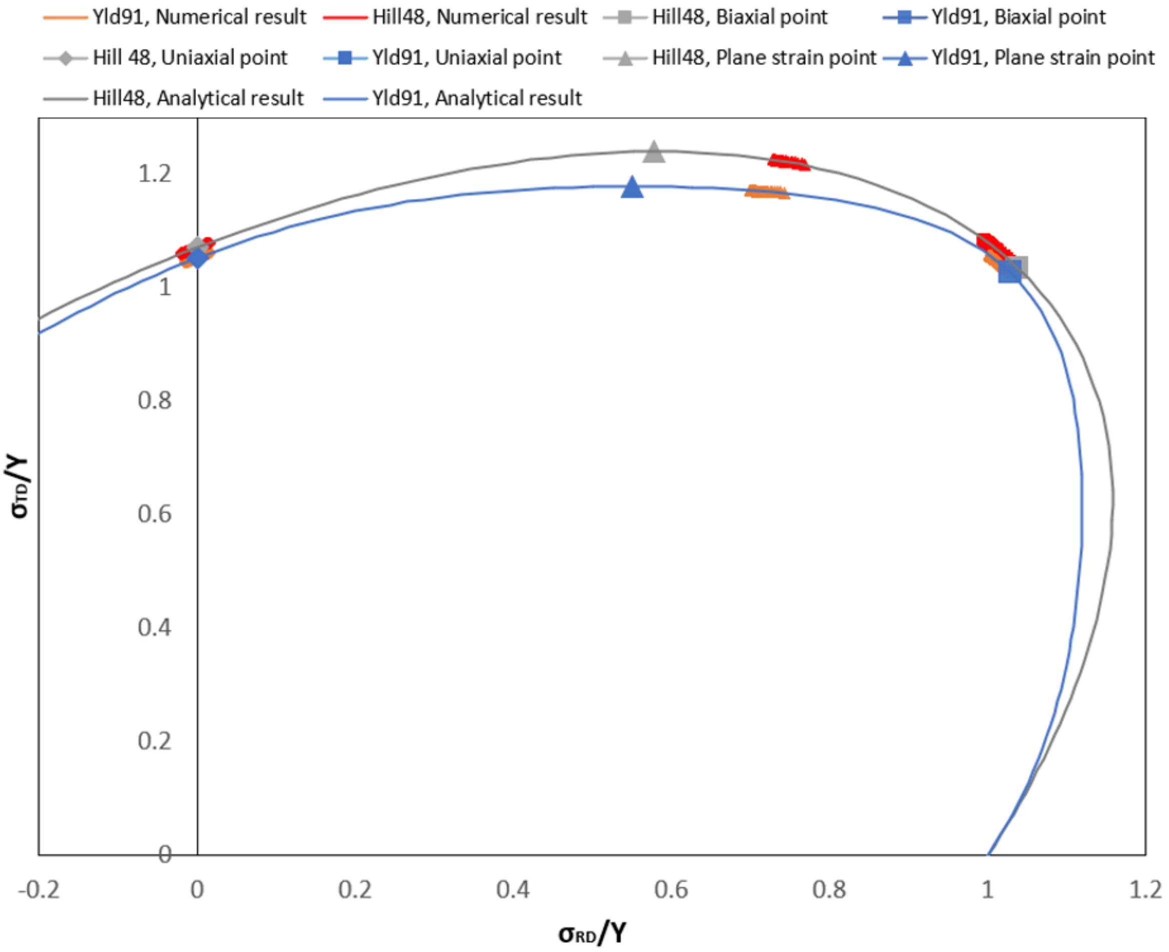

Figure 5.23. Normalized stresses in the transverse and rolling directions from analytical predictions and numerical solutions from Marciniak tests. Diamond marker: Uniaxial stress; Triangle marker: Plane strain (5.5 inch specimen); Square marker: Equibiaxial stress.

Globally, the results show that the hardening law influences the onset of necking while the yield criterion has a strong impact in the strain path predicted. **Figure 5.23** shows the normalized stresses, obtained from the Marciniak test using different configurations of the specimen, plotted in the transverse and rolling directions. The reference stress states are also marked on the analytical surfaces. The numerical results show the slight evolution of the loading direction, during the test. Moreover, this figure highlights that for a specimen with 5.5 inch, there is a relevant difference between analytical and numerical results, justifying the differences observed in **Figure 5.9** (b).

Regarding the equibiaxial stress state, the experimental strain paths are quite linear, except for the Nakazima with a 50.8 mm punch radius, which show the tendency to change to a plane strain state. Nevertheless, in the linear part they present a ratio closer to equibiaxial strain. The same trend is observed in the numerical results, which is explained by the slight deviation from the equibiaxial stress state, shown in **Figure 5.23**. This is enough to change the strain ratio to a value closer to 1.0, as shown in **Figure 3.7** (b). Thus, despite the material's anisotropy, all equibiaxial tests had $\varepsilon_{\mathrm{TD}}/\varepsilon_{\mathrm{RD}}$ values close to 1, i.e. the material tries to reach a balance between equibiaxial stress state and equibiaxial strain state, due to the geometrical constraints. This fact was also reported for the Hydraulic Bulge tests in the work of Reis et al. [44].

5.2. Nonlinear strain paths

Two different combinations of bilinear strain paths were performed, namely uniaxial tension followed by mini-Nakazima (punch with 5 mm radius) and Marciniak test followed by the mini-Nakazima. Two different values of specimen width were adopted in the Marciniak test, to obtain two different strain paths for the first loading stage.

5.2.1. Uniaxial followed by Mini-Nakazima (equibiaxial)

Figure 5.24 presents the comparison between the predicted bilinear strain paths for the three models, as well as the experimental results. The imposed uniaxial tension yields 6% of major pre-strain. The elastic recovery of the metallic sheet between the first and second loading phases is not visible in the experimental data. This creates a small divergence of results at the beginning of the second phase. However, it is possible to see that the strain paths are approximately parallel. In fact, the ratio between the major and minor strain in the experimental results is 1.027 and in the numerical is 1.019.

Figure 5.25 shows the punch force evolution in each stage of the bilinear strain path. The uniaxial tensile force shows a similar trend for the three models, corroborating the calibration results of section **3.1.3**. As shown in **Figure 5.25** (b), the punch force evolution attains the maximum value for a punch displacement of approximately 8.2 mm, which is smaller than the one observed for the monotonic equibiaxial strain path (see **Figure 5.20** (b)). This corroborates the influence of the pre-strain in the strains distribution. The trend between the models remains similar with the S_V/Yld91 model reaching the strain localization earlier, as highlighted in the **Figure 5.25** (b).

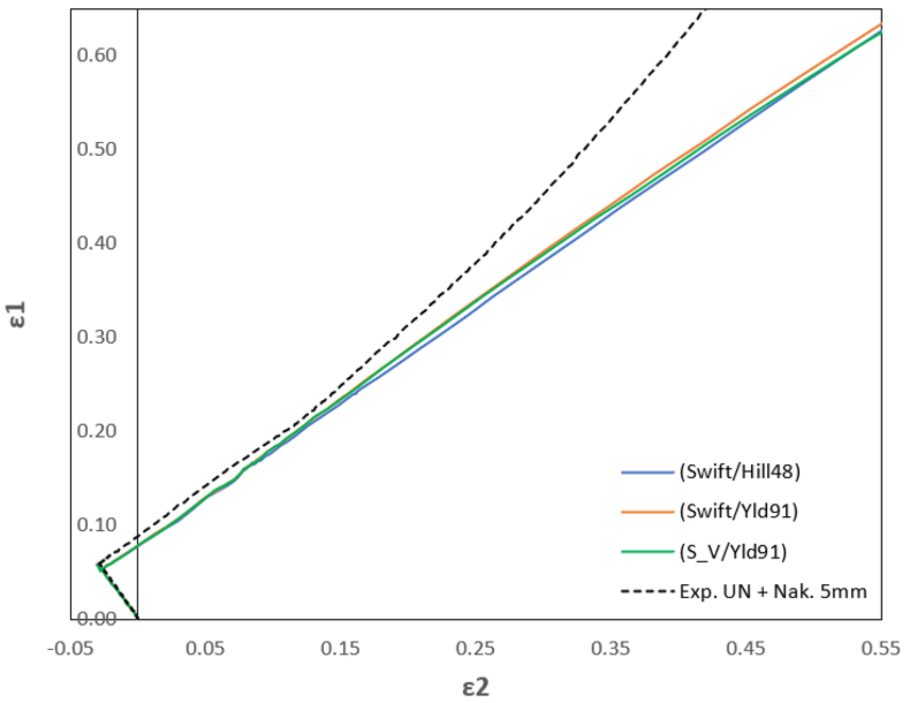

Figure 5.24. Major strain-minor strain evolution comparison between experimental and numerical results of the nonlinear test (Uniaxial tension + mini-Nakazima).

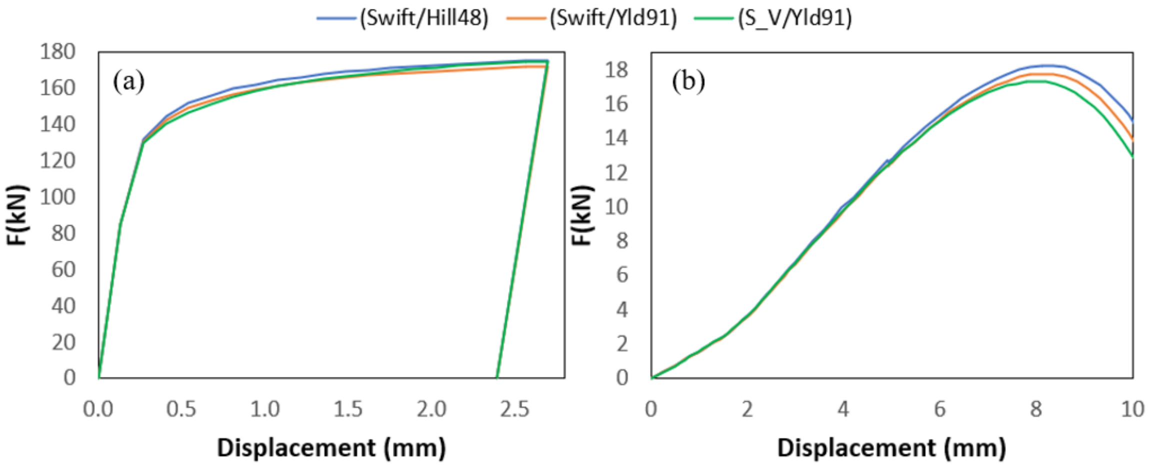

Figure 5.25. Evolution of the predicted force applied to the specimen in the nonlinear test (Uniaxial tension + mini-Nakazima): (a) First phase; (b) Second phase.

Figure 5.26 shows the distribution of the equivalent plastic strain in the specimen after the second strain path. For 10 mm of punch displacement, the maximum equivalent plastic strain predicted by the model's combinations Swift/Hill48, Swift/Yld91 and S_V/Yld91 provide is 2.02, 2.25 and 2.40, respectively. Since the second step uses the 5 mm Nakazima punch, the strain localization occurs in the center of the specimen, as highlighted in **Figure 5.26** (d). It should be mentioned that the thickness reduction is less uniform than the one observed in **Figure 5.21** (d), since a higher equivalent plastic strain was attained, due to pre-strain applied in the first phase.

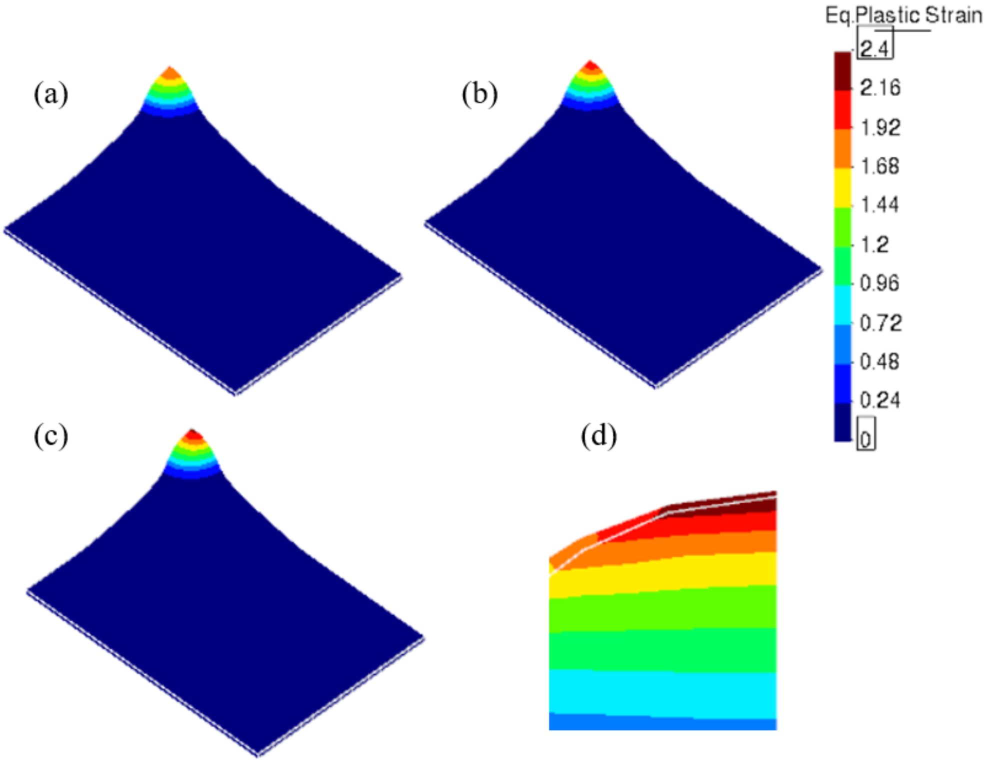

Figure 5.26. Equivalent plastic strain in the specimen of the nonlinear test (Uniaxial tension + mini-Nakazima): (a) Swift/Hill48, (b) Swift/Yld91, (c) S_V/Yld91; (d) Strain distribution in the center of the specimen, as predicted with the S_V/Yld91 model.

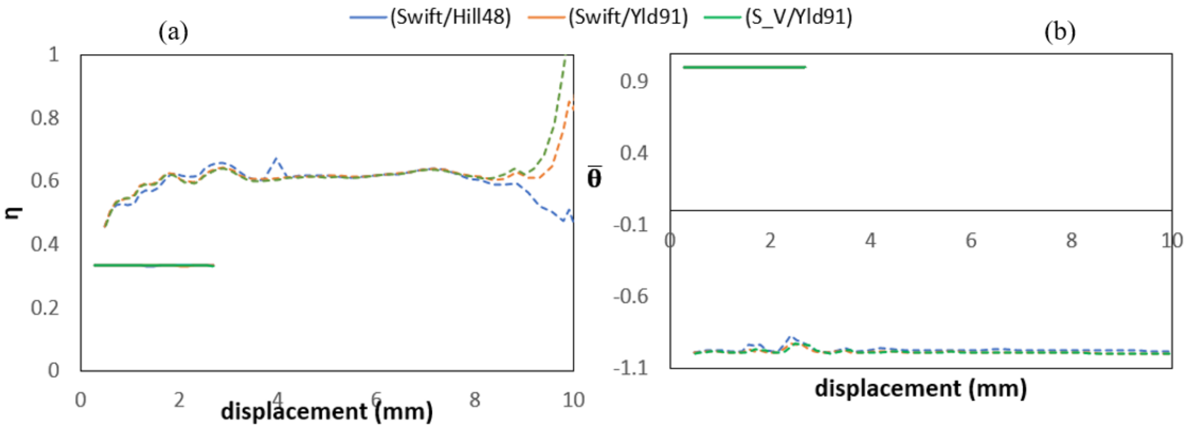

Figure 5.27. Evolution of triaxiality (a) and Lode parameter (b) in the nonlinear test (Uniaxial tension + mini-Nakazima). Continuous line: phase one; Dashed line: phase two.

Figure 5.27 (a) and (b) present the evolution of the stress triaxiality and Lode parameter in each phase. The values attained in each phase are identical to the ones found in the monotonic strain patch simulations (see **Figure 5.7** for the first phase and **Figure 5.22** for the second). The stress triaxiality changes after the onset of necking, which is connected with the strong thinning predicted. Considering the results from the monotonic strain paths, the weak influence of the constitutive models on the numerical solution was expected for uniaxial tensile stress and equibiaxial stress conditions.

5.2.2. Marciniak followed by Mini-Nakazima (equibiaxial)

5.2.2.1. Specimen with 5.5 inch (Marciniak)

In this test, the Marciniak tools were selected to deform the 5.5 inch specimen, followed by the mini-Nakazima tools. **Figure 5.28** shows the comparison between the predicted strain path for the three models, as well as the experimental results. In this case, a pre-strain of 3% was imposed. As for the previous case, the experimental data does not show the elastic recover between loading stages. However, for this bilinear path the impact seems smaller, due to the different trajectory predicted in the experimental and numerical results, during the first stage. In the second stage, the ratio between the major and minor strain in the experimental results is 1.024 and in the numerical is 1.095. Taking into account the results for the monotonic strain paths, the difference between experimental and numerical results shown in the **Figure 5.28** was expected. The differences seem more negligible due to the small pre-strain value.

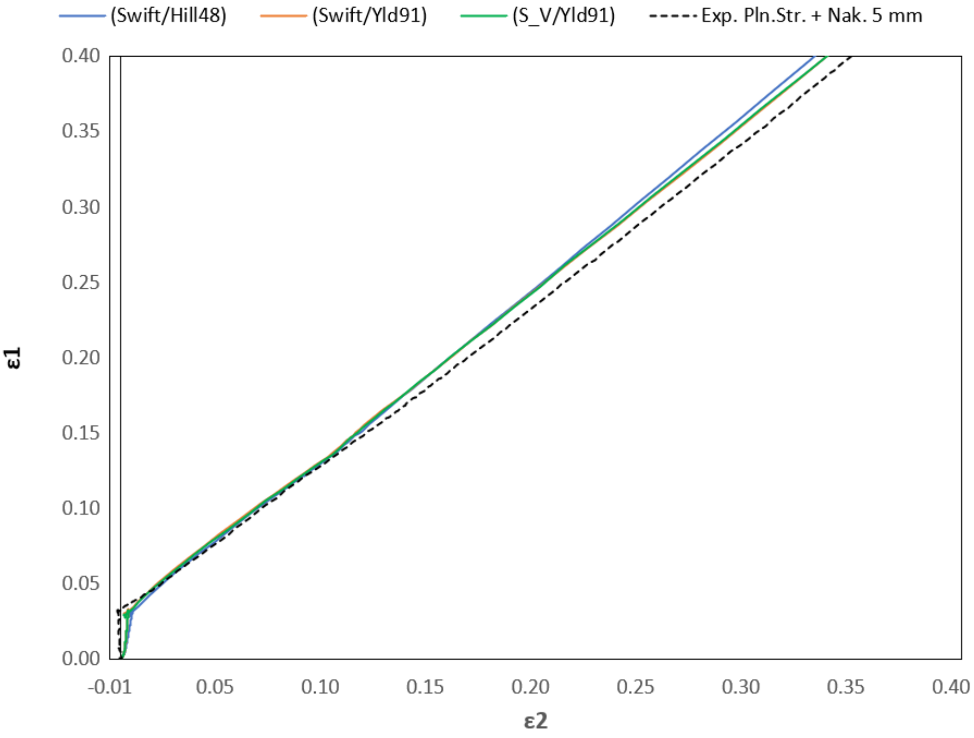

Figure 5.28. Comparison of the major strain-minor strain evolution between experimental and numerical results of the nonlinear test (5.5 inch Marciniak + mini-Nakazima).

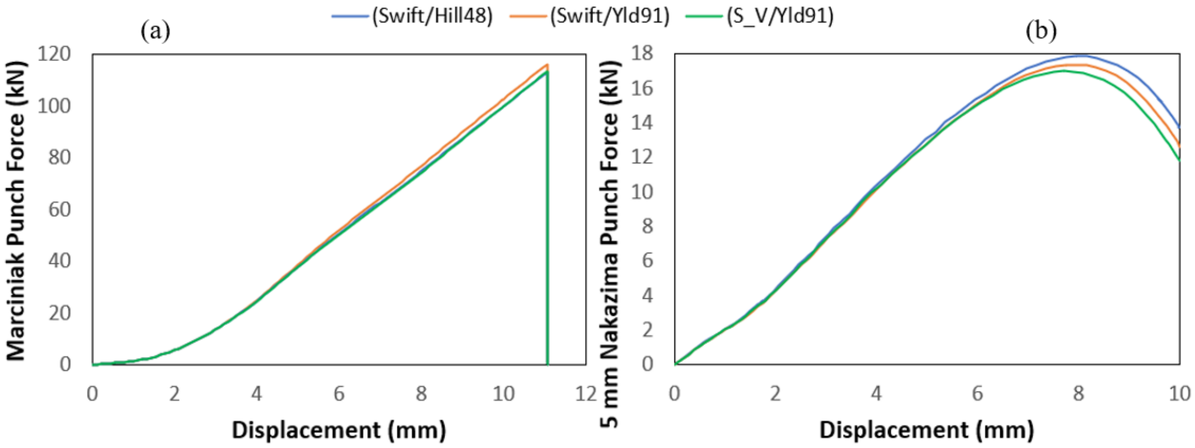

Figure 5.29. Evolution of the predicted force applied to the specimen in the nonlinear test (5.5 inch Marciniak + mini-Nakazima): (a) First phase; (b) Second phase.

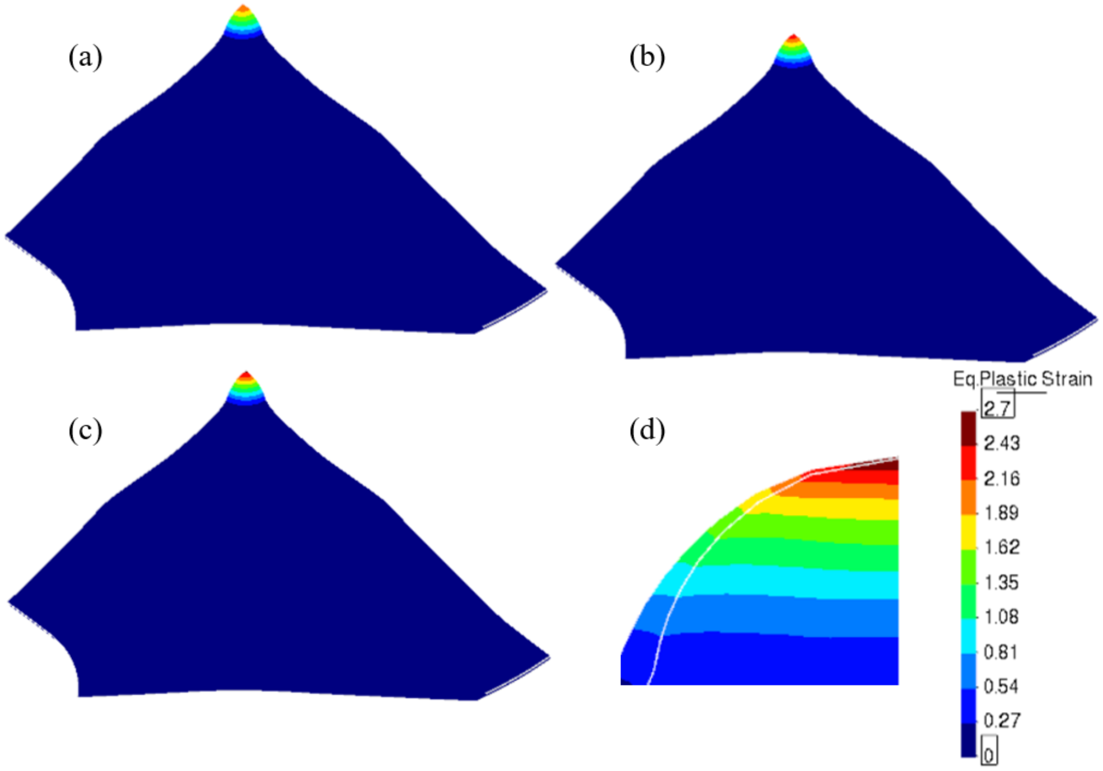

Figure 5.30. Equivalent plastic strain in the specimen of the nonlinear test (5.5 inch Marciniak + mini-Nakazima): (a) Swift/Hill48, (b) Swift/Yld91, (c) S_V/Yld91; (d) Strain distribution in the center of the specimen, as predicted with the S_V/Yld91 model.

Figure 5.29 presents the punch force evolution in each loading stage, highlighting the similarities with the ones reported for the monotonic strain paths, in **Figure 5.9** (a) and in **Figure 5.20** (b). In this case, the maximum punch force under equibiaxial stress conditions is attained for a punch displacement of approximately 8.1mm. This value is slightly smaller than the one reported for the previous bilinear strain path. Thus, the pre-strain for a path closer to plane strain seems to have a higher influence on the strains distributions than the uniaxial tensile one.

Figure 5.30 shows the distribution of the equivalent plastic strain in the specimen. For a punch displacement of 11.5 mm the maximum equivalent plastic strains is 2.30, 2.58 and 2.7 for the model Swift/Hill48, Swift/Yld91 and S_V/Yld91, respectively. The localization also occurs in the center of the specimen, as highlighted in **Figure 5.30** (d), which confirms that the application of pre-strains in different conditions did not change the ability of the model to reproduce the equibiaxial stress state in the center of the specimen. **Figure 5.31** (a) and (b) presents the evolution of the stress triaxiality and the Lode parameter, respectively, in each phase of loading. It is evident that, as in the monotonic strain path (see **Figure 5.11** (b)), it was not possible to perfectly reproduce the plane strain state in the first loading stage. As in the previous bilinear strain path case, the stress triaxiality changes after the onset of necking, which is connected with the strong thinning predicted (see **Figure 5.30** (d)).

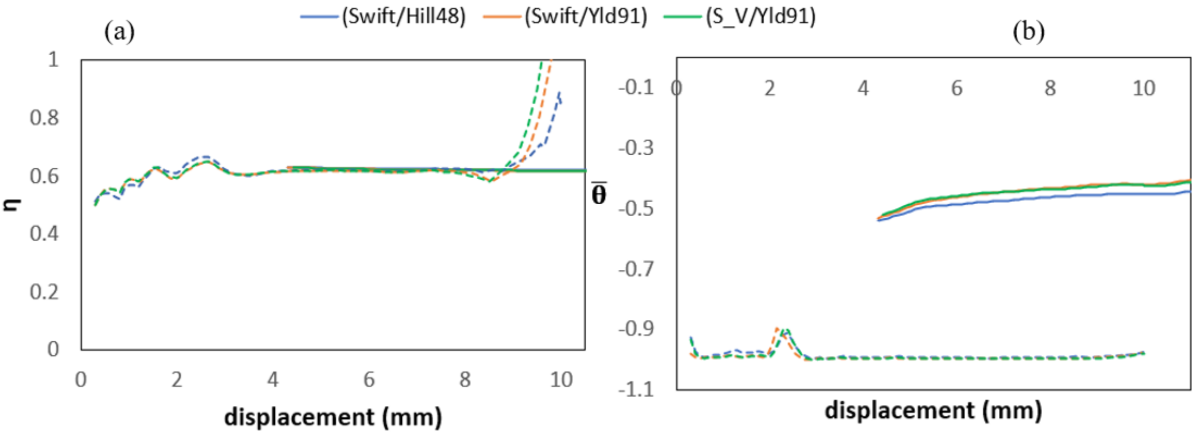

Figure 5.31. Evolution of triaxiality (a) and Lode parameter (b) in the nonlinear test (5.5 inch Marciniak + mini-Nakazima). Continuous line: phase one; Dashed line: phase two.

5.2.2.2. Specimen with 6.5-inch (Marciniak)

The last simulation considers the 6.5 inch specimen for the first stage, using the Marciniak tools. Thus, the first stage is biaxial and the second equibiaxial. **Figure 5.32** displays the major-minor strain evolution for the experimental and numerical results. This is the test with the most subtle change in strain trajectory, which makes the elastic recovery of the material almost imperceptible in the numerical models. In this case, a pre-strain of 12% was imposed. As for the monotonic strain path, the impact of the yield criteria selected is evident, in the first phase. The differences in the first phase are more evident than the previous one, because higher strain values are attained. In the second stage, the ratio between the major and minor strain in the experimental results is 1.004 and in the numerical is 0.965 and 0.996, for the Hill48 and the Yld91 models, respectively. Thus, the comparison with the results for the monotonic strain path indicate that this pre-strain seems to induce a slight change in the strain path under equibiaxial stress (see **Figure 5.20** (a)).

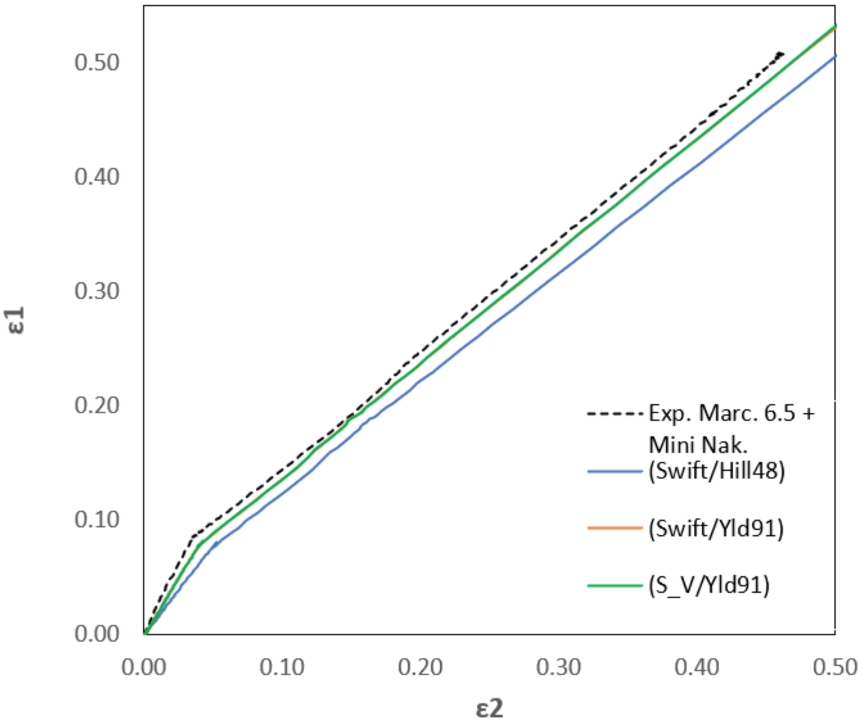

Figure 5.32. Comparison of the major strain-minor strain evolution between experimental and numerical results of the nonlinear test (6.5 inch Marciniak + mini-Nakazima).

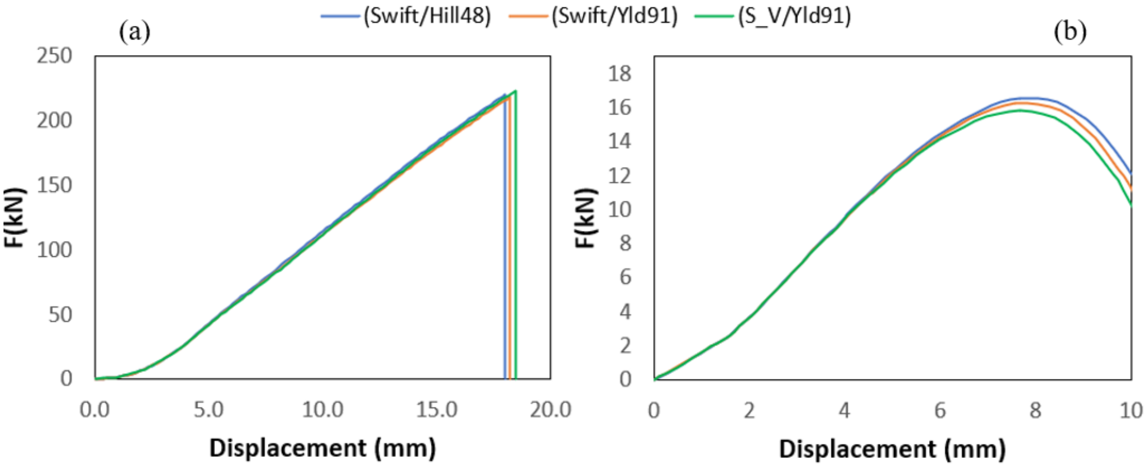

Figure 5.33. Evolution of the predicted force applied to the specimen in the nonlinear test (6.5 inch Marciniak + mini-Nakazima): (a) First phase; (b) Second phase.

Figure 5.33 shows the punch force evolution in each stage of the bilinear strain path. As in the previous nonlinear tests, the evolution of the punch force is very similar to those presented for the monotonic results (**Figure 5.12** (b) and **Figure 5.20** (b)). **Figure 5.33** (a) highlights that in this case different punch displacements had to be imposed to assure the same pre-strain. As for the other bilinear strain paths, the maximum punch force of the mini-Nakazima punch is attained for a punch displacement of approximately 7.6 mm. The trend between the three constitutive models is unaltered.

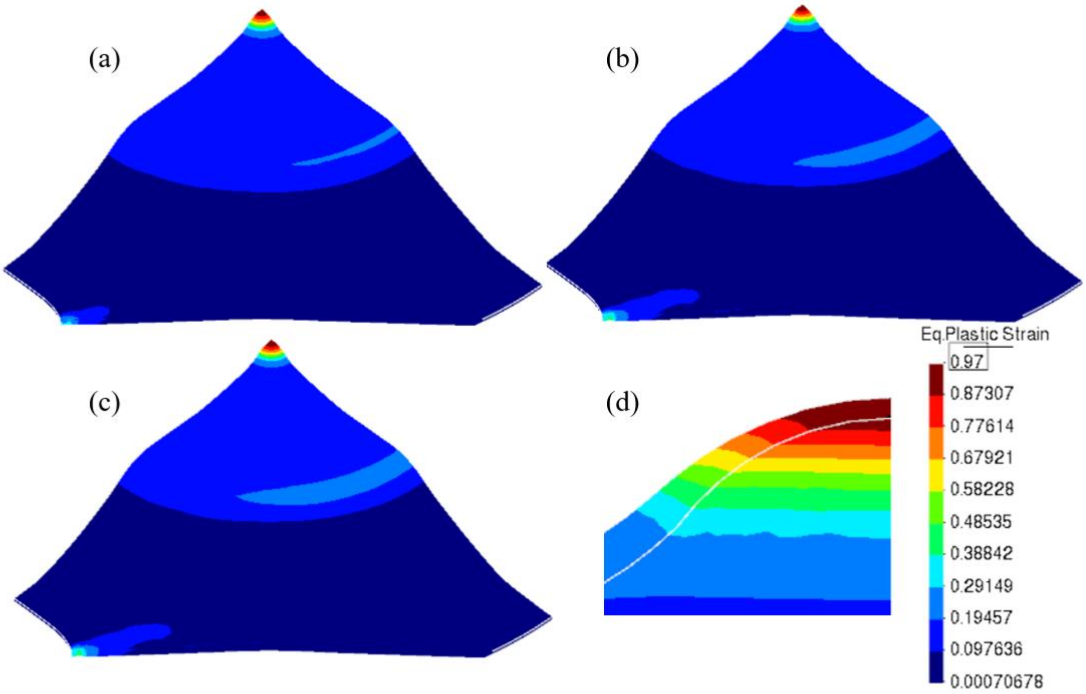

Figure 5.34. Equivalent plastic strain in the specimen of the nonlinear test (6.5 inch Marciniak + mini-Nakazima): (a) Swift/Hill48, (b) Swift/Yld91, (c) S_V/Yld91; (d) Strain distribution in the center of the specimen, as predicted with the S_V/Yld91 model.

Figure 5.34 shows the distribution of the equivalent plastic strain in the specimen at the end of the second phase. For 7 mm of displacement of the 5 mm radius punch, the maximum equivalent plastic strain predicted by the Swift/Hill48, Swift/Yld91 and S_V/Yld91 models is 0.95, 0.96 and 0.98, respectively. The strain localization occurs in the center of the specimen, as in all other simulations that used the mini-Nakazima tools, as highlighted in the **Figure 5.34** (d).

5.2.3. Comparisons of bilinear strain path results and discussion

All constitutive models enable a fairly accurate reproduction of the bilinear strain paths. Nevertheless, the models that use the Yld91 yield criterion lead to results closer to the experimental ones. The exception is in uniaxial tension and equibiaxial stress tests, for which the results of both yield criteria were very close. It is noteworthy that the plasticity model enables the prediction of the strain localization, but the fracture prediction would require the use of a damage model. In this context, many of the uncoupled fracture models are based on the equivalent strain at fracture, as discussed in chapter **2**.

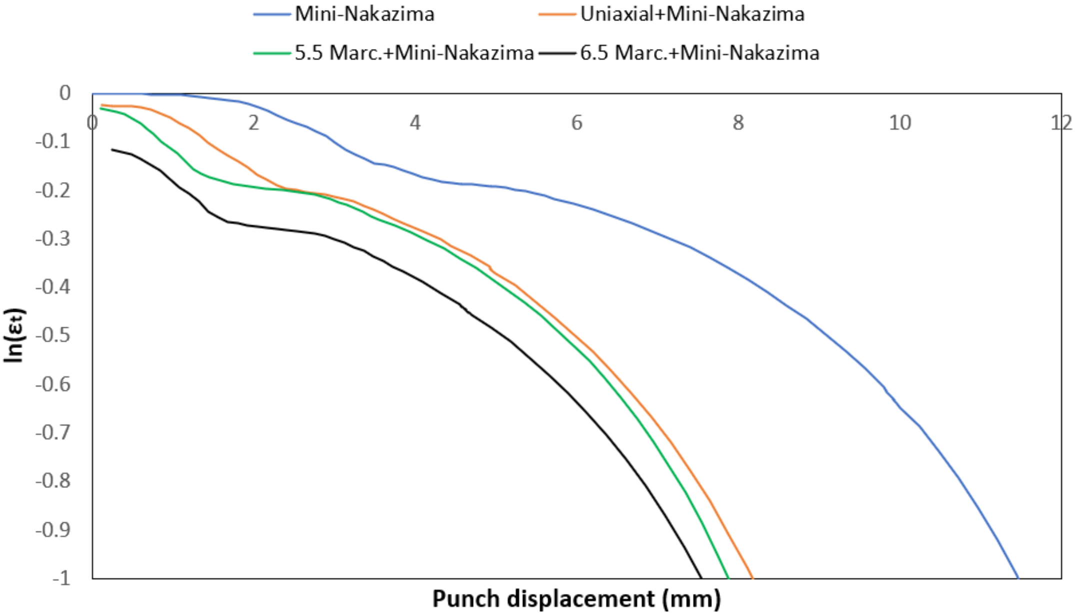

Figure 5.35. Evolution of the strain along the thickness direction, at the center of the specimen, in function of the punch displacement (Swift/Yld91 model).

Figure 5.35 shows the evolution of the strain in the thickness direction, at the center of the specimen, in function of the mini-Nakazima punch displacement. The results are shown only for the Swift/Yld91 model, since the other present a similar trend. The evolution obtained with the monotonic test is compared with the bilinear strain paths. The trend is similar in all tests, with an inflection point that can be related with the changes in the contact conditions between the blank and the punch. In fact, in the beginning of the test the contact changes from the center point to the periphery. Afterwards, with the increase of the thickness strain, the contact in the center is established again. The figure highlights that the through-thickness pre-strains induced by uniaxial tension and close to the plane strain conditions are quite similar. However, the conditions imposed in the first path are enough to change the evolution in the second one. The biaxial through-thickness pre-strain is quite higher, which justifies the smallest displacement for which the localization occurs. **Figure 5.35** shows that the drop of the punch force is being predicted for a thickness strain ln (ε_t) close to -1, which corresponds to a thickness of 0.33 mm.

6. CONCLUSION

The main scope of this work was to access the ability of constitutive models to predict nonlinear strain paths in sheet metal forming. The numerical strain paths solutions are compared to the experimental ones, provided by the benchmark committee, in order to assess the accuracy of each constitutive model. Furthermore, the analysis of the strain fields was performed to access the ability of the plasticity model to predict the strain localization. The tests were performed for conditions close to uniaxial tension, plane strain and different biaxial stress ratios. In the numerical models adopted, the drawbeads were replaced by a null displacement in the outer radius of the specimen. It was possible to conclude that the use of this simplification leads to substantial computational gains, in comparison to the physical drawbeads.

In all tests performed, it was possible to predict the strain localization and the consequent drop in the forming force. For the conditions close to uniaxial tension, necking occurs leading to the change of the strain path. However, for the plane strain and biaxial conditions the necking occurs in the punch shoulder area and not in the center of the specimen. Moreover, in the equibiaxial tests the strain localization occurs in a wide region, around the specimen center, never presenting a strong gradient.

The results from the monotonic strain paths tests highlight the importance of the yield criterion, which has a greater influence on the strain path predicted than the hardening law. This is more evident under conditions close to plane strain, which is the region where the yield criteria present higher differences in terms of the normal to the yield *loci*. In this context, it should be mentioned that no experimental data for plane strain was available to calibrate the yield criteria. Another conclusion that can be drawn from the monotonic tests is that the Barlat91 leads to strain paths closer to the experimental ones, when compared with the ones predicted by Hill48. Regarding the hardening law, the combined Swift and Voce always leads to a lower maximum punch force, which is attained also for a lower displacement. This can be related with the fact that it also predicts a lower value for the equivalent plastic strain that leads to the onset of necking, under the uniaxial stress state. The same effects are valid for the bilinear strain paths.

6.1. Remarks for future work

The simplification adopted to reproduce the intermediate blank in the Marciniak test should be evaluated, by performing the tests considering the two deformable bodies. Although, it is not expected to have a great influence on the results, small changes on the strain paths can occur as consequence of some sliding between the two blanks. Moreover, it was assumed that the differences between the physical drawbead and the boundary conditions adopted would be higher for the specimen with the smaller width. Nevertheless, it would be interesting to evaluate the differences between both models for other stress state conditions.

In addition to the bilinear strain paths analyzed in this work, it will be interesting to carry out simulations for other ones, which require resorting to other numerical tools to enable the trimming of small specimens for the pre-strained ones.

The results presented in this work highlight that if the goal is to predict ductile fracture the constitutive model must include a yield criterion that enables a proper description of the strain field but also a damage model. The results provided by the benchmark committee only allow to identify non-coupled fracture models, since there is no information regarding the punch force evolution. Some of these models can be calibrated based on the information extracted on this work regarding the evolution of the stress triaxiality and the Lode parameter.

BIBLIOGRAPHY

[1] F. Hensler, “Advantage: Excellence in Engineering Simulation, SPOTLIGHT ON MULTIPHYSICS,” *ANSYS Inc.*, vol. VIII. 2014.

[2] D. Banabic, *Sheet Metal Forming Processes. Metal Forming.* Springer, 2010.

[3] T. B. Stoughton and J.-W. Yoon, “2020 NUMISHEET BENCHMARK 2 – Fracture Model Prediction for Nonlinear Strain Paths,” *12th Int. Conf. Work. Numer. Simul. 3D Sheet Met. Form. Process.*, not published.

[4] “ASTM E8 / E8M-21,” *Standard Test Methods for Tension Testing of Metallic Materials*. ASTM International, West Conshohocken, PA, 2021.

[5] A. E. T. D. Banabic, H.-J. Bunge, K. Pohlandt, *Formability of Metallic Materials: Plastic Anisotropy, Formability Testing, Forming Limits*. Springer, 2000.

[6] W. F. Hosford, *MECHANICAL BEHAVIOR OF MATERIALS*, 2nd ed. Cambridge University Press, 2005.

[7] T. B. Stoughton and J.-W. Yoon, “Constitutive Model Calibration Data,” *12th Int. Conf. Work. Numer. Simul. 3D Sheet Met. Form. Process.*, not published.

[8] T. B. Stoughton and J.-W. Yoon, “Local DIC Strain Data,” *12th Int. Conf. Work. Numer. Simul. 3D Sheet Met. Form. Process.*, not published.

[9] T. B. Stoughton and J.-W. Yoon, “Fracture Characterization in Uniaxial Tension,” *12th Int. Conf. Work. Numer. Simul. 3D Sheet Met. Form. Process.*, not published.

[10] W. E. Luecke, “Numisheet 2020 tension / compression tests for steel alloys DP1180 and DP980,” *12th Int. Conf. Work. Numer. Simul. 3D Sheet Met. Form. Process.*, not published.

[11] E9-19, “ASTM E9-19,” *Standard Test Methods of Compression Testing of Metallic Materials at Room Temperature*. ASTM International, West Conshohocken, PA, 2019.

[12] A. D. Santos, P. Teixeira, A. Barata Da Rocha, and F. Barlat, “On the determination of flow stress using bulge test and mechanical measurement,” *AIP Conf. Proc.*, 2010.

[13] L. C. Reis, M. C. Oliveira, A. D. Santos, and J. V. Fernandes, “On the determination of the work hardening curve using the bulge test,” *Int. J. Mech. Sci.*, 2016.

[14] M. Gorji, B. Berisha, P. Hora, and F. Barlat, “Modeling of localization and fracture phenomena in strain and stress space for sheet metal forming,” *Int. J. Mater. Form.*, 2015.

[15] M. Dunand and D. Mohr, “Hybrid experimental-numerical analysis of basic ductile fracture experiments for sheet metals,” *Int. J. Solids Struct.*, 2010.

[16] C. C. Roth and D. Mohr, “Ductile fracture experiments with locally proportional loading histories,” *Int. J. Plast.*, 2016.

[17] N. Pathak, C. Butcher, and M. Worswick, “On simulation of edge stretchability of an 800MPa advanced high strength steel,” *J. Phys. Conf. Ser.*, 2016.

[18] N. Pathak, C. Butcher, and M. Worswick, “Assessment of the Critical Parameters

Influencing the Edge Stretchability of Advanced High-Strength Steel Sheet," *J. Mater. Eng. Perform.*, 2016.

[19] N. Pathak, C. Butcher, M. J. Worswick, E. Bellhouse, and J. Gao, "Damage evolution in complex-phase and dual-phase steels during edge stretching," *Materials (Basel).*, 2017.

[20] M. C. Kasaei, MM., Oliveira, "Influence of the Contact with Friction on the Deformation Behavior of Advanced High Strength Steels in the Nakajima Test," *J. Strain Anal. Eng. Des.*, 2021.

[21] T. Marciniak, T. Marciniak, and T. Cad, "Formability Characterization using Marciniak Tests," *12th Int. Conf. Work. Numer. Simul. 3D Sheet Met. Form. Process.*, not published.

[22] J. Noder and C. Butcher, "A comparative investigation into the influence of the constitutive model on the prediction of in-plane formability for Nakazima and Marciniak tests," *Int. J. Mech. Sci.*, 2019.

[23] Z. Marciniak and K. Kuczyński, "Limit strains in the processes of stretch-forming sheet metal," *Int. J. Mech. Sci.*, 1967.

[24] R. Zhang, Z. Shao, and J. Lin, "A review on modelling techniques for formability prediction of sheet metal forming," *Int. J. Light. Mater. Manuf.*, 2018.

[25] K.-H. Chang, *e-Design: Computer-Aided Engineering Design*. Elsevier Inc., 2015.

[26] Z. Deng and R. Hennig, "Influence of material modeling on simulation accuracy of aluminum stampings," *J. Phys. Conf. Ser.*, 2017.

[27] T. B. Gonoring, M. T. D. Orlando, J. L. Ferreira, M. V. de Souza, and L. P. Moreira, "Prediction of the Uniaxial Tensile Plastic Behavior of an interstitial free steel using different work-hardening equations," *ABM Week 2019*, 2019.

[28] "About Maplesoft." https://www.maplesoft.com/company/about/ (accessed Jul. 09, 2021).

[29] F. Pütz, F. Shen, M. Könemann, and S. Münstermann, "The differences of damage initiation and accumulation of DP steels: a numerical and experimental analysis," *Int. J. Fract.*, 2020.

[30] A. H. Ben Ouirane, N. Boudeau, R. Velasco, and G. Michel, "Error evaluation on experimental stressstrain curve obtained from tube bulging test," *Thin-Walled Struct.*, 2011.

[31] F. Barlat *et al.*, "Yielding description for solution strengthened aluminum alloys," *Int. J. Plast.*, 1997.

[32] L. F. Menezes and C. Teodosiu, "Three-dimensional numerical simulation of the deep-drawing process using solid finite elements," *J. Mater. Process. Technol.*, 2000.

[33] M. C. Oliveira, J. L. Alves, and L. F. Menezes, "Algorithms and strategies for treatment of large deformation frictional contact in the numerical simulation of deep drawing process," *Arch. Comput. Methods Eng.*, 2008.

[34] "GID / ABOUT US." https://www.gidhome.com/about-us/ (accessed Jul. 09, 2021).

[35] T. J. R. Hughes and J. Winget, "Finite rotation effects in numerical integration of rate constitutive equations arising in large-deformation analysis," *Int. J. Numer. Methods Eng.*, 1980.

[36] D. M. Neto, M. C. Oliveira, J. L. Alves, and L. F. Menezes, “Comparing faceted and smoothed tool surface descriptions in sheet metal forming simulation,” *Int. J. Mater. Form.*, 2015.

[37] D. M. Neto, “Numerical simulation of frictional contact problems using Nagata patches in surface smoothing,” Coimbra University, 2014.

[38] M. C. Oliveira, D. M. Neto, J. L. Alves, and L. F. Menezes, “Study on the influence of the yield surface shape in the hole expansion test,” *IOP Conf. Ser. Mater. Sci. Eng.*, 2020.

[39] J. L. Alves, S. Bouvier, M. C. Oliveira, and L. F. Menezes, “Drawbeads : to Be or Not to Be,” *NUMISHEET’2005, 6th Int. Conf. Work. Numer. Simul. 3D Sheet Form. Process. - Cut. Edge Technol.*, 2005.

[40] T. B. Stoughton and J.-W. Yoon, “Fracture Characterization in Biaxial Stretching,” *12th Int. Conf. Work. Numer. Simul. 3D Sheet Met. Form. Process.*, not published.

[41] B. Ii, I. Notes, and M. T. S. C. Model, “Pre-Straining,” *12th Int. Conf. Work. Numer. Simul. 3D Sheet Met. Form. Process.*, not published.

[42] C. Butcher, F. Khameneh, A. Abedini, D. Connolly, and S. Kurukuri, “On the experimental characterization of sheet metal formability and the consistent calibration of the MK model for biaxial stretching in plane stress,” *J. Mater. Process. Technol.*, 2021.

[43] J. Ha, M. Baral, and Y. P. Korkolis, “Plastic anisotropy and ductile fracture of bake-hardened AA6013 aluminum sheet,” *Int. J. Solids Struct.*, 2018.

[44] L. C. Reis, P. A. Prates, M. C. Oliveira, A. D. Santos, and J. V. Fernandes, “Anisotropy and plastic flow in the circular bulge test,” *Int. J. Mech. Sci.*, 2017.

[45] Y. Lou, S. Zhang, and J. W. Yoon, “Strength modeling of sheet metals from shear to plane strain tension,” *Int. J. Plast.*, 2020.

[46] Y. Bai, “Effect of Loading History on Necking and Fracture,” Massachusetts Institute of Technology, 2008.

APPENDIX A: TRIAXIALITY AND LODE PARAMETER

The Cauchy stress tensor $\boldsymbol{\sigma}$ presents three invariants, which can be defined in function of its components as follows:

$$I_1 = \mathrm{Tra}(\sigma_{ij}) = \sigma_{11} + \sigma_{22} + \sigma_{33}, \tag{17}$$

$$I_2 = \sigma_{11}\sigma_{22} + \sigma_{22}\sigma_{33} + \sigma_{11}\sigma_{33} - {\sigma_{12}}^2 - {\sigma_{23}}^2 - {\sigma_{13}}^2, \tag{18}$$

$$I_3 = \sigma_{11}\sigma_{22}\sigma_{33} + 2\sigma_{12}\sigma_{23}\sigma_{13} + \sigma_{11}\sigma_{33} - \sigma_{11}{\sigma_{23}}^2 - \sigma_{22}{\sigma_{13}}^2 - \sigma_{33}{\sigma_{12}}^2, \tag{19}$$

where Tra represents the trace of a second order tensor. The Cauchy stress tensor $\boldsymbol{\sigma}$ can also be decomposed into two parts, the hydrostatic and the deviatoric one $\mathbf{s}$, as follows:

$$\sigma_{ij} = \sigma_m \delta_{ij} + s_{ij}, \tag{20}$$

$$\sigma_m = \frac{1}{3} I_1, \tag{21}$$

where σ_m is the mean stress and δ_{ij} is the Kronecker symbol, i.e. $\delta_{ij} = 0$, if $i \neq j$ and $\delta_{ij} = 1$ if $i = j$ [45]. The hydrostatic component is responsible for volumetric (elastic) changes, while the deviatoric one is related with the plastic deformation. Also for the deviatoric stress tensor $\mathbf{s}$ it is possible to define its invariants, in function of its components, as follows [45]:

$$J_1 = s_{kk} = 0, \tag{22}$$

$$J_2 = \frac{1}{3} {I_1}^2 - I_2, \tag{23}$$

$$J_3 = \det(\mathbf{s}) = \sigma_{11}\sigma_{22}\sigma_{33} + 2\sigma_{12}\sigma_{23}\sigma_{13} - {s_{12}}^2 s_{33} + {s_{23}}^2 s_{11} + {s_{13}}^2 s_{22}. \tag{24}$$

Notice that, according with the definition given in equation (22), $J_1 = 0$, which is the main characteristic of any deviatoric quantity. Thus, any stress state that leads to plastic deformation can be characterized in function of its stress invariants. This approach is commonly adopted in literature, for defining ductile fracture criteria.

The principle is that any stress state can be defined in function of only two parameters: the stress triaxiality and the Lode parameter. The stress triaxiality η is defined as [45][46]:

$$\eta = \frac{\sigma_m}{\bar{\sigma}}, \tag{25}$$

where $\bar{\sigma} = \sqrt{3J_2}$, is the equivalent stress, defined according to the von Mises yield criterion. The normalized third stress invariant ξ is defined as:

$$\xi = \frac{\left(3\sqrt{3}\,J_3\right)}{\left(2J_2^{\frac{3}{2}}\right)} = \cos(3\theta_L), \tag{26}$$

such that ξ varies in the range of [-1, 1]. In equation (26), the Lode angle θ_L is also introduced, with a range of $[0, \pi/3]$. Based on this definition, it is also possible to determine the normalized Lode angle, as follows:

$$\bar{\theta} = 1 - \frac{6\theta_L}{\pi} = 1 - \frac{2}{\pi}\cos^{-1}(\xi), \tag{27}$$

with a range of [-1, 1] [45][46], which is also called the Lode parameter.

Whatever the variable selected along with the stress triaxiality, it is possible to associate specific values to corresponding stress states, as highlighted in **Figure A. 1** and **Figure A. 2**, considering the normalized third stress invariant and the normalized Lode angle, respectively. The values associated with uniaxial tension, equibiaxial tension and plane strain tension conditions are also displayed in the **Table A.1**.

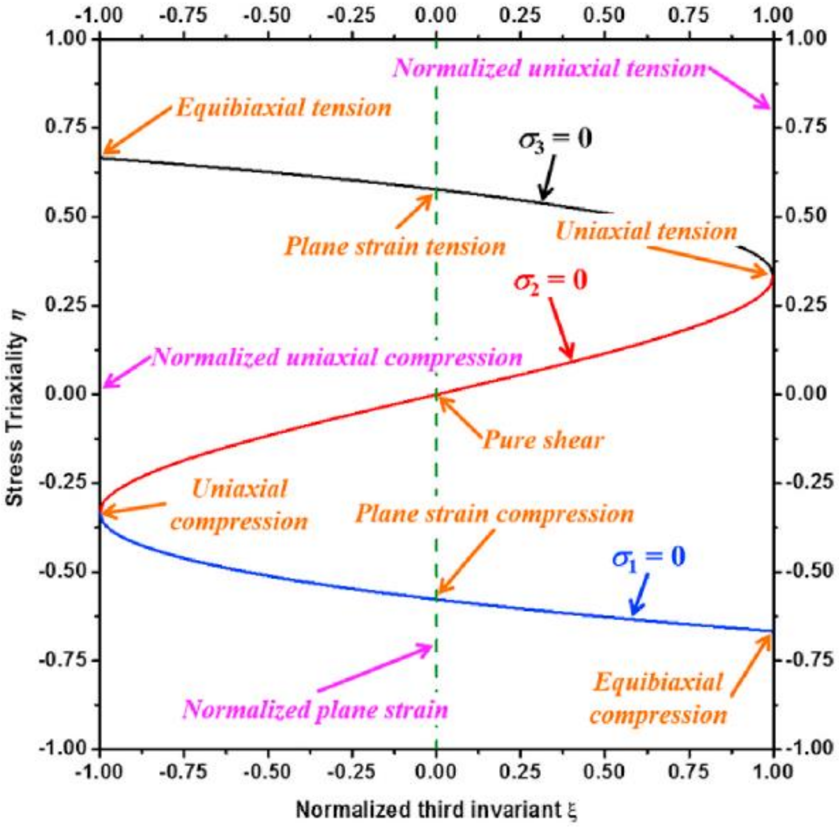

Figure A. 1. Usual values for stress states in the space of (η, ξ) [45].

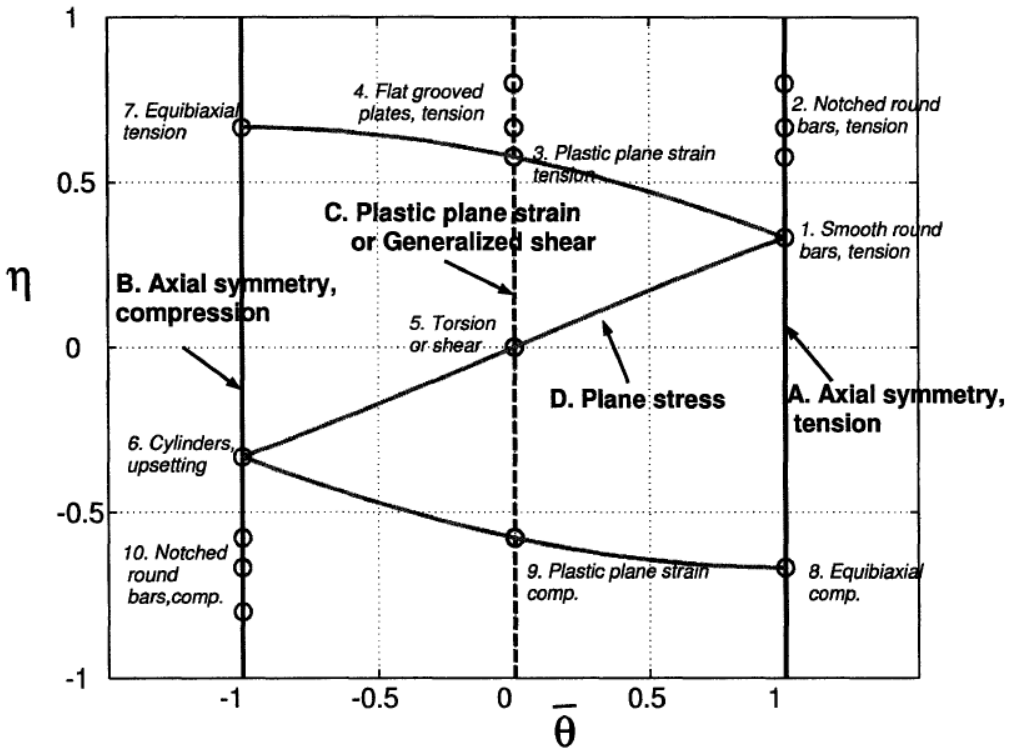

Figure A. 2. Usual values for stress states in the space of ($\boldsymbol{\eta}$, $\bar{\boldsymbol{\theta}}$) [46].

Table A.1. Usual values for $\boldsymbol{\eta}$, ξ and $\bar{\boldsymbol{\theta}}$ for each stress state condition [45][46].

	η	ξ	$\bar{\theta}$
Uniaxial tension	1/3	1	1
Equibiaxial tension	2/3	-1	-1
Plane strain tension	$\sqrt{3}/3$	0	0